Diffusion of laser polarized gases in MRI

Dissertation zur Erlangung des Grades

Doctor rerum naturalium

am Fachbereich Physik
der Johannes Gutenberg-Universität Mainz
vorgelegt von

Luis Agulles Pedrós
geboren in Dénia/Spanien

Mainz 2007

Tag der mündlichen Prüfung: 23. November 2007

Per a de qui tant vaig apendre
llevat de plorar

Contents

Abbreviations

ADC	Apparent Diffusion Coefficient
BG	Buffer Gas
D	Diffusion coefficient
$D_{i,j}$	Binary diffusion coefficient
$\left[D_{i,j}\right]_k$	k^{th} approximation of the binary diffusion coefficient
D_i	self diffusion coefficient of a component in a gas mixture
Δr	one dimensional mean free path
DW	Dwell Time
γ	magnetogyric ratio or gyromagnetic ratio
FID	Free Induction Decay
FLASH	Fast Low Angle SHot
FOV	Field Of View
FT	Fuorier Transformation
HP	Hyperpolarized
LP	Laser Polarized
l_s	cavity size
l_G	spin dephase characteristic length
MRI	Magnetic Resonance Imaging
NMR	Nuclear Magnetic Resonance
P	Polarization
p	pressure

PSF	Point spread function
r.f.	Radio Frequency
SNR	Signal to Noise Ratio
SW	Spectral Width
T_1	characteristic spin lattice relaxation time
T_2	characteristic spin spin relaxation time
w	number of collisions made by one particle divided by unit time
x	concentration
Xe	is referred to Xenon with all its isotopes
^{129}Xe	is referred to the isotope 129-Xenon mixed with the other isotopes of Xe

Chapter 1

Introduction

Qualunque cosa farai, amala come amavi
la cabina del Paradiso quand'eri picciriddu.
Nuovo cinema Paradiso (Giuseppe Tornatore)

In the 1930's Rabi and co-workers, based on the papers of Stern and Gerlach from ten years before, studied the interaction of the spin of a proton with a magnetic field. These quantum mechanical concepts were extended in 1946 by Bloch and Purcell to the measurement of the precession of nuclear spins in magnetic fields. They were awarded the Nobel Prize in Physics in 1952 for this work. These first steps of the Nuclear Magnetic Resonance (NMR) were extended in 1973 by Lauterbur and Mansfield by the development of magnetic resonance imaging (MRI), which allows acquiring 3D images and tomography. The idea was simple, since spins precess with a frequency (Larmor frequency) that depends on the magnetic field, the magnetic field has to be made spatially dependent to result in a frequency representation of the sample's geometry. They were awarded the Nobel Prize in Physiology or Medicine in 2003 for these works [Mans73] [Laut73].

Highly resolved images can only be obtained from parts of the body, which are rich in a sensitive NMR-isotope (e.g. protons) in highly mobile environments (e.g. liquids). Therefore, rigid tissues (e.g. bones) and hollow structures (e.g. lungs) do not contribute to the MR-image. While bones can be nicely resolved by X-ray techniques, the diagnostic imaging techniques for pulmonary diseases were very limited[1] until MRI with hyperpolarized gases was introduced by Albert *et al.* [Albe94].

[1] Essentially only scinitilography of gaseous radio isotopes (^{99}Tc, ^{127}Xe, ^{133}Xe, ^{181}Kr) can be used. Because the radioactive dosage is limited the concentration of such isotopes has to be kept relatively low, which results in poorly resolved images.

"Hyperpolarization" means that the polarization is larger than that given by thermal or Boltzmann polarization. The use of optical pumping with polarized laser increases the NMR-signal up to five orders of magnitude. This idea is based on the research of Alfred Kastler [Tayl00], who facilitated the study of atomic structures by means of the radiation that atoms emit under excitation by light and radio waves. He was awarded the Nobel Prize in Physic in 1966 for these works. Since then the technique of optical pumping (i.e. generating alignment of spins by transferring angular momentum to the spins from polarized light) has been studied extensively and developed by several groups [Bouc60][Sche65][Cole63][Gamb65][Heil99]. Recently, the field has expanded rapidly with the advent of inexpensive and high-power diode laser arrays. Liters of ^{3}He or ^{129}Xe with absolute nuclear polarizations of unity order [Wolf04] [Ruse06] can now be routinely produced in a matter of hours.

The development of hyperpolarized gases artificially increases the signal, and high quality MRI of gases can be achieved this way [Good02][Beck98]. The gain in sensitivity and acquisition time is in principle of a great advantage compared to water [Char92] [Glad94]. Thus, in the last decade MRI of hyperpolarized gases was introduced for imaging of voids in porous systems, as foams, granular systems and lungs [Blüm94] [Appe98]. A particular interesting question in spatially resolved experiments with gases is the achievable resolution and contrast. However, the effects on the MRI quality which arise from the use of gases rather than liquids have not been discussed in detail yet.

Compared with liquids, gases have a much higher diffusivity which strongly influences the NMR signal strength, hence the resolution and appearance of the images. The influence of such diffusive processes scales with the diffusion coefficient of the gas, the strength of the magnetic field gradients and the timings used in the experiment. Diffusion may not only limit the MRI resolution, but also distort the line shape of MR images for samples, which contain boundaries or diffusion barriers within the sampled space [Saam96] [Swie95]. Therefore, the objective of this work was the determination and quantification of the influence of gas diffusion on the appearance of MR images. Additionally, different strategies were tested to optimize resolution and contrast for different applications.

In Chapter 2 an introduction to the basics of NMR and MRI is given, as well as to the principles of hyperpolarization and diffusion. Chapter 3 summarizes the used experimental devices and setups.

Chapter 4 includes the basics of the theory of particle diffusion and the possible anomalies of diffusion measurements by NMR which can arise from spin current dependence on magnetization. This dependence is studied for ^{129}Xe and ^{3}He, for

different collisions regimes through variation of pressure.

In lung imaging the hyperpolarized gas is an admixture of gases; in particular oxygen and nitrogen. Therefore, Chapter 5 studies the diffusion coefficient of one component in binary gas admixtures, comparing NMR measurement and simulations of ^{129}Xe and ^{3}He in admixture with other buffer gases. For that purpose a novel method to mix gases is presented, which can be synchronized with the NMR-sequence. The synchronization permits the reproducibility of concentrations in the mixture with high precision.

The change and control of the diffusion coefficient of these relevant NMR isotopes, ^{129}Xe and ^{3}He, allow a detailed study of the MR images upon diffusion –and therefore upon concentration– which is presented in chapter 6. By controlling and adjusting the diffusion coefficient to the experimental conditions, these effects can be used to improve image resolution or to enhance the signal of cavities. These studies were restricted to ^{3}He since it is commonly used in MRI.

This results can be of major importance for instance, for the increase in resolution and accuracy of apparent diffusion coefficient (ADC) maps of lungs that present a severe emphysema, were the signal in the affected region would otherwise be severely attenuated by rapid diffusion. Finally, it should be emphasized that even though the work was centered on MRI, the results can be of importance for any experiment that involves field gradients, such as probing restricted diffusion and flow in porous systems, which yield information on the structure of materials.

Chapter 2

Introductory Theory

In this chapter the theoretical background will be discussed: NMR and MRI [Levi01] [Call91] [Haac99] [Erns87] [Tala91], diffusion coefficient measurements [Call91] [Pric97] and laser polarized gases [Bouc60] [Cole63] [Appe04] [Appe98]. For a deeper understanding, however, a more specific theoretical description will be carried out at the beginning of each experimental chapter concerning to the topic that will be presented.

2.1 Introduction

From the 5^{th} century BC, Democritus and Leucippus already introduced the belief that all matter is made up of various imperishable, indivisible elements which they called “atoma” or “indivisible units”. Of importance to the philosophical concept of atomism is the historical accident that, the particles that chemists and physicists of the early 19^{th} century AC thought were indivisible, were found in the 20^{th} century to be composed of even smaller entities: electrons, neutrons, protons and so on. This work will focus on the the nuclei of the atoms, which are composed by neutrons and protons (also known collectively as nucleons).

Nuclear Magnetic Resonance (NMR) is a phenomenon that occurs when the nuclei of certain atoms are brought into a static magnetic field. Protons (electrically charged) and neutrons posses an intrinsic magnetism, which is not due to a circulating current.

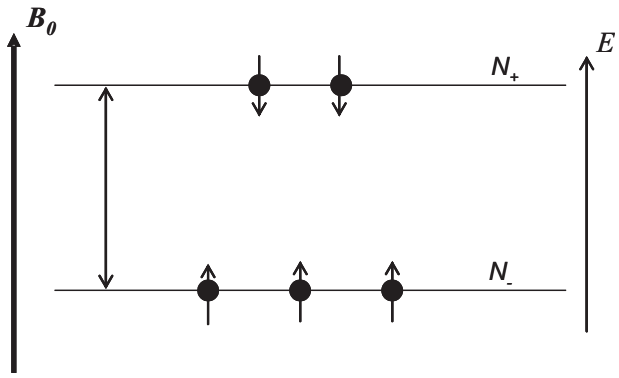

Figure 2.1: Distribution of spin population in energy levels due to the action of a magnetic field. The shown orientation of the spin depends on the magnetic moment, which is $\mu < 0$ for ^{3}He and ^{129}Xe

2.1.1 Quantum Mechanical description

The intrinsic angular momentum or spin of a nucleon is characterized by a spin quantum number, I. Since the nucleus has both, spin and charge distribution, it will have an associated nuclear magnetic moment, $\boldsymbol{\mu}$, which is collinear and proportional to the spin angular momentum $\mathbf{I}$,

$$\boldsymbol{\mu} = \gamma\hbar\mathbf{I} \tag{2.1}$$

with a proportionality constant, γ, the magnetogyric ratio (or gyromagnetic ratio) and $\hbar = h/2\pi$ the Dirac's constant, which is proportional to the Planck's constant, h. The response of the spin vector is to move around the magnetic field. The magnetic moment of the spin moves on a cone, keeping a constant angle between the spin magnetic moment and the field.

The nuclei have a potential energy when brought into a magnetic field of flux density $\mathbf{B_0}$. From quantum mechanics it is known that angular momentum and the associated energies are quantized and can only assume discrete values. Hence in the presence of such an external magnetic field $\mathbf{B_0}$, the degeneracy of the eigenstates of the nuclear spins vanishes, resulting in m energy levels with

$$E_m = \mathbf{B_0}\boldsymbol{\mu} = \gamma\hbar\mathbf{I}\mathbf{B_0} = -m\gamma\hbar B_0 \tag{2.2}$$

which are proportional to the magnetic quantum number $m = -I, -I+1, \ldots, I-1, I$, where $\mathbf{B_0} = (0, 0, B_0)$ is chosen to define the z-direction.

As a result a nucleus with quantum number I may assume $2I+1$ discrete energy levels. An observation known as Zeeman splitting. Since this work exclusively deals

with nuclei (^{3}He and ^{129}Xe) having $I = 1/2$ only two such energy levels or directions of the spins exists ("up" and "down") as shown in Fig.2.1. In this case the energetic distance between the two levels of Eq.2.2 are given by

$$\Delta E = E_{1/2} - E_{-1/2} = \gamma \hbar B_0 \tag{2.3}$$

which corresponds to a frequency

$$\omega_0 = \frac{\Delta E}{\hbar} = \gamma B_0 \tag{2.4}$$

which is called the *Larmor* frequency.

From the quantum mechanical point of view, the energy is related to the Hamiltonian of the system. For the actual case the sum of the total energy system is given by

$$\hat{\mathcal{H}} = \hat{\mathcal{H}}_Z + \hat{\mathcal{H}}_{rf} + \hat{\mathcal{H}}_{DD} + \hat{\mathcal{H}}_{CS} + \hat{\mathcal{H}}_J + \hat{\mathcal{H}}_Q. \tag{2.5}$$

where $\hat{\mathcal{H}}_Z$ refers to the Zeeman splitting due to the magnetic field and $\hat{\mathcal{H}}_{rf}$ refers to the external radio frequency field used to manipulate the spin ensemble evolution, which are both externally applied.

The Hamiltonian $\hat{\mathcal{H}}_{DD}$ refers to the direct dipole–dipole coupling interaction due to magnetic interactions of nuclear spins with each other, $\hat{\mathcal{H}}_{CS}$ refers to the the chemical shift due to the indirect magnetic interaction of the nuclear spins and the external magnetic field mediated by the electrons, $\hat{\mathcal{H}}_J$ refers to the indirect dipole–dipole coupling (J-coupling) interaction due to the magnetic interactions of nuclear spins with each other mediated by the electrons, and $\hat{\mathcal{H}}_Q$ refers to the quadrupolar coupling due to the electric charge distribution in the nucleus with the electric field gradients resulting from surrounding charges. All of these are internal spin interactions and therefore intrinsic to the material being studied.

External spin interactions

When spins are placed into an external constant magnetic field $\mathbf{B}_0$, they align within the field. The energy, and therefore the Zeeman Hamiltonian, is equal to this described in Eq.2.2:

$$\hat{\mathcal{H}}_Z = E_m = \mathbf{B_0}\boldsymbol{\mu} = \gamma\hbar\mathbf{I}\mathbf{B_0} = -m\gamma\hbar B_0 \ . \tag{2.6}$$

If a short and strong time-dependent magnetic field, $\mathbf{B}_{rf}$, is applied in the x-direction by means of a r.f. coil with a phase ϕ and frequency oscillation ω_1, the field

will be given by

$$\mathbf{B}_{rf} = B_{rf}\cos(\omega_1 t + \phi)\mathbf{e}_x \tag{2.7}$$

where B_{rf} is the maximum oscillation amplitude. It is convenient to visualize this oscillating field as two counter rotating vectors representing the resonant and non-resonant components. The resonant component rotates with the Larmor precession and the non-resonant component in the opposite direction:

$$\mathbf{B}_{rf}^{res} = \frac{B_{rf}}{2}\left[\cos(\omega_1 t + \phi)\mathbf{e}_x + \sin(\omega_1 t + \phi)\mathbf{e}_y\right] \tag{2.8}$$

$$\mathbf{B}_{rf}^{non-res} = \frac{B_{rf}}{2}\left[\cos(\omega_1 t + \phi)\mathbf{e}_x - \sin(\omega_1 t + \phi)\mathbf{e}_y\right] \tag{2.9}$$

Although it wastes half of the r.f. field, the non-resonant component has almost no influence on the spins and may be neglected [Levi01]. Then, the corresponding Hamiltonian for the effect of an r.f. pulse is:

$$\hat{\mathcal{H}}_{rf} \approx -\gamma\hbar B_1\left[\cos(\omega_1 t + \phi)\hat{I}_x + \sin(\omega_1 t + \phi)\hat{I}_y\right] \tag{2.10}$$

where $B_1 = \frac{1}{2}B_{rf}$. The quantity $|\gamma B_1|$ is proportional to the peak r.f. field in the coil. This is called the nutation frequency, ω_{nut}, and is a measure of how strongly the r.f. field influences the resonant spins.

Internal spin interactions

In usual NMR experiments internal spin interactions are the most important source of information [Levi01] [Call91][Tala91]. However, since this work only deals with ^{3}He and ^{129}Xe for imaging purposes, the internal spin interactions of Eq.2.5 can be ignored for the following reasons:

• For spins $I = 1/2$ there are no electric energy terms which depend on the orientation or internal structure of the nucleus, i.e. all spins behave like a single point charge at the nuclear center, so there is no quadrupole interaction.

• The J-coupling provides a direct spectral manifestation of the chemical bond. As ^{3}He and ^{129}Xe are atoms that do not form molecules under the experimental conditions carried out in this experiments of this work, J-coupling do not have to be considered. The same argument also applies to the chemical shift interaction.

• Direct dipole–dipole interaction had been recently observed in ^{3}He gas at ambient temperature but at high pressures to slow down the diffusion [Zaen07], experimental conditions that won't be used in this work.

Finally, the evolution of the spin system is described by the time-dependent Schrödiger equation

$$\frac{\mathrm{d}}{\mathrm{d}t}|\Psi(t)\rangle = \frac{-i}{\hbar}\hat{\mathcal{H}}\,|\Psi(t)\rangle\,. \tag{2.11}$$

Quantum mechanics has therefore given an explanation for the behaviour of a nuclear spin; a single nucleus in isolation. However usually it is dealt with large ensembles in which different nuclei may occupy different states $|\Psi(t)\rangle$. The description must therefore account for the ensemble averages. This is done by representing the average by a sum over all subensembles, each with classical probability N_i. In each subensemble all nuclei are in identical states $|\Psi(t)\rangle$. For example, the averaged expectation value along the z-axis then becomes

$$\overline{\langle\Psi(t)|\hat{I}_z|\Psi(t)\rangle} = \sum_i N_i \langle\varphi_i(t)|\hat{I}_z|\varphi_i(t)\rangle \tag{2.12}$$

where the bar over a quantity is taken to represent the averaging of the subensembles and $|\varphi_i(t)\rangle$ represent the eigenstates. For the case of spin $I = 1/2$, the expectation value is given by

$$\overline{\langle\Psi(t)|\hat{I}_z|\Psi(t)\rangle} = \frac{1}{2}\left(\overline{|N_+|^2} - \overline{|N_-|^2}\right), \tag{2.13}$$

where N_+ and N_- are the number of spins in the $m_I = +1/2$ and the $m_I = -1/2$ states respectively.

2.1.2 Semi-classical description

From the semi-classical point of view, N corresponds to the population of the energy levels of Fig.2.1. The population of the two energy levels is very similar, because the energy difference is small compared to the thermal energy of the system at ambient temperature. The ratio of the populations in thermal equilibrium at temperature is then given by a Boltzmann distribution

$$\frac{N_+}{N_-} = \exp\left(-\frac{\Delta E}{k_B T}\right) = \exp\left(-\frac{\hbar\omega_0}{k_B T}\right) = \exp\left(-\frac{\hbar\gamma B_0}{k_B T}\right) \tag{2.14}$$

where k_B is Boltzmann's constant and T is the temperature in kelvin. A related quantity is the polarization, P_B, which describes the excess population of the two energy levels

$$P_B = \frac{N_+ - N_-}{N_+ + N_-} = \tanh\left(\frac{\hbar\gamma B_0}{2k_B T}\right). \tag{2.15}$$

This expression is simplified by the fact that the thermal energy is much bigger than the magnetic dipole energy, thus $T >> \hbar\omega_0/k_B$. This is the so-called "high temperature" approximation, in which Eq.2.15 becomes

$$P_B \approx \left(\frac{\hbar\gamma B_0}{2k_B T}\right) \tag{2.16}$$

For example, ^{3}He or ^{1}H nuclei at room temperature and a magnet field of $4.7T$ have a polarization of 19.6 and 26.1 per million respectively.

Finally the observable NMR-signal has an intensity which is proportional to the sum of all magnetic moments. This macroscopic magnetization, M_0, is then given by

$$M_0 = \sum_j^{N_S} \mu_j = \frac{N_S \hbar\gamma P_B}{2} \tag{2.17}$$

where $N_S = N_+ + N_-$ is the total number of spins.

In order to observe such a signal, the thermal equilibrium must be perturbed by applying an additional magnetic field exactly at the resonance condition described by Eq.2.4. This perturbation field is that one related to $\hat{\mathcal{H}}_{rf}$ of Eq.2.10. The r.f. field can tip the spins, and with it the magnetization when $\omega_1 \approx \omega_0$.

In a classical picture this applies a torque, $\boldsymbol{\tau}_{tor} = \boldsymbol{\mu} \times \mathbf{B}$, to the magnetic dipoles or in a quantum magnetic description generates transitions between the two energy levels. Classically the torque corresponds to a displacement of the magnetization vector described by the following equation of motion

$$\frac{\mathrm{d}\mathbf{M}}{\mathrm{d}t} = \gamma \mathbf{M} \times \mathbf{B} \tag{2.18}$$

where $\mathbf{B}$ consists of both, the static applied field $\mathbf{B_0} = (0, 0, B_0)$ defining the z-direction, and the magnetic vector of the radio frequency field $\mathbf{B_1}$. The latter can be thought of as a field rotating in the x–y plane at angular frequency $\omega_1 = \omega_0$. Thus the classical picture of the $\mathbf{B}$ components are

$$\mathbf{B} = (B_1 \cos(\omega_0 t), -B_1 \sin(\omega_0 t), B_0) \tag{2.19}$$

Equations 2.18 and 2.19 may then be combined to give three equations for the time dependence of the components of $\mathbf{M}$, also known as the Bloch equations:

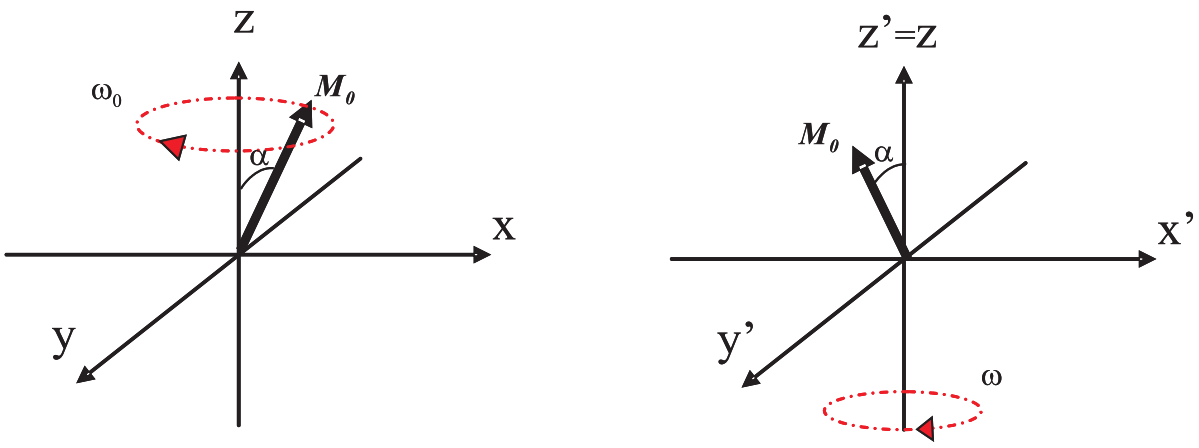

Figure 2.2: Representation of magnetization vector M_0 tipped by an angle α: (a) in a static reference frame, where it precesses around the z-axis and (b) in the rotating coordinate frame (*RCF*), where the magnetization vector appears static if the entire coordinate frame rotates with the angular frequency $\omega \approx \omega_0$ around the z-direction.

$$\begin{aligned} \frac{dM_x}{dt} &= \gamma[M_y B_0 - M_z B_1 \sin(\omega_0 t)] \\ \frac{dM_y}{dt} &= \gamma[-M_x B_0 + M_z B_1 \cos(\omega_0 t)] \\ \frac{dM_z}{dt} &= \gamma[M_x B_1 \cos(\omega_0 t) + M_y B_1 \sin(\omega_0 t)] \end{aligned} \tag{2.20}$$

These equations are not yet complete, since they do not account for relaxation times.

2.2 The rotating coordinate frame

In a classical representation, the magnetization is viewed as a vector aligned with the external magnetic field. The perturbation/excitation field B_1 causes then a complex motion of this vector by moving it away from the z-axis in spiral with frequency ω_0 as explained by Eq.2.20. To simplify the description of NMR experiments, the concept of the rotating coordinate frame $(RCF : x', y', z' = z)$ is introduced, which rotates at an angular velocity of $\omega = \omega_0$ around the z-axis, as illustrated by Fig.2.2. Hence, the notation of the magnetization vector during an NMR experiment greatly simplifies.

Equation 2.18 in the *RCF* (rotating with angular frequency ω) is then derived from the static frame of reference by

$$\left(\frac{d\mathbf{M}}{dt}\right)_{RCF} = \left(\frac{d\mathbf{M}}{dt}\right)_{Static} + \mathbf{M}\times\boldsymbol{\omega} \tag{2.21}$$

rearranging terms in this equation, the following is obtained

$$\left(\frac{d\mathbf{M}}{dt}\right)_{RCF} = \gamma\mathbf{M}\times\mathbf{B} + \gamma\mathbf{M}\times\boldsymbol{\omega}/\gamma = \gamma\mathbf{M}\times\mathbf{B}_{eff} \tag{2.22}$$

where the term $\boldsymbol{\omega}/\gamma$ has the dimensions of a magnetic field and can be considered a "fictitious" field, $\mathbf{B}_{eff}$, that arises from the effect of the rotation, with

$$\mathbf{B}_{eff} = \mathbf{B} + \boldsymbol{\omega}/\gamma \tag{2.23}$$

Equation 2.22 demonstrates that the ordinary equations of motion applicable in the laboratory frame are valid in the rotating frame as well, provided $\mathbf{B}_{eff}$, as defined in the Bloch equations, is used in place of $\mathbf{B}$. Hence the complete expression is

$$\mathbf{B}_{eff} = \mathbf{B}_0 + \boldsymbol{\omega}/\gamma + \mathbf{B}_1 = \frac{\omega_0 - \omega}{\gamma}\mathbf{e}_z + \mathbf{B}_1 \tag{2.24}$$

2.3 Relaxation times

The return to the equilibrium of the magnetization after an excitation pulse is dominated basically by two characteristics processes; one related to the magnetic field alignment and the other to the loss of phase coherence in the detected signal, i.e. in the rotating *x–y* plane.

2.3.1 Spin-Lattice Relaxation

The application of a $\pi/2$ pulse perturbs the spins from their thermal equilibrium causing the net magnetization M_0 to rotate into the *x–y* plane, while the longitudinal component M_z becomes zero. After the application of the pulse, the spins tend to return back to equilibrium by exchanging energy with their surrounding neighborhood, the so-called lattice. This is achieved through a relaxation mechanism which is called "spin-lattice relaxation" and it is described by the spin-lattice relaxation time T_1. This relaxation describes the restoration of M_z back to its initial value M_0 after the application of the $\pi/2$ pulse. The relaxation rate of M_z is described by the equation

$$\frac{dM_z}{dt} = -\frac{M_z - M_0}{T_1} \tag{2.25}$$

with the solution

$$M_z(t) = M_0\left(1 - e^{-t/T_1}\right). \tag{2.26}$$

In the case of laser polarized gases, T_1 is also the characteristic time of the ensemble to recover the thermal equilibrium to M_0. However, as for optical pumped gas the magnetization exceeds the thermal one, T_1 does not describe a magnetization recovery, but a decay without the need of applying any r.f. pulse. In other words, it can be described as a polarization decay to the Boltzmann magnetization, M_0, given by

$$M_z(t) = M(0)e^{-t/T_1} + M_0 \tag{2.27}$$

where T_1 depends mainly on the following relaxation mechanisms:

$$\frac{1}{T_1} = \frac{1}{T_1^{Grad}} + \frac{1}{T_1^{Wall}} + \frac{1}{T_1^{Dip}} + \frac{1}{T_1^{O2}} + \left(\frac{1}{T_1^{vdWalls}} \text{ in the case of Xe}\right) \tag{2.28}$$

which are described in the following:

- Gradient relaxation

In the presence of a magnetic field gradient, a moving atom will experience different magnetic field strengths. If the field fluctuations are close to the transition frequency $\omega = |\Delta E|/\hbar$ between Zeemann energy levels of Eq.2.3, then spin flips can be induced, what result in a destruction of polarization with the following rate [Sche65]

$$\frac{1}{T_1^{Grad}} = D\left(\frac{|\nabla B_x|^2 + |\nabla B_y|^2}{B_0^2}\right) \tag{2.29}$$

where $\frac{|\nabla B_x|^2 + |\nabla B_y|^2}{B_0^2}$ is the relative transversal gradient and D is the diffusion coefficient. This relation is only valid when the magnetic field and the gas pressure[1] are sufficiently large, so that

$$\frac{\omega_0 r^2}{D} >> 1 \tag{2.30}$$

where ω_0 is the Larmor frequency and r is the radius of the gas container [Cate88].

- Wall Relaxation

[1] see Eq.4.13.

The surface relaxation mechanisms of laser polarized gases are complex [Fitz69] [Drie95], however can be outlined as

$$\frac{1}{T_1^{Wall}} = \frac{1}{\eta}\frac{S}{V} \tag{2.31}$$

where $\frac{S}{V}$ is the surface-to-volume ratio of the gas container and η is a coefficient dependent on the surface material, the temperature, and the magnetic field strength. Additionally, it is shown [Schm04] that small quantities of ferromagnetic materials in glass cells, which are commonly used to store laser polarized gases, can dominate the relaxation process due to magnetization if the cells have been close to strong magnetic fields. The characteristic hysteresis curve have been also observed in such cases where the relaxation time of ^{3}He is reduced from 200 *hours* to 10 *hours* [Schm06] [Schm06b].

- Dipolar Relaxation

Dipolar relaxation is caused by atomic collisions, during which nuclear spins couple via magnetic dipole interaction, transferring their energy into a relative angular momentum. As a result, the nuclear polarization is lost. The resulting relaxation rates at room temperature have been derived for ^{3}He [Newb93] and ^{129}Xe [Hunt63]:

$$\frac{1}{T_1^{Dip}} = \frac{p}{817h \cdot bar} \quad \text{for } ^3\text{He} \tag{2.32}$$

and

$$\frac{1}{T_1^{Dip}} = \frac{p}{61h \cdot bar} \quad \text{for } ^{129}\text{Xe} \tag{2.33}$$

where p is given in *bar* and h means hours. This relaxation effect is only relevant at high pressures limiting long storages.

- Paramagnetic oxygen

Paramagnetic gases are also important as a depolarization factor. The most important paramagnetic gas is oxygen since it is usually inevitable in medical research. The oxygen-induced depolarization rate has been empirically determined for ^{129}Xe [Jame88] and ^{3}He [Saam95] according to

$$\frac{1}{T_1^{O2}} = 0.45\frac{p_{O2}}{1.013}\frac{273}{T}\left(\frac{299}{T}\right)^{0.42} \quad \text{for } ^3\text{He} \tag{2.34}$$

and

$$\frac{1}{T_1^{O2}} = 0.388\frac{p_{O2}}{1.013}\frac{273}{T}\left(\frac{300}{T}\right)^{0.03} \quad \text{for } ^{129}\text{Xe} \tag{2.35}$$

given in $1/s$, T in kelvin and the oxygen partial pressure p_{O2} in *bar*. These equations are valid for a temperature range from $200K$ to $400K$.

- Van der Waals Bound

Chann *et al.* [Chan02] reported a new mechanism of depolarization for ^{129}Xe given by the spin rotation coupling in bound Xe–Xe van der Waals molecules. Under usual clinical conditions, this kind of relaxation can be considered as constant

$$\frac{1}{T_1^{vdWaals}} = 0.24h^{-1}. \tag{2.36}$$

2.3.2 Spin–Spin Relaxation

Following the $\pi/2$ pulse, the tipped spins in the rotating transverse *x*–*y* plane have phase coherence but soon they move out of phase due to field inhomogeneities, internuclear dipole–dipole interactions, chemical shift, and other types of inter-nuclear interactions. This loss of phase coherence is called "spin–spin relaxation" and it is described by the spin–spin relaxation time T_2. The rate of change of the magnetization in the rotating *x*–*y* plane is described by the equation:

$$\frac{\mathrm{d}M_{xy}}{\mathrm{d}t} = -\frac{M_{xy}}{T_2} \tag{2.37}$$

resulting

$$M_{xy} = M_{xy}(0)e^{-t/T_2} \tag{2.38}$$

In solids, internuclear dipole–dipole interactions are profound and they cause very strong relaxation with a short T_2, while in liquids and gases these interactions are usually averaged out due to the Brownian movement of the particles which results in $T_2 \lesssim T_1$.

- Free Induction Decay (FID)

In pulsed NMR-experiments an intense r.f. pulse with an effective amplitude B_1 is applied (see Eq.2.10). The direction of notation of the magnetization in the rotating coordinate frame (*RCF*) is described by the phase of the pulse, which defines the direction of $\mathbf{B}_1$ in the *x*–*y* plane. Then the magnetization will rotate about $\mathbf{B}_1$ with an angular velocity $\omega_1 = \gamma B_1$. A pulse of duration t_p will therefore tip the magnetization by an angle $\alpha = \gamma B_1 t_p$.

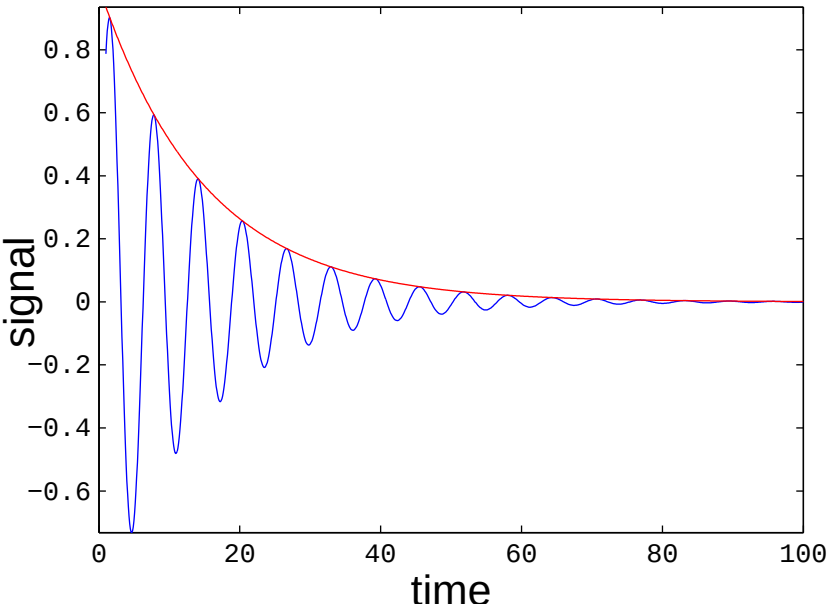

Figure 2.3: Free Induction Decay (FID), in blue, showing the exponential decay with T_2^* , in red. The oscillation is due to a small offset from the Larmor frequency which leads to the beat frequency $\Delta\omega = \omega - \omega_0$ (see Fig.2.2).

The pulses are then classified by this tip angle and the r.f. phase (e.g. *x* pulse, which rotates **M** around the rotating *x*', see Fig.2.2). The oscillation of the macroscopic magnetization induces a small alternating current in the receiver coil. This sinusoidal oscillating current at ω_0 decays exponentially with time, see Fig.2.3.

In inhomogeneous B_0 fields, the rotating spins in the transverse plane experience different fields and rotate at slightly different angular frequencies. This leads to an additional loss of phase coherence which causes the signal to decay more quickly than the time constant T_2. This signal decay, which is generally met (see Fig.2.3), is called the "Free Induction Decay" (FID) and it is characterized by the time constant T_2^* in the rotating *x*–*y* plane (considering ($T_2^* << T_1$)):

$$M_{xy}(t) = M_0 e^{-t/T_2^*}, \tag{2.39}$$

where at time $t = 0$ the $\pi/2$-pulse is applied, and the relation between the T_2 and T_2^* time constants is given by the equation

$$\frac{1}{T_2^*} \equiv \frac{1}{T_2} + \frac{1}{T_2'} + \gamma \Delta B_0 \tag{2.40}$$

where T_2' is an additional term which arises from local changes in the magnetic susceptibility of the sample [Haac99], and $\gamma\Delta B_0$ are inhomogeneities in the external field

experienced by the spin (usually due to the movement of the particle).

2.3.3 Relaxation in porous media

Porous media are characterized by a large surface to volume ratio. If He and Xe are inside a porous media at room temperature and ambient pressure, with pores sizes smaller than $1mm$, during a normal acquisition time of $1ms$ they can easily collide with the pore walls due to their diffusional motion (see section 2.6). Then the decay factor $1/T_1^{Wall}$ can be the dominant decay time in Eq.2.28.

One relaxation mechanism for spins in pores involves the presence of strong relaxation *sinks* at the pore surface [Call91]. These *sinks* may be due to the presence of paramagnetic centers at the surface, to dephasing caused by strong local magnetic field gradients or to the momentary reduction in rotational tumbling experienced by a molecule as it adheres to the surface.

Clearly the ratio of the pore surface to pore volume will vary according to the pore size so that a priori we might expect the overall relaxation behaviour to be similarly size dependent. The problem can be solved by a classical "magnetization diffusion" approach of the Bloch equations assigning a spatially magnetization distribution, $\rho_m(\mathbf{r},t)$, which obeys the following differential equations [Brow79]:

$$D\nabla^2\rho_m = \frac{\partial\rho_m}{\partial t} \tag{2.41}$$

and

$$(D\mathbf{n}\nabla\rho_m + \eta\rho_m)_{\text{surf}} = 0 \tag{2.42}$$

where $\mathbf{n}$ is the unitary vector perpendicular to the surface and η the sink strength [Call91].

Equation 2.41 is applied within the volume of the pore and Eq.2.42 in the surface. In general the solution takes the form of a sum of normal modes which depend on the geometry and η :

$$S(t) = S(0)\sum_{i=0}^{\infty} A_i e^{-t/\tau_i} \tag{2.43}$$

assuming the initial condition $\rho_m(\mathbf{r},0)) = S(0)/V$. This equation can describe either the T_1 or T_2 relaxation process, depending on the value of η chosen. The parameters which determine A_i and τ_i are the molecular self-diffusion coefficient, D, the pore size, and the average value of η over the surface. This last parameter is somewhat empirical and a variety of methods are employed in its estimation [Call91].

2.4 Magnetic Field Gradients

Spatial information can be introduced in NMR in a straight-forward way, by making the observed frequency spatially dependent. The easiest way to realize this is to perform the experiment with an additional spatially varying magnetic field, $\mathbf{B}_r(\mathbf{r})$, where $\omega_r(\mathbf{r}) = \gamma B_r(\mathbf{r})$, which is superposed to the static magnetic field $\mathbf{B}_0$ as $\mathbf{B}(\mathbf{r}) = \mathbf{B}_0 + \mathbf{B}_r(\mathbf{r})$. Usually this additional field has a linear dependence on space i.e. a constant gradient.

For instance a magnetic field gradient in the x-direction is given by $G_x \equiv \frac{\partial B_r(\mathbf{r})}{\partial x}$ and will cause the following dependence of the NMR-frequency on space

$$\omega(x) = \gamma B_x = \gamma\left(B_0 + x\frac{\partial B_r(\mathbf{r})}{\partial x}\right) = \gamma(B_0 + xG_x) = \omega_0 + \gamma G_x x\,. \tag{2.44}$$

2.4.1 Spatially dependent NMR signals, k-space

Without any field variation and without any motion of the spins, the NMR signal can be expressed as a spatial integral with a local weighting factor, $\rho(\mathbf{r})$, the spin spatially distribution density:

$$S(t) = \int_{-\infty}^{\infty} \rho(\mathbf{r}) e^{-i\gamma\omega_0 t}\mathrm{d}\mathbf{r}\,. \tag{2.45}$$

Hence, in the presence of a gradient in the x-direction the expression of Eq.2.44 has to be substituted:

$$S(t) = \int_{-\infty}^{\infty} \rho(x) e^{-i\gamma(B_0+G_x x)t}\mathrm{d}x\,. \tag{2.46}$$

Mansfield [Mans73] introduced the concept of a reciprocal space vector, $\mathbf{k}$, defined by

$$\mathbf{k} \equiv \frac{\gamma}{2\pi}\int_{t1}^{t_2} \mathbf{G}(t)\mathrm{d}t \tag{2.47}$$

for a gradient lasting from t_1 to t_2. The $\mathbf{k}$-vector has a magnitude expressed in units of reciprocal space, and from Eq.2.47 it becomes clear that the $\mathbf{k}$-space may be sampled by changing either the duration of the gradient or the gradient amplitude.

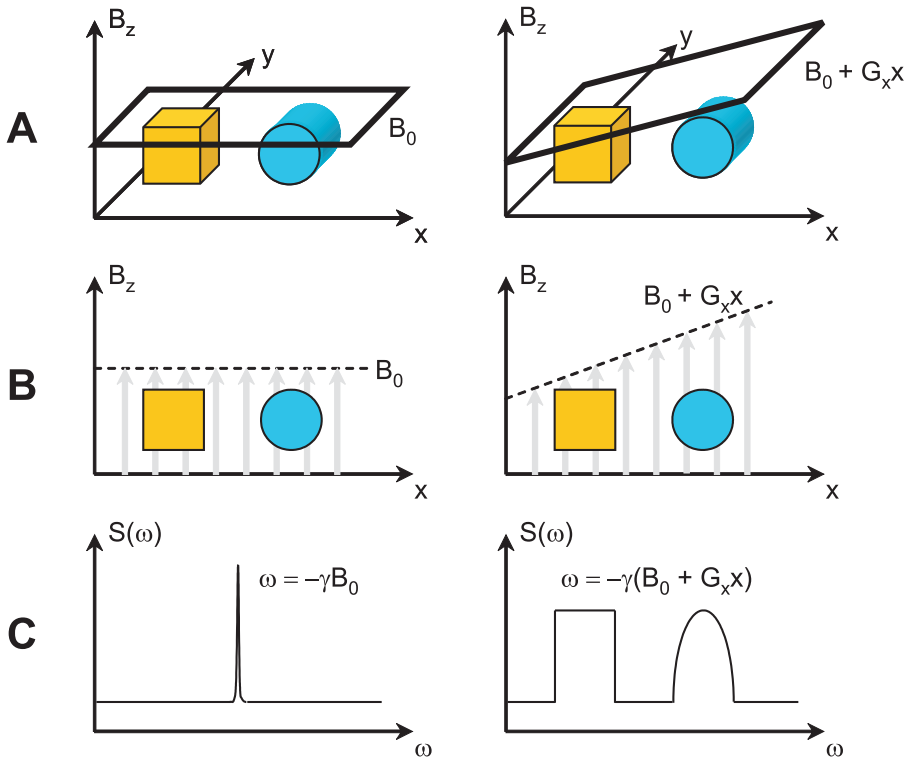

Figure 2.4: Principle of frequency encoding. The situations of two differently shaped samples in a homogeneous magnetic field (left) and with an additional gradient field (right) are shown. **A:** 3D representation of the objects. **B:** Projection along the y-axis. **C:** NMR spectra of the objects.

The frequency-encoded spatial distribution (image) can be uncovered by a Fourier transformation of the time signal in Eq.2.46,

$$\rho(x) = \frac{1}{2\pi} \int_{-\infty}^{\infty} S(k_x) e^{-i2\pi k_x x} \mathrm{d}k_x \tag{2.48}$$

which for a one dimensional case corresponds to a 1D projection of the spin density, as illustrated in Fig.2.4.

This concept can be easily be extended to two or more dimensions by introducing further gradients, e.g. for a complete 3D-image

$$\rho(\mathbf{r}) = \frac{1}{2\pi} \int_{-\infty}^{\infty} S(\mathbf{k}) e^{-i2\pi \mathbf{k}\mathbf{r}} \mathrm{d}\mathbf{k}. \tag{2.49}$$

Hence, the size and resolution of the image is defined by the way **k**-space is scanned. The **k**-vector, on the other hand, can be scaled by changing either strength

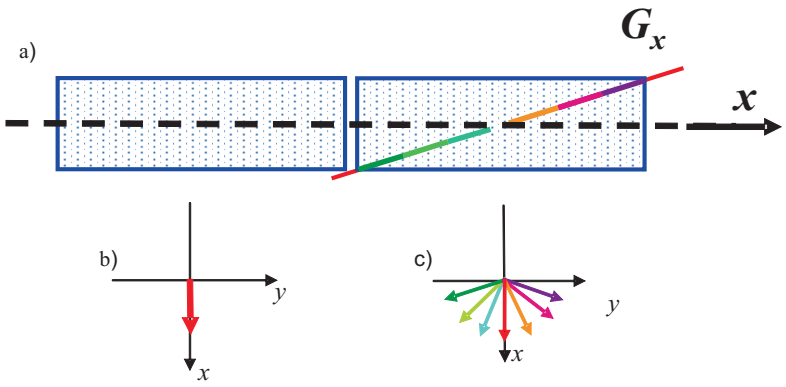

Figure 2.5: a) A gradient is applied in the x-direction of a sample (blue rectangle) b) The spin ensemble before is flipped and represented in the rotating frame (RCF) , $\phi = 0$. c) After a certain time, depending on its position (i.e. gradient strength) the spins will be dephased, $\phi = \gamma G_x x t$. The bigger the magnetic field , the more dephased are the spins.

or duration of the gradient pulses in an imaging sequence.

2.4.2 The spatial phase

As a frequency is only a temporal change of phase, $\omega = \frac{d\phi}{dt}$, Eq.2.44 can be integrated in the reference coordinate frame to

$$\phi(\mathbf{r},t) = \gamma \int_0^t \mathbf{r}(t')\mathbf{G}(t')dt' \tag{2.50}$$

which is the phase evolution at position $\mathbf{r}$ during the application of an arbitrary gradient shape, $\mathbf{G}(t')$, during time t, as shown in Fig.2.5. This also explains the loss of phase coherence in the presence of field inhomogeneities, in this case a gradient, as discussed in Eq.2.40.

For a static sample (i.e. $\mathbf{r}(t) = \mathbf{r}$) this equation simplifies to

$$\phi(\mathbf{r},t) = \gamma \mathbf{r} \int_0^t \mathbf{G}(t')dt' = 2\pi \mathbf{k}(t)\mathbf{r} \tag{2.51}$$

The product of $\mathbf{kr}$ can therefore be identified as a phase.

2.4.3 Echoes

The application of gradients rapidly dephases the NMR signal (see Fig.2.6), which makes the concept of rephasing echo sequences very favorable for the complete acquisition of the NMR signal. For NMR imaging sequences two strategies of refocusing such dephased signals are of importance, one is using r.f. pulses (the so-called Hahn- or spin-echo) and the other gradients (hence called gradient-echo).

The latter is easily understood, because Eq.2.50 already shows that any dephasing due to the application of a gradient pulse can be undone by inverting the sign of the gradient. This Gradient Echo (GE) acts as follows: an r.f. pulse excites the spins and brings a noticeable component of the magnetization into the rotating *x*–*y* plane. Subsequently, a gradient **G** induces a rapid dephasing of the spins during a time τ, resulting in a phase spread $\Delta\phi^{GE}_{dephase} = \gamma \mathbf{r}\mathbf{G}\tau$, where a static sample ($\mathbf{r}(t) = \mathbf{r}$) and rectangular gradient shape ($\mathbf{G}(t) = \mathbf{G}$) are assumed. Rephasing is achieved by inverting the gradient amplitude to $-\mathbf{G}$, so that after a time τ all phase spread is refocused $\Delta\phi^{GE}_{rephase} = \gamma \mathbf{r}(-\mathbf{G})\tau$. The total phase after a 2τ time (echo time) is $\Delta\phi^{GE}_{dephase} + \Delta\phi^{GE}_{rephase} = 0$. This is identical to the spins reaching their initial position in the *RCF* independent on their spatial position, the definition of an echo (see Fig.2.6).

The rephasing and dephasing of this echo is recorded in the presence of the 2nd gradient of Fig.2.6, which therefore must have a duration of 2τ. This corresponds to the acquisition of an horizontal line in the **k**-space (see Fig.2.7 from point 3 to point 4).

Alternatively, an echo can also be generated by inverting every phase of the spin system. This can be done by the application of a π-pulse at a time τ in the center of the sequence, which inverts the phase distribution symmetrical to its direction in the *RCF*, applying the second gradient without inversion.

Such spin-echoes allow for complete rephasing independent of the field inhomogeneities (the gradient is switched on during the entire sequence without inversion). Therefore, changes in local susceptibilities and inhomogeneities of the main magnetic field are also refocused. Of course, the gradient echo misses such “extra-inhomogeneities” because it can only refocus the phase-spread due to the field inhomogeneity of the gradient field itself.

Nevertheless, the gradient echo is more favorable for samples which are not in thermal equilibrium (e.g. hyperpolarized gases). This is because so far the inhomogeneity in the $\mathbf{B_1}$ field was neglected. This is usually bigger than the imperfections in $\mathbf{B_0}$. In reality a π-pulse will therefore only cause a perfect phase inversion for a very small region of the sample and destroy significant amounts of hyperpolarization

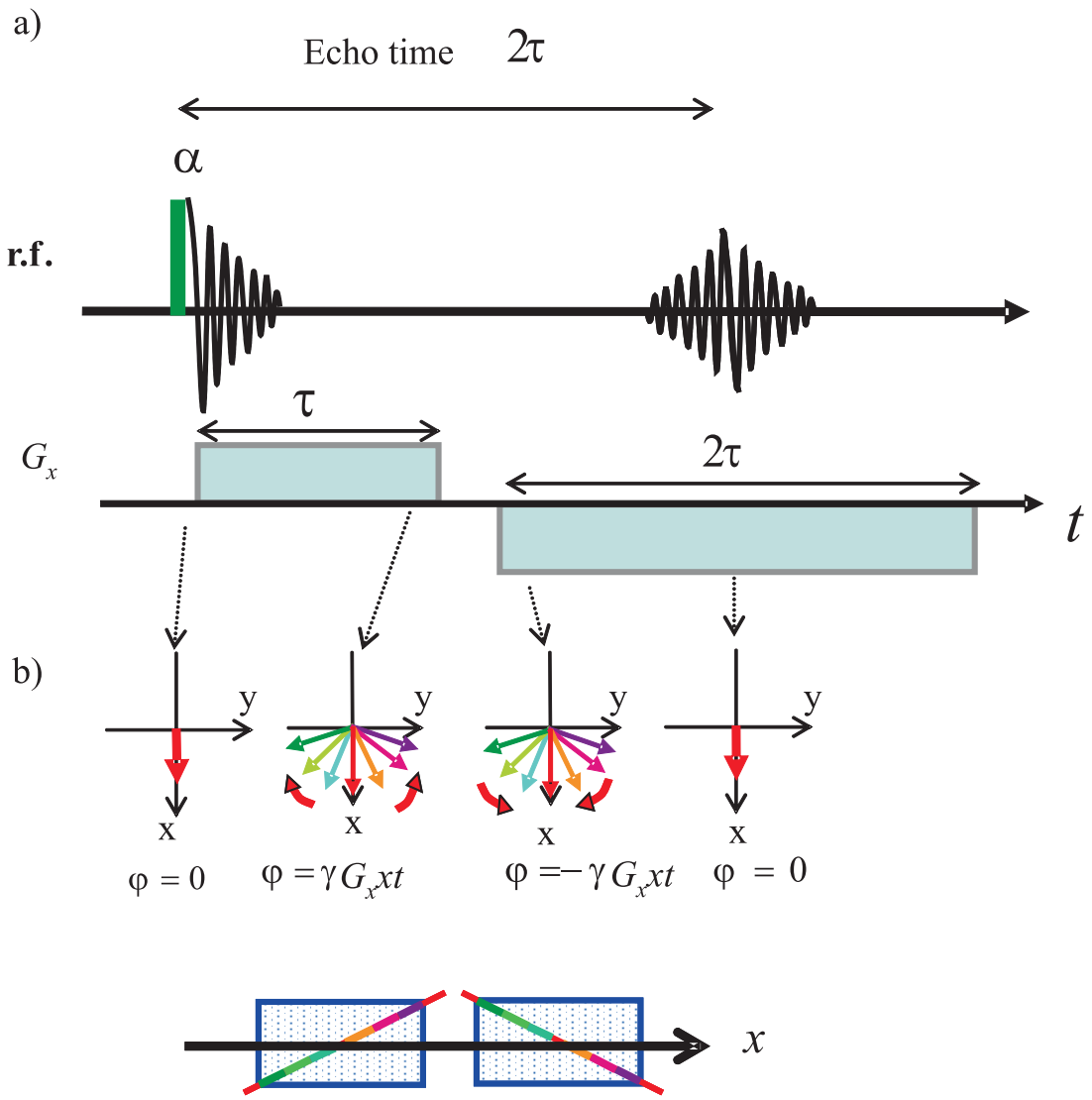

Figure 2.6: a)Graphic representation of gradient echo sequence: The top line shows the r.f. excitation (green) and the resulting NMR signals, of which the latter is the gradient echo. The central row depicts the gradient amplitude which is reversed during the second pulse to invert the phase spread, shown in b). Here the gradient is also represented over the sample as a function of space. In the *RCF* (bottom) the individual phases at different locations (indicated by color) and different times in the sequence are shown.

everywhere else. An effect less important in the case of gradient echoes, since the first and only r.f. pulse can be set to very small amplitude (typically 5°–10°) due to the large magnetization.

2.5 Spatial resolution (MRI)

So far only the concept of frequency encoding has been discussed in section 2.4. Therefore, a gradient is switched on during the sampling of the NMR signal. In order to acquire a complete trajectory in **k**-space, the **k**-vector and the associated phase, see Eq.2.51, must firstly become negative and evolve through a condition equals to zero (that is the echo maximum) to a corresponding positive value. This corresponds to a dephasing interval (points 1–2 in Fig.2.7) to achieve a maximal negative *k*-read value followed by a rephasing interval centered on the maximum of the echo (points 3–4 in Fig.2.7). Because the complete signal is recorded during this interval, the associated gradient is called "read".

The field of view (FOV), i.e. the maximum region which can be imaged, depends in general on the interval $\Delta\mathbf{k}$ used to sample the **k**-space, $FOV = 1/\Delta\mathbf{k}$ [Haac99]. In the case of frequency encoding, it depends on the sampling time, the "dwell time" (DW) between the acquisition of two data points, and the gradient strength G_{read} as follows [Haac99]:

$$FOV_{read} = \frac{2\pi}{\gamma G_{read}\, DW} \quad \text{or} \quad FOV_{read} = \frac{n\pi}{\gamma G_{read}\tau} \tag{2.52}$$

where n is the number of sampled data points and τ is defined in Fig.2.7.

Perpendicular directions of **k**-space are then accessible by adding a phase contribution to the **k**-vector prior to sampling. This is typically done in the dephasing interval during which an additional gradient is switched on (blue stepped gradient in Fig.2.7). This sets a second component of the **k**-vector, which then points in the second dimension of **k**-space. Because only one such step is possible per "read"-trajectory, the procedure has to be incrementally repeated in separate experiments. This gradient manifests its influence on the recorded signal solely by a spatial phase, see Eq.2.51, therefore it is called the "phase" gradient.

The phase gradient is kept constant during the time τ , but its amplitude is incremented by ΔG_{phase} from experiment to experiment (see Fig.2.7). The phase change of the NMR signal is proportional to the location of the spins **r**, which solving Eq.2.51 for the sequence of Fig.2.7 gives

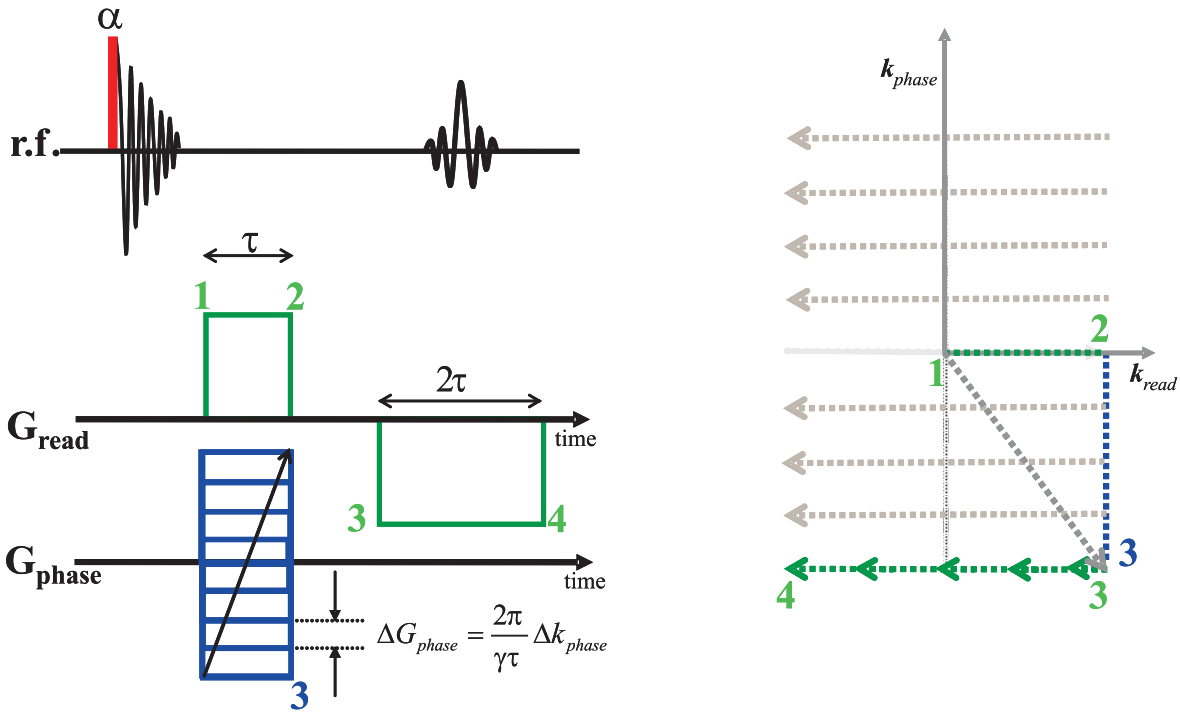

Figure 2.7: Time diagram of a 2D gradient-echo imaging sequence (left) and the resulting path through **k**-space (right): The numbers indicate the position in the **k**-space reached at certain times during the sequence. Point 1 corresponds to $\mathbf{k} = (0,0)$. The read gradient dephases the spins, hence pushing the associated component, *k*-read, to its positive maximum. However, at the same time an orthogonal gradient adds another phase contribution, resulting in a **k**-vector pointing to 3. A gradient inversion subsequently begins to invert the phase evolution of the spin system. Then the rephasing starts, and the NMR signal is acquired (marked with green arrows). Leaving the read gradient on for twice the dephasing duration, τ, samples a complete horizontal line in **k**-space (from point 3 to 4). In repeating this process for different strengths of the phase gradient, the entire **k**-space is sampled.

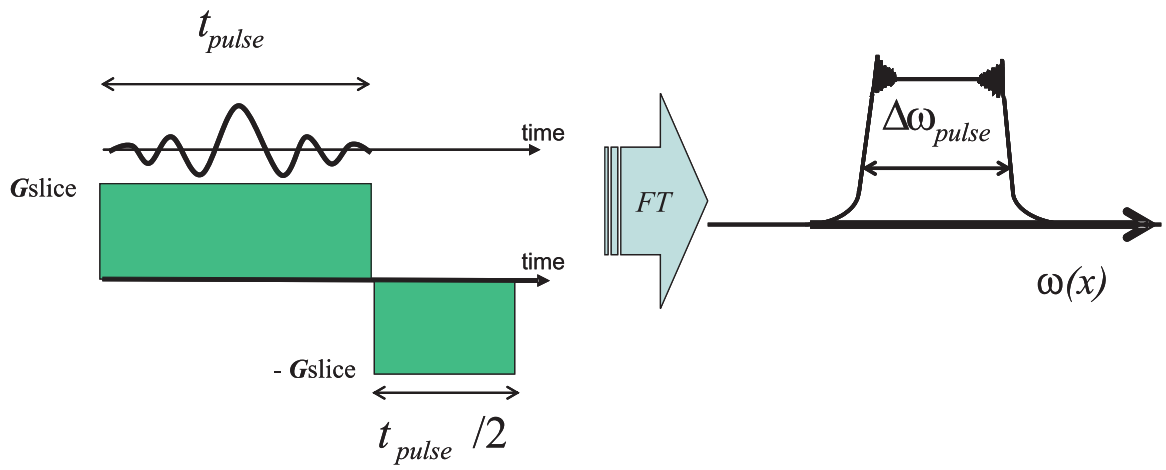

Figure 2.8: Slice selection pulse: a *sinc* shaped pulse in the time domain represents a square frequency selection after Fourier transformation. By parallel application of a bipolar gradient, only spins in a certain slice of the sample are escited (see text for details).

$$\Delta\phi = \gamma\tau\Delta\mathbf{G}_{phase}\mathbf{r} \tag{2.53}$$

Hence, for this method, the **k**-space is sampled by incrementing G_{phase} instead of the time, and the FOV is given by [Haac99]

$$FOV_{Phase} = \frac{2\pi}{\gamma\Delta G_{phase}\tau}. \tag{2.54}$$

Typically a combination of both, frequency and phase encoding techniques, are used as shown in Fig.2.7.

The concept of **k**-space sampling can easily be extended to 3D by adding a second phase gradient to the sequence, which is then stepped in an independent loop. However, this is a very time consuming process and enormous data sets are produced, because a complete third dimension has to be acquired. Typically only a limited region of a sample is of interest anyway, therefore only a few slices through this volume are sufficient. Such NMR tomography can be realized by the application of slice selective r.f. excitation with shaped pulses.

The principle of selective excitation is depicted in Fig.2.8. A *sinc*-shaped pulse $(\sin(x)/x)$ excites a rectangular spectrum in the frequency domain. In a first approximation the excitation pulse length t_{pulse} is inversely proportional to the spectral width $\Delta\omega_{pulse}$ excited by this pulse, see Fig.2.8.

A long “soft” pulse, which is often modulated in shape, can therefore selectively excite only a part of the whole spectrum. In presence of a gradient, this leads to a slice

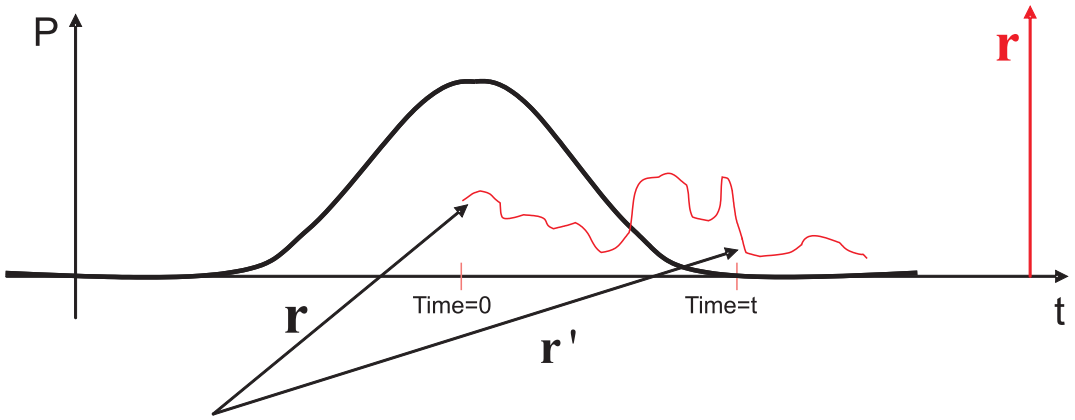

Figure 2.9: Representation of self-diffusion: translation of a particle in space and time (trajectory and axis in red) and, superposed in black, its probability function for moving from $\mathbf{r}$ to $\mathbf{r}'$ in a time t. The probability is a Gaussian described by Eq.2.60.

selection, as the spectrum is the projection of the sample along the gradient direction (see Fig.2.4). As the phases of the excited spins start to dephase already during the time of the slice selection pulse under influence of the gradient, usually a refocusing gradient pulse is applied with inverted amplitude and half the time of the r.f. pulse (see Fig.2.8). Hereby, ideally all spin phases in the slice are refocused.

2.6 Diffusion

Diffusion is usually defined as the transport of matter (gas, liquid or solid mixtures) by relative movement of the particles in concentration, temperature or pressure gradients.

2.6.1 Statistical description

The classical description of diffusion is given by Fick's laws, (diffusion at constant temperature and pressure).

$$\mathbf{J}(\mathbf{r},t) = -D\nabla c(\mathbf{r},t) \tag{2.55}$$

This equation states that a gradient of concentrations, $\nabla c(\mathbf{r},t)$, is proportional to the induced flux of matter, $\mathbf{J}(\mathbf{r},t)$, where $\mathbf{r}$ is the position of the particle at the time t, as defined in Fig.2.9. The factor of proportionality is the diffusion coefficient, or more generally the diffusion tensor. It is a tensor because matter can diffuse differently depending on the direction.

Combining the continuity equation

$$\frac{\partial c(\mathbf{r},t)}{\partial t} = -\nabla \mathbf{J}(\mathbf{r},t) \tag{2.56}$$

with Eq.2.55, Fick's second law is obtained to describe the temporal behaviour of the concentration

$$\frac{\partial c(\mathbf{r},t)}{\partial t} = \nabla D \nabla c(\mathbf{r},t) \tag{2.57}$$

However this model of diffusion does not give a good explanation of the movement of a particle when the concentration plays no role, i.e. when the particle is moving in the absence of a concentration gradient, the so called self-diffusion. Self-diffusion is the random translational motion of molecules driven by internal kinetic energy, it is also closely related to molecular size, as it can be seen from the Stokes-Einstein equation :

$$D = \frac{k_B T}{f_r} \tag{2.58}$$

where T is the temperature of the system, f_r is the friction coefficient and D is the scalar diffusion coefficient, i.e. the diffusion tensor when it is completely isotropic. The friction coefficient f_r is not easy to calculate because molecular shapes are complicated and may include contributions from factors such as hydration. Therefore, a statistical description of self-diffusion is usually more successful. For this purpose a correlation function $P(\mathbf{r}|\mathbf{r}',t)$, which describes the probability of the movement of a particle from $\mathbf{r}$ to $\mathbf{r}'$ in a time t, is introduced. This correlation function also follows Fick's second law:

$$\frac{\partial P(\mathbf{r}|\mathbf{r}',t)}{\partial t} = \nabla D \nabla P(\mathbf{r}|\mathbf{r}',t). \tag{2.59}$$

For isotropic diffusion a solution of Eq.2.59 is a Gaussian, as depicted in Fig.2.9[Call91]

$$P(\mathbf{r}|\mathbf{r}',t) = \frac{e^{-(\mathbf{r}'-\mathbf{r})^2/(4Dt)}}{\sqrt{(4\pi D t)^3}}. \tag{2.60}$$

Another important parameter for the description of diffusion is the mean path that the particle travels during a certain time. This parameter is also known as the mean square displacement and is given by the Einstein-Smoluchowski equation [Eins05] [Smol06]:

$$\left\langle (\mathbf{r}' - \mathbf{r})^2 \right\rangle = 2nDt \tag{2.61}$$

where n is the number of dimensions in which the particle is allowed to move [Call91].

2.6.2 Restricted Diffusion

The considerations made above are only valid for particles which are allowed to move everywhere, resulting in a Gaussian probability. However, reality is different and usually diffusion is spatially restricted. In such a case the probability function will be different and harder to calculate. Therefore, ξ, a ratio between the measured (experimental or apparent) diffusion coefficient, $ADC(t)$, which is generally time dependent and the diffusion coefficient for the free diffusion (unrestricted), D, is defined [Pric97]. This dimensionless variable ξ will indicate the level of restriction due to obstacles.

$$\xi(t) \equiv \frac{2\,n\,ADC(t)\,t}{\left\langle (\mathbf{r}' - \mathbf{r})^2 \right\rangle_{free}} \tag{2.62}$$

where $\left\langle (\mathbf{r}' - \mathbf{r})^2 \right\rangle_{free}$ is the mean square displacement of the particle when it diffuses freely.

There will be two different regimes of ξ depending on the time used to measure the diffusion. Measurements for a short time do not allow the particles to collide extensively with the walls that limit the movement ($ADC \approx D$). On the other hand in long time limit measurements of the mean square displacement of the particle have to be the cavity size ($ADC < D$).

If the shape of the cavity deviates from a sphere, then the observed diffusion coefficient also depends on the direction of the measurement. In the case of a cylinder parallel to the z-axis, as shown in Fig.2.10, the diffusion in the x- or y-direction is restricted by the diameter while it is free along the z-direction

Thus the diffusion coefficient becomes a tensor. In real samples this is the most common case and the most general description. Because of the sign independence of the diffusing particle mean path $\left\langle (\mathbf{r}' - \mathbf{r})^2 \right\rangle$, the tensor is symmetric and can be written as:

$$\underline{D} = \begin{pmatrix} D_{11} & D_{12} & D_{13} \\ D_{12} & D_{22} & D_{23} \\ D_{13} & D_{23} & D_{33} \end{pmatrix}.$$

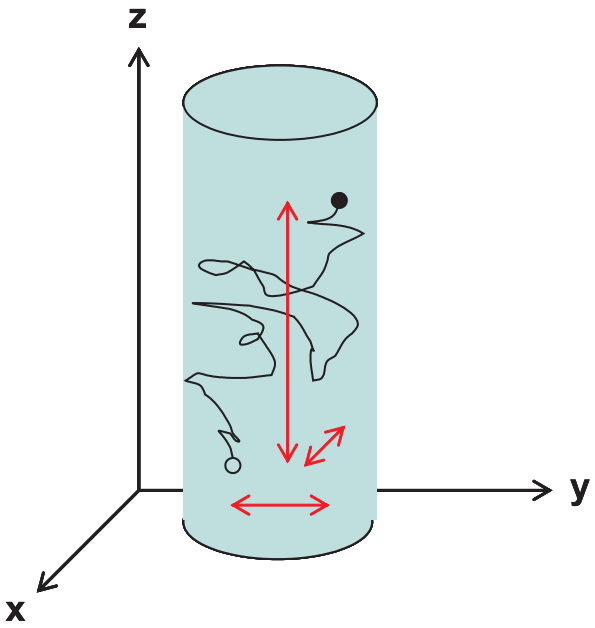

Figure 2.10: Particle diffusing inside a cylinder parallel to the *z*-axis. The empty circle represents a particle when its position is initially encoded and the full one when the measurement stops. The red arrows shows the mean square displacement along to each axis.

2.6.3 Determination of the diffusion coefficient by NMR

Because diffusion is defined by the distance a particle travels randomly in a certain time, it is clear that spatially varying magnetic fields, i.e. field gradients, can be used to observe its influence on the NMR signal. Therefore, two gradients of identical intensity and duration but opposite direction are added to a FLASH sequence [Haas86], as shown in Fig.2.11 (a). In case of static particles , the dephasing of the spins during the first gradient is perfectly rephased and results in an not attenuated echo, see Fig.2.11 (b). However if the particles diffuse, they change their position during the experiment and hence their phase spread is no longer refocused perfectly, resulting in an attenuation of the echo, see Fig.2.11 (c).

This process can be expressed by rewriting Eq.2.46 in a more general form including Eq.2.60:

$$S(t,\mathbf{G}) = \int_{-\infty}^{\infty}\int_{-\infty}^{\infty} \rho(\mathbf{r})P(\mathbf{r}|\mathbf{r}',t)e^{i\gamma\int_0^t \mathbf{G}\mathbf{r}\mathrm{d}t}\,\mathrm{d}\mathbf{r}\mathrm{d}\mathbf{r}' \tag{2.63}$$

where the density, $\rho(\mathbf{r})$, is weighted by the correlation function, $P(\mathbf{r}|\mathbf{r}',t)$. To solve this equation, the magnitude and the duration of the applied gradients, as well as the

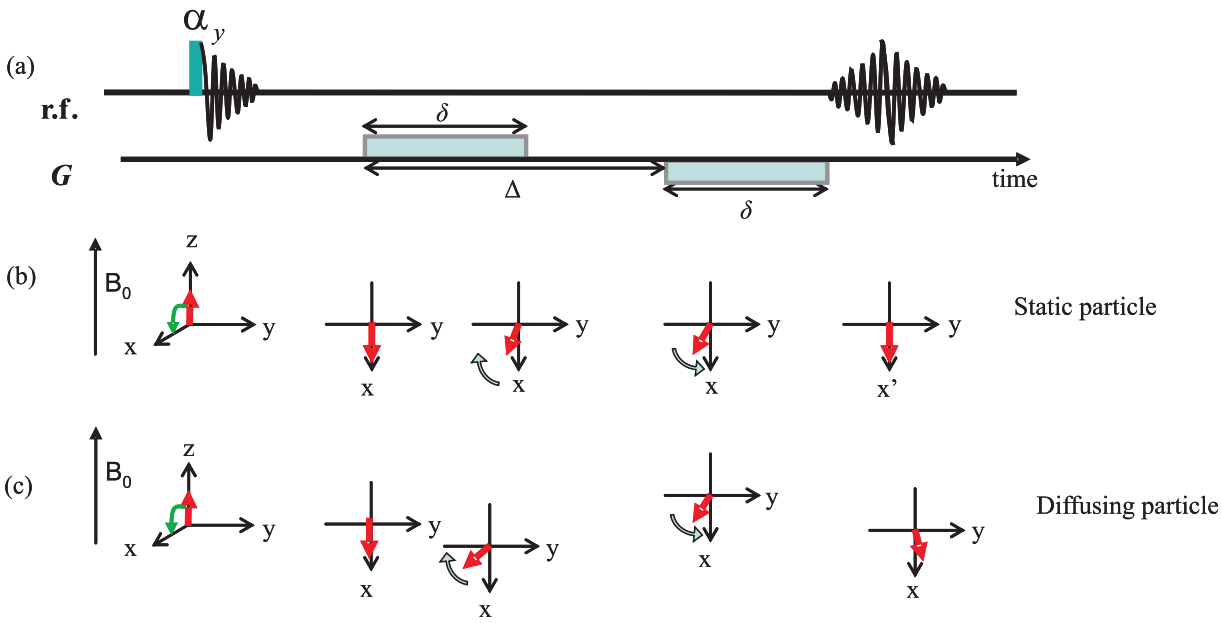

Figure 2.11: Difference of dephasing and rephasing between a diffusing particle and a static particle. Since the static particle is always at the same position in the gradient, its phase is completely refocused (as in Fig.2.6). However, as the diffusing particle moves, its spin is not completely refocused which leads to a loss of echo signal related to the diffusion.

times of the r.f. pulses, have to be known. For the sequence depicted in Fig.2.11 (a) this gives the following solution:

$$E(\mathbf{G},\delta,\Delta) = \frac{S(\mathbf{G},\delta,\Delta)}{S(0,\delta,\Delta)} = \exp\left[-\gamma^2 G^2 D\delta^2\left(\frac{\Delta-\delta}{3}\right)\right] \tag{2.64}$$

also known as Stejskal-Tanner equation [Stej65]. $E(\mathbf{G},\delta,\Delta)$ defines a normalized echo attenuation, which depends on the gradient duration, δ, and interval Δ as defined in Fig.2.11 (a). It does not depend on the density $\rho(\mathbf{r})$ since $\rho(\mathbf{r})$ is time independent.

In the absence of gradient, the echo intensity $E(0,\delta,\Delta)$ is maximal. By increasing the gradient intensity, the echo signal $E(\mathbf{G},\delta,\Delta)$ decreases due to the influence of diffusion, which leads to an imperfect refocusing of the spin phases.

Since in a real experiment, perfect rectangular gradient pulses cannot be realised, the ideal gradient shape of a step function is artificially smoothed by applying short ramps during a time ε at the beginning and the end of the pulses as depicted in Fig.2.12. The solution of Eq.2.63 for such trapezoidal gradients results in the following expression for the echo attenuation [Chen99]

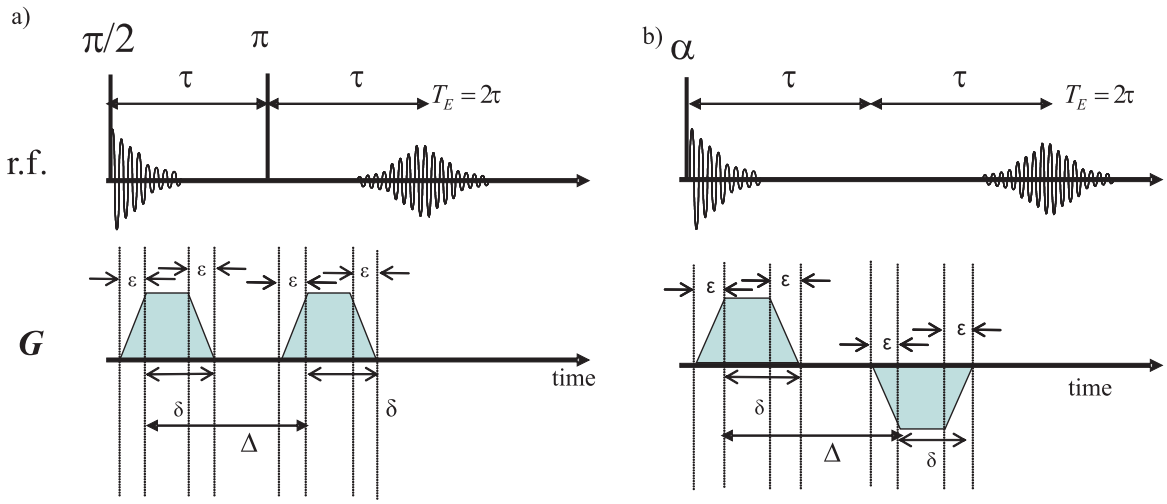

Figure 2.12: Timing diagram in the diffusion sequence for trapezoidal gradients, in a spin echo sequence, (a), and in a gradient echo sequence, (b).

$$E(\mathbf{G},\delta,\Delta) = \exp\left\{-\gamma^2 G^2 D\left[\delta^2\left(\frac{\Delta-\delta}{3}\right)+\frac{\varepsilon^3}{30}-\frac{\delta\varepsilon^2}{6}\right]\right\}. \tag{2.65}$$

Varying the strength of G in a diffusion sequence will produce a Gaussian dependence of the echo amplitude on the gradient strength. The diffusion coefficient can be obtained by fitting such curve with a linear regression of $\ln E$ versus G^2.

In the case of anisotropic diffusion, Eqs.2.65 and 2.64 have to be modified by the tensorial description of the diffusion coefficient (with ideal gradients, i.e. $\varepsilon \to 0$) [Pric97]

$$E(\mathbf{G},\delta,\Delta) = \exp\left[-\gamma^2 \mathbf{G}\underline{D}\mathbf{G}\delta^2\left(\frac{\Delta-\delta}{3}\right)\right] \tag{2.66}$$

where the product of gradients and diffusion tensor resulting in

$$\mathbf{G}\underline{D}\mathbf{G} = (G_x,G_y,G_z)\begin{pmatrix} D_{11} & D_{12} & D_{13} \\ D_{12} & D_{22} & D_{23} \\ D_{13} & D_{23} & D_{33}\end{pmatrix}\begin{pmatrix} G_x \\ G_y \\ G_z\end{pmatrix}$$

Because of the symmetric nature of the tensor only 6 different diffusion coefficients have to be determined; for example the gradient directions xx, yy, zz, xy, xz, yz in the following equation derived from Eq.2.66

$$\ln E(\mathbf{G},\delta,\Delta) = -\gamma^2\delta^2(\Delta-\delta/3)\sum_{i=x,y,z}\sum_{j=x,y,z} G_i D_{i,j} G_j. \tag{2.67}$$

Measurement in restricted geometries

In case of restricted diffusion Eq.2.59 can be no longer solved exclusively in the time domain (i.e. the NMR sequence acting on freely diffusing particles), because $P(\mathbf{r}|\mathbf{r}',t)$ then obviously has spatial "cut-offs" which have to be taken into account. This represents a severe complication and can only be solved analytically for simple geometries, which are only summarized here (for details see [Call91]). The analytical solutions for a rectangular (i.e. walls in a distance a), a cylindrical and spherical pore of radius a are listed below:

- Rectangular

$$E(q) = \frac{2-2\cos(2\pi qa)}{(2\pi qa)^2} + 4(2\pi qa)^2 \sum_i^{\infty} \exp\left(\frac{-i^2 D\Delta}{a^2}\right) \frac{-1(1-)^i \cos(2\pi qa)}{\left[(2\pi qa)^2 - (i\pi)^2\right]^2} \text{ so that } q = \frac{\gamma\delta G}{2\pi} \tag{2.68}$$

- Cylindrical

$$E(q) = \exp\left\{-2\gamma^2 G^2 \sum_i^{\infty} f(\alpha_i)\right\} \tag{2.69}$$

with

$$f(\alpha_i) = \frac{2D\delta\alpha_i^2 - 2 + 2\exp(-D\alpha_i\Delta) + 2\exp(D\alpha_i\delta) - \exp[-D\alpha_i(\Delta+\delta)] - \exp[-D\alpha_i(\Delta-\delta)]}{D^2\alpha_i^6(a2\alpha_i^2 - 1)} \tag{2.70}$$

where the α_i are the roots of the following Bessel-function equation $\alpha_i a J_0(\alpha_i a) = J_1(\alpha_i a)$.

- Spherical

$$E(q) = \exp\left\{-2\gamma^2 G^2 \sum_i^{\infty} g(\beta_i)\right\} \tag{2.71}$$

with

$$g(\beta_i) = \frac{\frac{2\delta}{\beta_i^2 D} - \frac{2+\exp[-\beta_i^2 D(\Delta-\delta)] - 2\exp[-\beta_i^2 D\delta]}{\beta_i^4 D^2} - \frac{\exp[-\beta_i^2 D(\Delta+\delta)] + \exp[\beta_i^2 D\delta]}{\beta_i^4 D^2}}{\beta_i^2(\beta_i^2 a^2 - 2)} \tag{2.72}$$

where the β_i are the roots of the following Bessel-function equation $\beta_i a J'_{3/2}(\beta_i a) = \frac{1}{2} J_{3/2}(\beta_i a)$.

2.7 Hyperpolarization Methods

Conventional NMR methods suffer from a main problem that limit their power and applicability; a notorious lack of sensitivity. This fundamental insensitivity originates from the minuscule size of nuclear magnetic moments, which results in an exceedingly small equilibrium nuclear spin polarization in even the high magnet fields, as already shown in section 2.1.2.

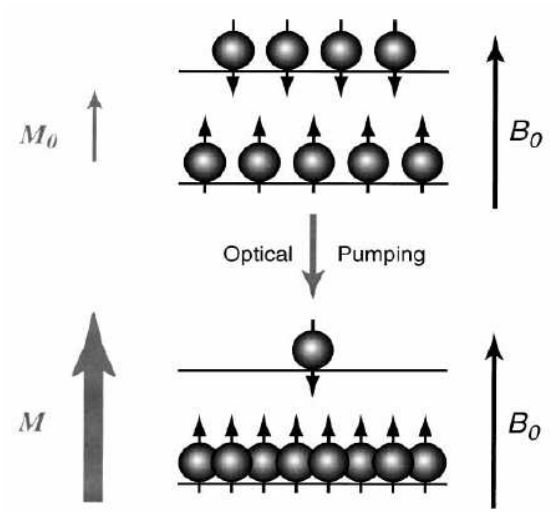

Figure 2.13: Effect of nuclear polarization of an ensemble of spin-1/2 nuclei in comparison with the Boltzmann distribution. In the top image is depicted the thermal equilibrium; the number of spins aligned anti-parallel to the magnetic field is nearly equal to the number of spins aligned parallel, resulting in a small polarization. In the bottom image is depicted the optical pumping polarization; with optical pumping the population distribution of the spins can be driven away from equilibrium, thereby increasing the polarization to order unity [Good02].

In certain systems, however, the sensitivity of NMR spectroscopy and MRI can be greatly enhanced via optical pumping. In that case, angular momentum is transferred from laser photons to electron spins and finally via magnetic coupling (hyperfine interaction) to nuclear spins, thereby temporarily enhancing the nuclear spin polarization in these systems by four to five orders of magnitude, as schematically shown in Fig.2.13.

Two methods are common to achieve optical pumping of nuclear spins of noble gases: alkali metal spin exchange, (used for ^{129}Xe or ^{3}He), [Bouc60] and metastability exchange, (used for ^{3}He) [Cole63].

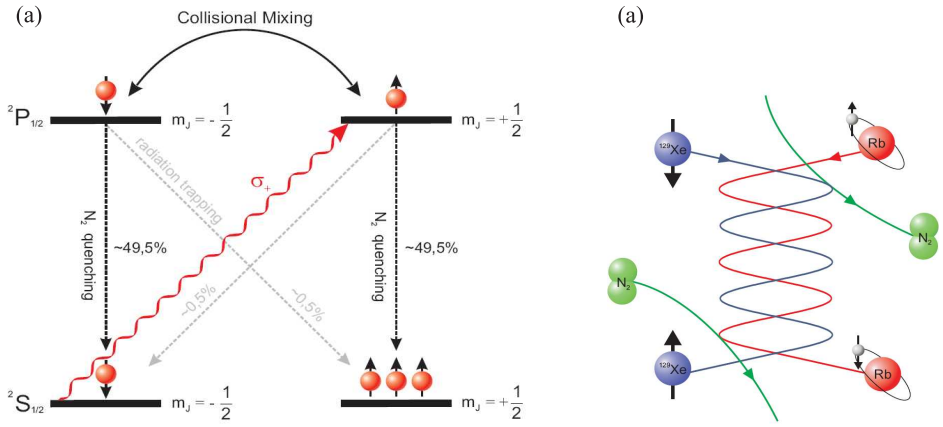

Figure 2.14: Alkali-metal optical-pumping/spin-exchange processes. (a) Optical pumping process of the D1 transition in Rb metal, by circular polarized σ_+ laser light. The excited states are mixed by gas collisions and radiation trapping is avoided by the admixture of N_2 as a quench gas. (b) Exchange via the formation of van der Waals molecules by collisions with N_2 at low pressures.

2.7.1 Alkali Metal exchange

It is well know that alkali metals vapour can be optically pumped [Good02]. Therefore using saturated rubidium vapour at temperatures between $100°C$ and $200°C$, inside a pump cell made from glass, that does not suffer damage because of chemical reactions. Rubidium vapour can be optically pumped with a circularly polarized laser light with a wave length of $\lambda = 795nm$. The optical pumping cell contains a gas admixture of ^{4}He, N_2, the isotope to polarize (^{129}Xe or ^{3}He) and the alkali metal vapour at elevated pressures (5–7*bar*). Both, ^{129}Xe or ^{3}He, can be polarized by this method, nevertheless the explanation will focus on ^{129}Xe. Nitrogen is needed to make possible non-radiative transitions to the ground state, and without N_2 the unpolarized fluorescence light will be absorbed again by the alkali atoms, thus reducing drastically the achievable electronic polarization.

The process has two steps; firstly the valence electrons of rubidium are polarized by the laser, reaching polarizations close to 1, see Fig.2.14 (a). The orientation of the electronic spins (J) is then transferred to the nucleus spin (I), in the case of ^{129}Xe by the characteristic formation of a Van der Waals molecule that links both atoms (see Fig.2.14 (b)).

Nitrogen is added to the gas mixture to quench the fluorescence of the electronically excited alkali metal atoms, which would otherwise work to depolarize the electron spins. The typically achieved polarization values are around 10–30 % for ^{129}Xe. ^{4}He is added to raise the pressure in the cell to broaden the absorption line of rubidium

by collisions.

The alkali metal exchange method is also suited for hyperpolarizing ^{3}He, but it is less effective than for ^{129}Xe. This is due to the very small collision cross section and to the fact that the probability of the formation of Van der Waals molecules in ^{3}He is much smaller, because of the smaller polarisability of the electrons shell.

2.7.2 Metastability exchange

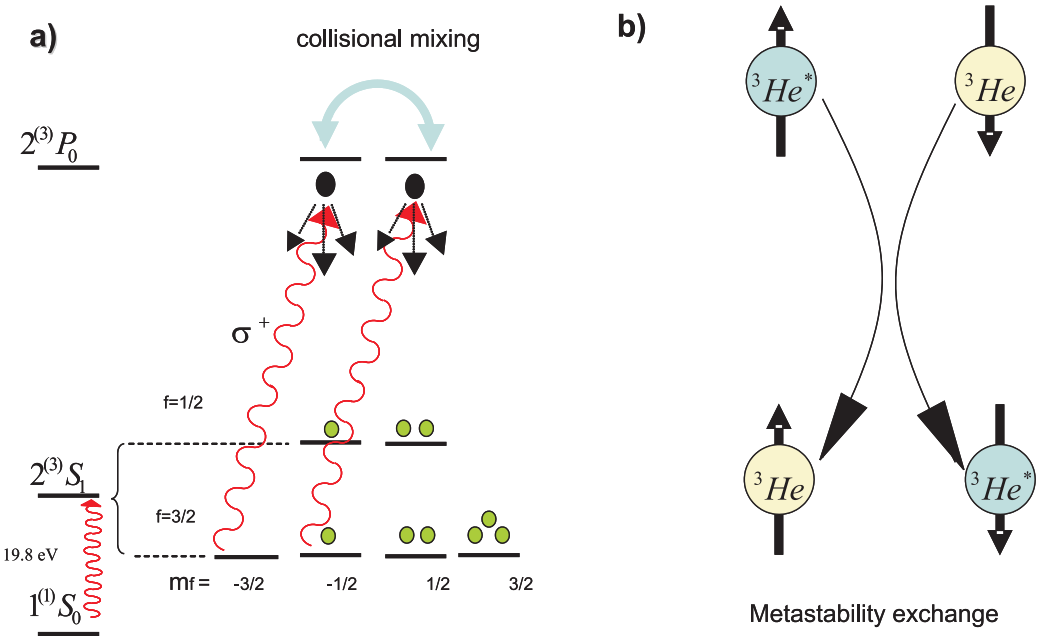

Figure 2.15: Metastability exchange: (a) relevant energy levels involved in the creation and subsequent nuclear spin polarization of metastable ^{3}He gas. (b) He*–He collisions permitting energy-conserving metastability exchange.

To hyperpolarize the ^{3}He, instead of optical pumping of an alkali metal transition, a metastable electronic state of the ^{3}He itself is pumped, which then transfers its electronic polarization to nuclear ^{3}He spin polarization. Before the ^{3}He gas can be optically pumped, a small portion of the gas must first be excited from the ground electronic state $1\,^1S_0$ into the metastable state $2\,^3S_1$, see Fig.2.15 (a); this is achieved by applying a weak r.f. discharge to the optical pumping cell. Metastable atoms can then be optically pumped by absorbing circularly polarized laser light at $\lambda = 1083nm$, which drives population from the state $2\,^3S_1$ ($F = 1/2$) level or the state $2\,^3S_1$ ($F = 3/2$) level to the $2\,^3P_0$ ($F = 1/2$) level. By collisional mixing of the excited states and isotropic reemission into the different $2\,^3S_1$ hyperfine states, the population is driven into the states with positive m_J quantum number. The polarization of the

^{3}He atom is then transferred to the nuclear state of the ground state, as is shown in Fig.2.15 (b), via so called metastability exchange collisions. In these processes the metastability is exchanged while keeping the total angular moment conserved. This means that:

$$^3He(m=-\frac{1}{2})+^3He^*(m_F) \rightleftharpoons {}^3He(m=+\frac{1}{2})+^3He^*(m_F-1)\,. \tag{2.73}$$

This is a purely electrostatic process being much more effective than the spin-exchange via hyperfine coupling. Since due to optical pumping with a σ_+-light the metastable ^{3}He* atoms with $m_F > 0$ are more populated, the above transfer reaction goes predominantly from left to right terms, populating the nuclei of the ground state atoms in the $m = 1/2$ state.

In comparison to alkali metal exchange the restriction to low pressures in metastability exchange poses the main problem, as the polarized gas has to be compressed from *mbar* order to *bar* order to accumulated sufficient amounts of gas, without losing its polarization. This problem was solved by using a compressor without any magnetic parts, as shown in [Schm04]. Hereby, polarization up to 73% are obtainable for different applications in NMR and MRI. The maximum polarization value achieved in an optimized setup inside a sealed optical pumping volume was $91\% \pm 2\%$ [Wolf04].

Chapter 3

Experimental Setup

3.1 Hyperpolarization of ^{129}Xe and ^{3}He

Two methods are common to achieve optical pumping of nuclear spins of noble gases: alkali metal spin exchange, (used for ^{129}Xe or ^{3}He), [Bouc60] and metastability exchange, (used for ^{3}He) [Cole63] (see section 2.7).

3.1.1 LP ^{129}Xe: experimental details

^{129}Xe is polarized in a home-built polarizer designed and constructed by S.Appelt and coworkers at the Research Center Jülich, Germany [Appe00], of which a sketch is shown in Fig.3.1. A high-pressure gas-bottle of xenon and buffer gases (94 % ^{4}He and 5 % N_2 and 1 % xenon) is connected to the apparatus. The ^{4}He is needed to increase the pressure to broad the absorption lines by collision. The working pressure is adjusted to $7 bars$ and the flow of this gas mixture throughout the device is controlled by a needle valve that opens to ambient pressure.

The gas flow is directed through a flow meter that measures the flux in mL/min and was usually adjusted to $200 mL/min$. Behind the flow meter the gas is mixed with rubidium vapour and allowed to enter the polarizing chamber. The rubidium vapour is produced by heating a small reservoir by a temperature controlled heat gun with the temperature usually adjusted to $140°C$ [Mühl07]. The polarization chamber is made from $5 mm$ thick glass and has plane-parallel sides where the laser light enters to excite the rubidium. The laser has two laser-diodes (Coherent Inc) producing each $30 W$ of light with a wavelength of $\lambda = 794.7 nm$. They were combined in a fiber and after a circular polarizer $\lambda/4$ plate focused on the chamber. The entire setup has to be placed in a relatively strong magnetic field of $9.32 G$ generated by a Helmholtz-coil.

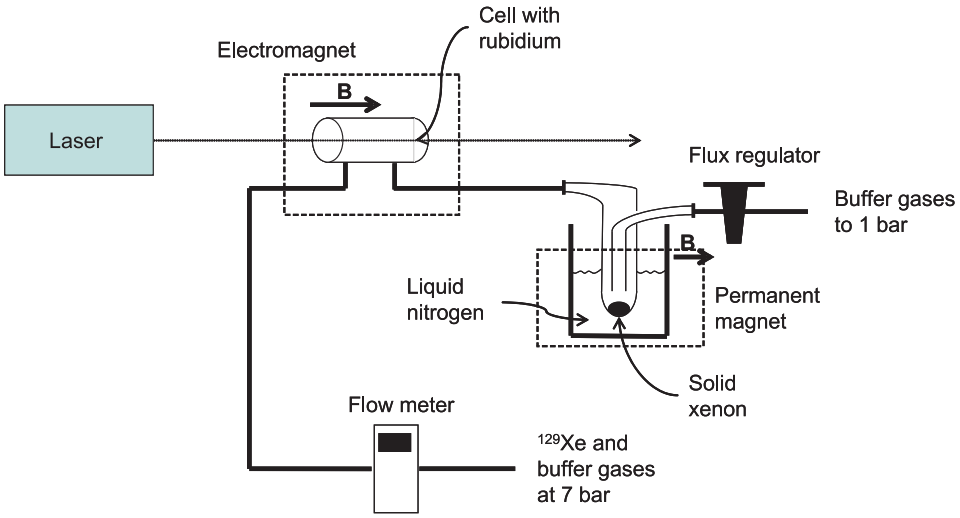

Figure 3.1: Schematic representation of the xenon-polarizer. See text for details.

The polarized xenon is then separated from the buffer gases by directing the gas flow through a cold finger, which is submerged in liquid nitrogen. However, the condensed xenon has to be stored in a relatively strong field, to avoid relaxation of ^{129}Xe via ^{131}Xe [Appe98]. Therefore, a special permanent magnet was designed (see Fig.3.2), which produced a relatively homogeneous field of 0.3 T [Blüm04].

The amounts (pressure) of hyperpolarized ^{129}Xe were controlled by the duration of the freezing time and the gas flux. Typical values were freezing times lasting between 5–20 minutes at a $300mL/min$ ($7bar$ overall pressure). The resulting pressures of xenon in a volume of $0.3L$ (after evacuating the buffer gases) at room temperature are listed in Tab.3.1.

Time$/[min]$	7.5	12	16	20
Pressure$/[bar]$	1.10 ± 0.05	1.60 ± 0.05	2.05 ± 0.05	2.35 ± 0.05

Table 3.1: Pressures of hyperpolarized xenon produced in a bottle of $0.3L$ by different polarization times. The gas flux was adjusted to $300mL/min$ and the buffer gases removed.

3.1.2 LP ^{3}He: experimental details

In Fig.3.3 a schematic drawing of the polarizer and compressor is presented. The process begins in a titanium getter, where the ^{3}He gas is purified. Then it flows throughout five glass cells, where it is excited in the metastable state by an rf-plasma. Therefore,

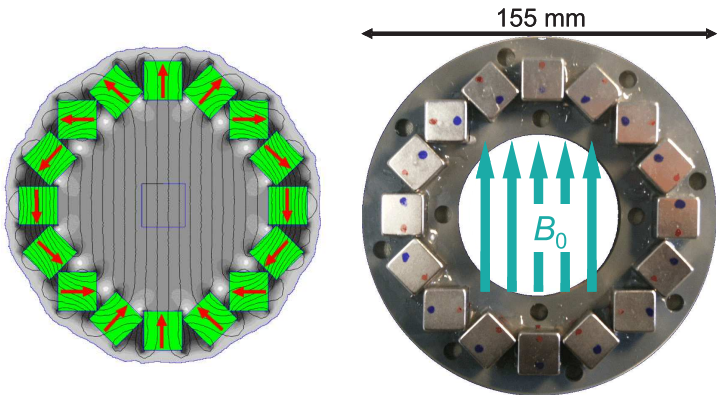

Figure 3.2: Home made magnet (Halbach design) to store the hyperpolarized ^{129}Xe. The magnet consists of an arrangement of 16 bar magnets in different orientations. Left: representation of the magnetic flux lines. The magnets are shown in green and their magnetization direction by red arrows. The gray shades depict the flux density. Right: photograph and dimensions of the finished magnet operating at a magnetic field of. $0.3T$ in its center at a total height of $250mm$ [Blüm04].

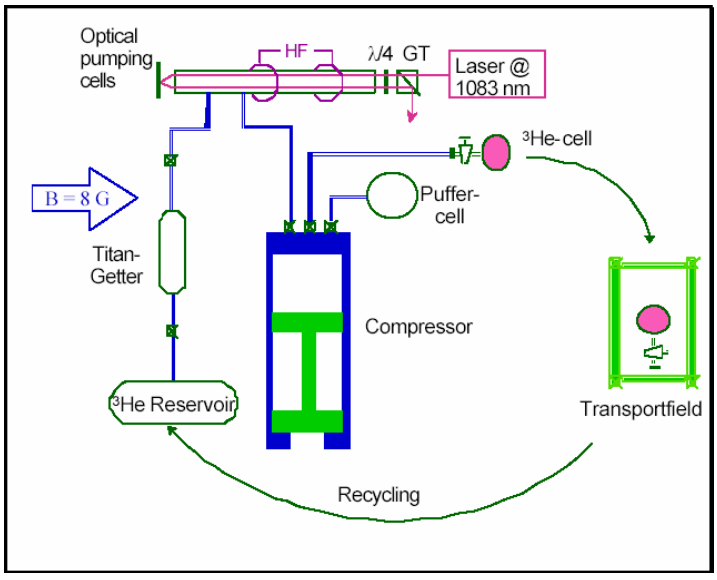

Figure 3.3: Schematic representation of the ^{3}He polarizer. Due to dimensions, only one instead of 5 optical pumping cells has been drawn. See text for details.

foil-electrodes are attached to the sides of each glass cell. A circularly polarized laser beam with a wave length $\lambda = 1083nm$ is guided through the cells. Two fiber-lasers with $15W$ each are combined to obtain sufficient power. The flow rate of the gas is adjusted to achieve a polarization in the order of 60%–80%. However, the fact that plasma has to be ignited sets an upper limit to the usable pressures, which must be in the range of $10^{-3}bar$. As a consequence the polarized ^{3}He has to be compressed to useful pressures. This is achieved by a hydraulic compressor with an interior volume of $15L$, which presses the gas in a storage deposit of $4L$ at a pressure of about $300mbar$. In a second step of compression, the gas is brought from the storage deposit to a glass transport cell. Of course the entire equipment must be placed inside a low magnet field of $8G$. With this instrumentation production rates of $3bar \cdot L/hour$ of hyperpolarized ^{3}He of $P \approx 60\%$–65% can be achieved [Schm04].

The glass transport cell is made from an alkaline-earth-alumina-silicate glass. These glass cells have a volume of ca. $1L$ and a relaxation time, T_1, up to 200 *hours*. The final pressure inside the transport cell is ca. 3 *bar*.

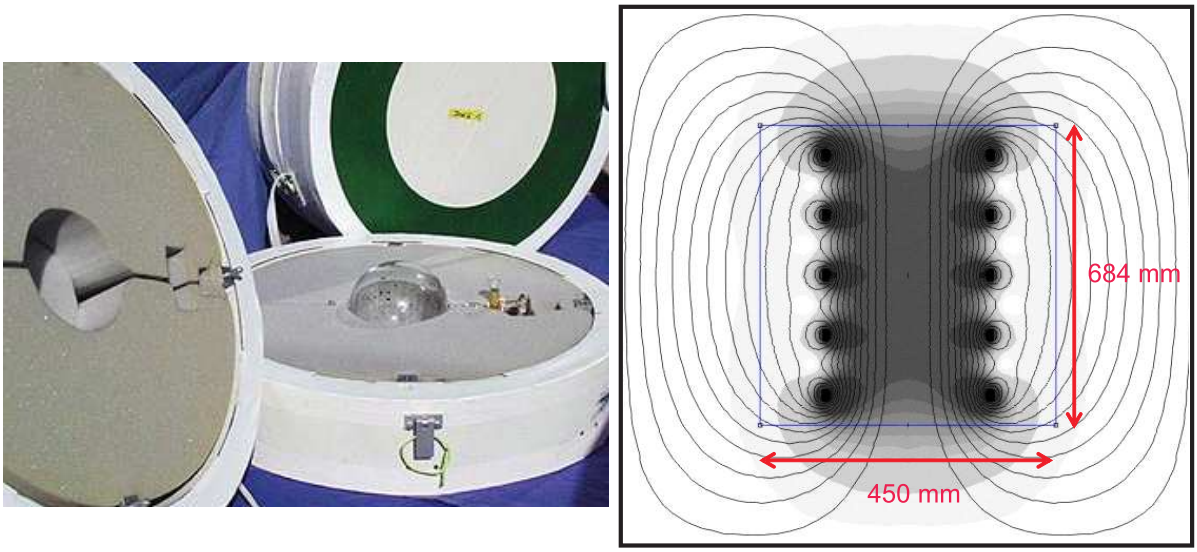

Figure 3.4: Transporter container of the gas cell (left) and home made cylindrical electromagnet to store the hyperpolarized ^{3}He in MRI-lab of the MPI-P (right). Left; The walls of the container have permanent magnets for field generation and shielded from external fields by a double layer of μ-metal. Right; the coil produces $25G$ with a current of $2A$. 2D axisymmetric FEM calculation of the flux lines inside this coil the gray scale intensities denotes the magnetic flux density, which is optimized for homogeneity and a maximal access to the center. Therefore the equally spaced coils had to have 229 windings at the ends while 158 were sufficient for the three in the center.

The polarization of the gas will only survive when the cell always stays inside an homogeneous magnetic field. As a consequence, special containers had to be designed for the transportation of these cells. They contain permanent magnets for field generation and shielded from external fields by a double layer of μ-metal [Gros00]. The relaxation time of the gas inside such boxes is longer than 100 hours. With such a box the gas can easily transported from the central ^{3}He production facility in the Institut für Physik to the Max Planck-Institut für Polymerforschung (MPI-P). Once in the MPI-P, the glass cell is stored inside a home made electromagnet of $25G$ shown in Fig.3.4.

3.2 Magnet and Spectrometer

All measurements were performed in a horizontal magnet of $4.72T$ with a $20cm$ bore[1]. Shielded gradients (Bruker, Rheinstetten) with strengths up to $300mT/m$ with a internal diameter of ca. $50mm$ were driven by DC-amplifiers (Copley Controls Corp.). A double resonant birdcage coil (Bruker) with an inner diameter of $26.5mm$ was used to excite ^{129}Xe and ^{3}He at Larmor-frequencies of $55.59MHz$ and $153.096MHz$, respectively. The gradients and the r.f. pulse were controlled from a Maran DRX console (Resonant Instruments) which runs under a Matlab (Mathworks Inc.) home made environment.

The gradients were calibrated imaging a sample with a known size at different gradient strengths. Then a comparison of the FOV with the sample size gives a relation between console parameters and gradient strength by means of Eq.2.52 and Eq.2.54 modified as

$$G_{read} = \frac{SW}{\gamma FOV_{read}} \quad \text{and} \quad G_{phase} = \frac{SI/2}{2\tau\gamma FOV_{phase}} \tag{3.1}$$

where τ is the time during which the phase gradient is applied, SI the number of acquired points and SW is the spectral width, equal to $1/DW$, where DW is the time between 2 acquisition points.

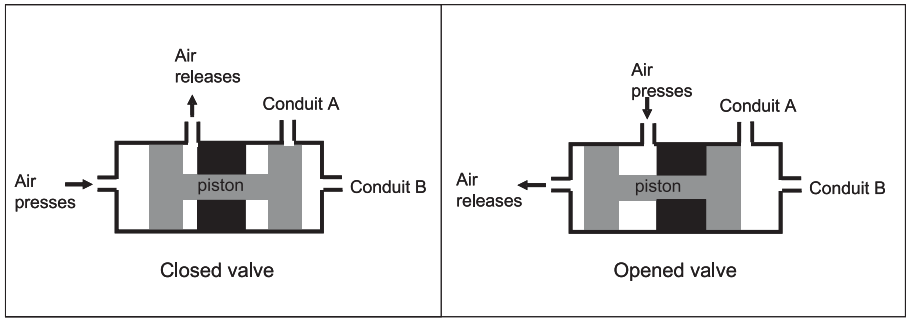

Figure 3.5: Valve used to block the way of the gas. Left: closed valve, the way of the gas for going from conduit A to conduit B is blocked by a piston, which is pushed by pressing air from left and releasing to the top. Right, opened valve: the conduits A and B are connected because the piston has been pulled pressing air from the top and releasing to the left.

3.3 Gas Mixer

3.3.1 Pneumatic Pistons and Magnetic Valves

A set of pneumatic pistons and magnetic valves were combined to even operate in the strong magnetic field of the superconducting NMR-magnet. Therefore, commercially available piston valves (Festo) had to be modified and tested. Firstly all magnetic parts were replaced in the piston valves by non magnetic ones, so that they could be mounted close to the NMR coil. The air flow which closes and opens the piston (see Fig.3.5) was controlled by a second set of magnetic valves outside the strong field of the superconducting magnet.

These magnetic valves are controlled by switching $24V$ which can be controlled manually or automated via the spectrometer. In this way valve operations can be included in the NMR pulse-programs, which made the measurements very fast, safe and reliable.

3.3.2 Automatized Gas Mixer

In order to prepare gas mixtures in a controlled way a dedicated setup for the gas handling had to be designed which is schematically presented in Fig.3.6 [Acos06] [Zaen07]. A sample tube of volume V filled with laser polarized (LP) gas was connected to the gas handling system, which is already positioned inside the NMR magnet. For ^{3}He measurements the sample tube was pre-evacuated and filled directly from

[1]Except images of Fig.6.15

the transport cell. Xenon filled bottles were pre-evacuated after a 10*min* accumulation of solid hyperpolarized xenon and then connected to the gas handling system; the bottle was left to reach ambient temperature for a period of approximately 15*min* under the presence of air flow.

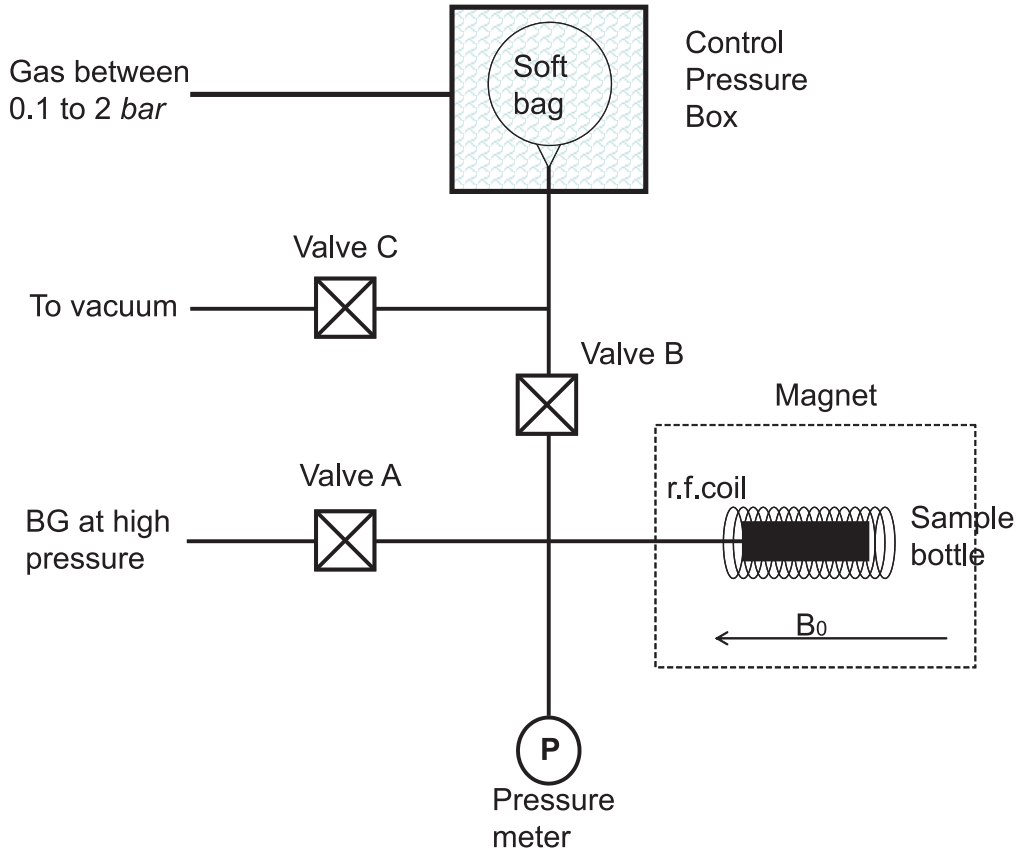

Figure 3.6: Sketch representing the pneumatic valve configuration used for preparing the different gas mixtures. A, B and C are pneumatic valves that can be controlled from the spectrometer console or manually. See text for details of their operation.

In order to minimize the length of the connection lines the pneumatic valves are located in the bore of the magnet in direct vicinity to the sample tube inside the r.f coil. To complete the setup a non magnetic pressure sensor (Sensortechnics GmbH, Puchheim Germany, PCB Series) was used to monitor the whole procedure. This sensor was also placed in the bore of the magnet and has an accuracy of 1*mbar*.

Valves B and C are opened in order to evacuate the transmission line to values in the order of $10^{-6}bar$. Once B and C are closed, the sample tube is opened to let the LP-gas expand into the transmission line. Valve B is then opened during a time t_B to release the exceeding pressure to a large soft bag inside a box (see Fig.3.7) at

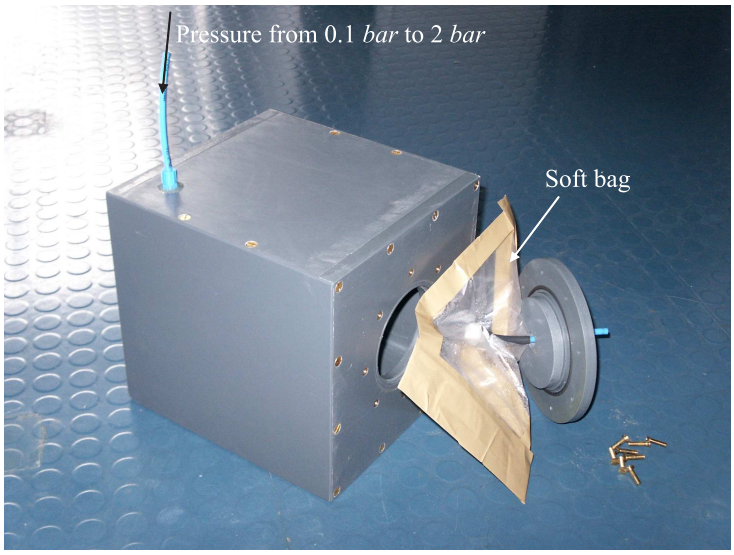

Figure 3.7: Box to controll the pressure inside the sample during the measurement, depicted in Fig.3.6. The soft bag is introduced in the box and connected to the gas handling system. The blue tube on the top of the box is connected to a N_2 gas source with regulable pressure when pressures $> 1bar$ are needed. For pressures below $1bar$ was attached a vacuum pump, with a pressure controll, was attached.

chosen pressure between 0.1 and 2 *bar*, thus establishing the pressure, p_A, of LP-gas in the sample tube. Usually, the ambient pressure is used as a reference pressure for the experiments. Closing B and opening C for a period of t_C permits the evacuation of the soft bag. The buffer gas is then pressed into the sample inside the r.f. coil by opening valve A for a short period of time, t_A. Prior to the equilibration with p_A an experimentally determined waiting time of ca. $6s$ is introduced to assure equilibrium in the gas mixture. At this point it is worth to note that mixing of gases is not due to diffusion processes as this would involve very long waiting times. The pressure of the buffer gas reservoir was typically set to 3 times p_A, in this way a turbulent inflow is generated which produces a complete mixture of both gases. The stabilization of the pressure sensor oscillated in 3–4 *s*, and the diffusion coefficient was measured repeatedly for a single inflow with a waiting time up to $10min$ with no apparent change within the experimental error.

3.4 Resolution Phantoms

In order to study the diffusion of a gas in different restrictions cavity shapes and sizes, two phantoms were built.

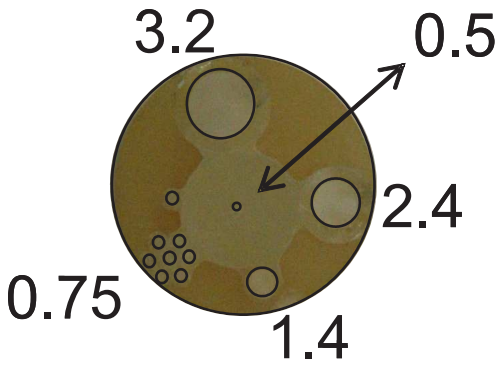

Figure 3.8: Set of cylinders of parallel capillaries whose long axis is set parallel to the B_0 direction (z). The cavity diameter sizes are depicted in the image in *mm*. The diameter of the capillaries are $(0.5, 0.75, 1.4, 2.4, 3.2)mm$

One phantom consists of a distribution of long capillaries, see Fig.3.8. Single capillaries of diameter $(0.5, 0.75, 1.4, 2.4, 3.2)mm$ were placed well apart in order to assure defined spatial resolution, while a group of capillaries with diameter $0.75mm$ are grouped for purposes not relevant for this work. All capillaries were sealed in one end and placed inside a rubber tube of $6.4mm$ radius. The space between the external part of the capillaries and the rubber tube was filled with epoxy and left to dry. After the rubber tube is removed, the set of capillaries was cut to a length of $40mm$ and placed inside a glass tube of $6.5mm$ radius and $150mm$ length.

This phantom, however, offers different restrictions regimes inside the same cavity. For a more ideal case, linear restrictions were needed. This was achieved with the phantom of Fig.3.9. This phantom consist of a set of parallel glass walls separated by distances of $(0.5, 0.75, 1, 2, 3, 4)mm$. The construction procedure was similar to the previous phantom.

In both cases, the connexion between phantom and gas handling system was done with a tube as small as experimental safely possible to avoid the gas diffusing between the phantom and the gas handling system. Especially care was put in the construction to avoid the glue, which stick the glass parts inside the phantoms (cylinders or glass walls), to be in contact with the LP-gases.

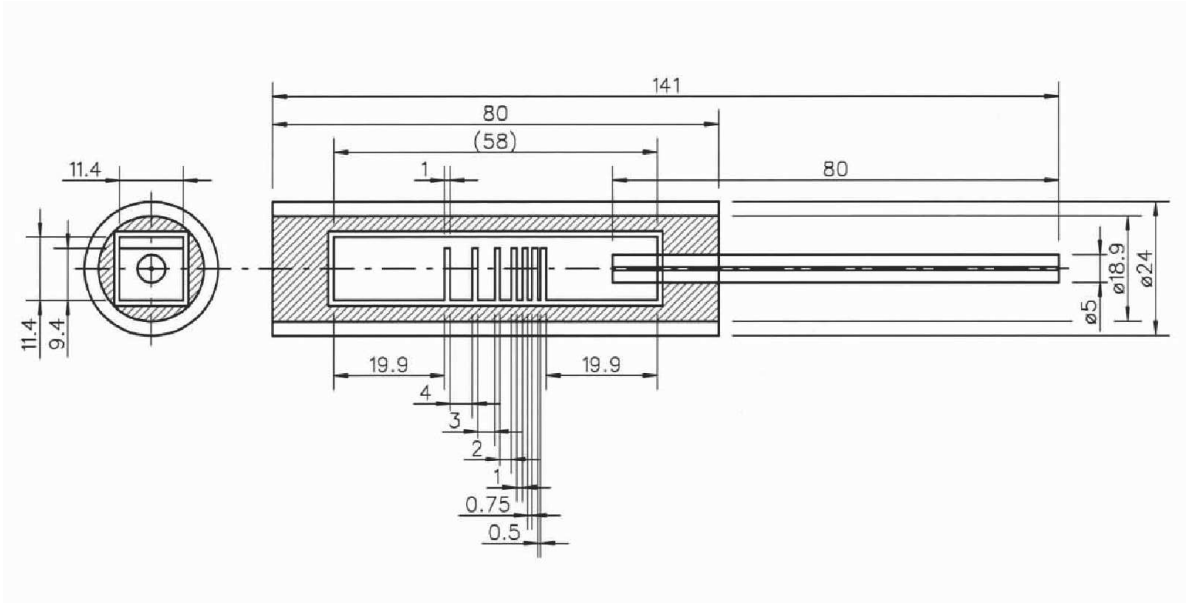

Figure 3.9: Sketch of the phantom, it consists of a set of parallel glass walls perpendicular to the B_0 direction (z). The distances separating the walls are (0.5, 0.75, 1, 2, 3, 4) *mm*. The thick of the separators are 1*mm*. Distances in the sketch are given in *mm*.

Chapter 4

Gas selfdiffusion measurements by NMR

Since Hahn published "Spin Echoes" [Hahn50], the influence of field inhomogeneities on the damping of nuclear spin echoes was known, which arises not only from relaxation effects but also from molecular displacements. 15 years later, Stejskal and Tanner [Stej65] developed an improved method to measure the Brownian motion by NMR. However, this motion is not necessarily related to the molecular motion, but to the spin of this molecule.

The new development of laser polarized methods has achieved polarizations close to the unity, 64% for ^{129}Xe [Ruse06] and 91% for ^{3}He [Wolf04]. These high polarization open the possibility to study new physical phenomena of laser polarized gases, e.g. dipolar coupling in ^{3}He gas at room temperature [Zaen07]. The hydrodynamic equations of a diluted spin polarized gas predict unusual effects like coupling between diffusion and heat conduction. As described in [Lhui82b] "*it may be hoped that these effects will be observed, either in* ^{3}*He or in* ^{1}*H*" . This, in principle, can be used to obtain information on thermal process from NMR measurements .

Therefore, in this chapter a detailed study of the gas diffusion coefficient, D, will be carried out in ^{3}He and ^{129}Xe. The classical theory will be presented following the ideal gas concept. Since D is measured by NMR methods, an explanation will follow with special interest in the magnetic properties and possible influence on the diffusion in hyperpolarized gases. This is important because in the following chapters D will be measured at different polarizations and in different gas mixtures.

4.1 Theory of gas self-diffusion coefficient

The diffusion coefficient, D, is a transport parameter already introduced in section 2.6 when the diffusion principles were presented as a probability distribution of particles in space. In this chapter a detailed theoretical description will be summarized in order to predict D. For that purpose, a particle spreading have to be considered to start off; it will cover a distance in a given time with a chaotic direction and path probability described in Eq.2.60. Thus, the diffusing particle will cover a closed surface of possible positions after a time. The diffusion coefficient will have the dimension of square meter per second.

In order to describe it in a mathematical way the first important point is the velocity propagation of particles in a gas. For that description the simplest theory is the so-called kinetic theory of gases, which assumes three basic points [Atk84]:

- The gas consists of particles of equal mass in ceaseless Brownian motion.
- The size of the particle is negligible, in the sense that their diameters are much smaller than the average distance traveled between collisions.
- The particles do not interact, except when they are in contact undergoing perfect elastic collisions.

Following this points, it can be concluded that the velocity of a gas component, whether an atom or a molecule, will span a wide range and the collisions continually redistribute the velocities among the particles. The fraction of particles with velocities between $\mathbf{v}$ and $\mathbf{v}+d\mathbf{v}$ is given by $f(\mathbf{v})d\mathbf{v}$ where

$$f(|\mathbf{v}|) = 4\pi \left(\frac{M}{2\pi RT}\right)^{3/2} \mathbf{v}^2 e^{-\frac{M}{2RT}\mathbf{v}^2} \tag{4.1}$$

and R is the gas constant, T the absolute temperature and M the molecular mass of the particle. Equation 4.1 is the Maxwell-Boltzmann velocity distribution and is represented in Fig.4.1 for Xe and He gases at standard conditions.

As it was mentioned, this speed distribution is given by collisions among the particles. The collision will be defined as if the particles were rigid spheres, i.e. there will be a collision whenever two particles are closer than their diameter d. The number of collisions made by one particle in a volume V with N particles divided by unit time will be given by the expression

$$w = \sigma v_r c \tag{4.2}$$

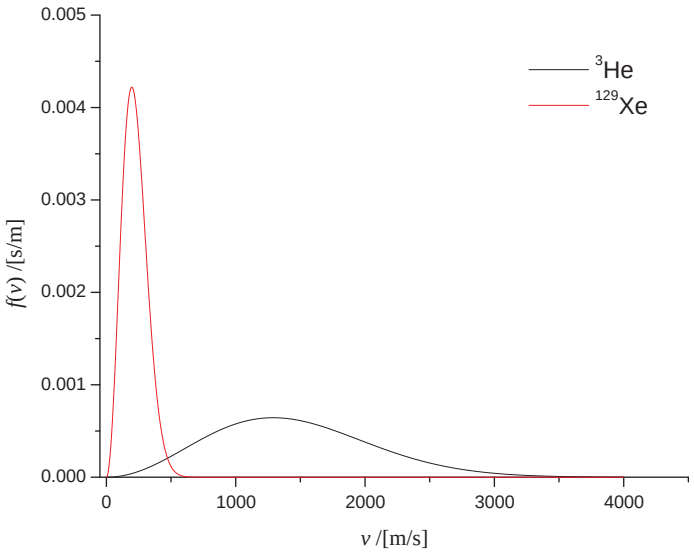

Figure 4.1: Speeds distribution of Maxwell-Boltzmann for ^{3}He and ^{129}Xe at standard conditions ($T = 25°C$ and $p = 1bar$).

where c is the concentration N/V, σ is the collision cross section of the particles as described in [Atk84] and v_r is related to the averaged velocity of the ensemble $\bar{v}$ as

$$v_r = \sqrt{2}\bar{v} = \sqrt{\frac{16RT}{\pi M}}. \tag{4.3}$$

For instance, one ^{3}He atom at $1bar$ and $300K$ will collide approximately $w \approx 2 \cdot 10^7$ times during one second considering the atom as a rigid sphere.

Once the velocity is known, the path λ traveled by the particle between collisions will be given by the following equation

$$\lambda = \frac{\bar{v}}{w} = \frac{k_B T}{\sqrt{2}\sigma p} \tag{4.4}$$

where the concentration c is substituted in the law for ideal gases $pV = Nk_BT$ with a pressure p.

In the case of one dimensional diffusion –lets say x-direction– a particle from a point with concentration $c(0)$ will cover on average a distance λ without colliding with other particles and will arrive at a point with concentration $c(\lambda)$, which can be described by a Taylor expansion of first order as

$$c(\lambda) \approx c(0) + \lambda \left(\frac{dc}{dx}\right)_0 . \tag{4.5}$$

In the case of a particle diffusion in the contrary direction, the concentration in $-\lambda$ will be given by

$$c(-\lambda) \approx c(0) - \lambda \left(\frac{dc}{dx}\right)_0 . \tag{4.6}$$

Consider now a plane perpendicular to the x-axis at $x = \lambda$ that is passed by a number of $\tilde{N}$ diffusing particles. The number of crossing particles will be proportional to the concentration c, to the surface area A of the plane, to the time Δt that the particles take to achieve the plane and to the velocity component in the x-direction v_x. However, to take the presence of a range of velocities in the sample into account, the result has to be summed over all possible ranges of v_x weighted by the probability distribution of velocities as Eq.4.1 for the x-direction

$$f(v_x) = \sqrt{\frac{M}{2\pi RT}} e^{-\frac{M}{2RT}v_x^2} \tag{4.7}$$

giving a total number of particles crossing the plane [Atk84]

$$\tilde{N}(\lambda) = cA\Delta t \int_0^\infty v_x f(v_x) dx = \frac{1}{4} A\Delta t c(\lambda)\bar{v}. \tag{4.8}$$

The flow of particles crossing the plane, i.e. the number of particles which cross the plane per unit area per unit time, will be given by

$$J_+ = \frac{\tilde{N}(\lambda)}{A\Delta t} = \frac{1}{4} c(\lambda)\bar{v} \tag{4.9}$$

in the case of the particles that diffuse in the positive direction of x. In the case of those particles diffusing in the negative direction of x, the flow will be

$$J_- = \frac{\tilde{N}(-\lambda)}{A\Delta t} = -\frac{1}{4} c(-\lambda)\bar{v} \tag{4.10}$$

and the net flow J will be the difference between the particles flowing to the positive direction and those flowing to the negative direction

$$J = J_+ - J_- = \frac{1}{2}\lambda\bar{v}\left(\frac{dc}{dx}\right)_0 \tag{4.11}$$

If an extrapolation to a 3-dimensional spread of particles is done and we compare

it with Eq.2.55, then we obtain a description of D as follows

$$D = \frac{1}{3}\lambda\bar{v} = \frac{1}{3}\frac{k_B T}{\sigma p}\sqrt{\frac{4RT}{\pi M}} \tag{4.12}$$

where the factor 2/3 is due to the fact that a diffusing particle still has a possibility of collision before or after traveling a distance λ [Atk84].

Although with only three assumptions a good determination of D has been derived, the kinetic theory of gases is still a rough approximation to the diffusion coefficient. A more complete theory has to take into account more detailed collisions terms. This task was done by Chapman [Cha70] and Enskog [Ens22], known as Chapman-Enskog theory. Several books deal with the subject [Cus03] [Tab91], but the most cited and complete is the one of Hirschfelder *et al.* [Hirs65].

An approximation to a more realistic collisions parameter will introduce more terms instead of σ in Eq.4.12. Following the description of D done by Hirschfelder *et al.* [1]

$$[D]_1 = 2.628 \cdot 10^{-7}\frac{\sqrt{T^3/M}}{p\sigma^2\Omega^{(1,1)*}(T^*)} \tag{4.13}$$

given in m^2/s where P is the pressure in atm, T in Kelvin and the collision parameter σ is completed with $\Omega^{(1,1)*}(T^*)$, which is a collision integral and depends on $T^* = kT/\varepsilon$, where ε is a parameter of the potential function that depends on the particle, as well as σ given in angstroms (1 Å = $10^{-10}m$). The subscript 1 in Eq.4.13 denotes the first approximation of the Champan-Enskog theory. Other approximations, like for example the influence of gas concentration and restriction, will be treated in the next chapter.

D	^{3}He	^{129}Xe
Eq.4.13	$1.837 \cdot 10^{-4} m^2/s$	$5.523 \cdot 10^{-6} m^2/s$
NMR	$1.8 \cdot 10^{-4} m^2/s$	$5.7 \cdot 10^{-6} m^2/s$

Table 4.1: Theoretical and NMR measured self diffusion coefficient for ^{3}He and ^{129}Xe at the pressure of 1 bar and temperature of 21°C. The experimental values are from Tab. 5.2 and Tab. 5.1 and experimental errors are less than 5%.

[1] see page 539 on [Hirs65]

4.1.1 Polarization influence on spin diffusion

The theory described is related to the movement of completely identical particles, where collisions were not affected by magnetic properties. As already explained in section 2.6, the parameter that describes the diffusion coefficient in NMR is the signal decay due to the influence of magnetic field gradients that dephase the coherence of the spins. Thus, the information of the diffusion is deduced from spin movement when it dephases; a process that not necessarily has to happen due to the movement of the particle, it can also happen when the spin state is transfered from one atom to other. This is important since other interactions could influence the measurement of the diffusion coefficient. This could suggest the idea that there can be a difference between particle and spin diffusion, i.e. the particles could not to be considered identical any more since magnetic properties make a distinction. As we can see, in order to measure D in a rigorous way, spin diffusion effects should be excluded.

In section 3.1, it was already mentioned that the polarization achieved in ^{3}He can be close to 90% and polarization of ^{129}Xe is getting close to this level [Ruse06] [Ruth99], even though in this work only a polarization up to 8% has been used, which is enough for the purpose of the work. These two gases have extended use in NMR due to their high polarization level and hence to the high signal to noise ratio achieved. The capacity of a gas to fill the entire container makes them a perfect tool in NMR to obtain images [Rizi05] and other information –by means of diffusion measurements for example– of porous material cavities [Tast05] and especially the lung [Eber96] [Conr06]. Due to the porosity, the gas is in contact with a big surface, and then T_1 and T_2 times are affected as explained in section 2.3. The T_1 decay, in the case of laser polarized gases, leads to a drawback because of the loss of polarization. Therefore, during an NMR experiment the polarization changes and consequently all factors that are influenced by diffusion can be affected.

In order to study spin diffusion, a method to include the indistinguishability of the nuclei when a collision occurs has to be adopted. The atoms that collide will have an "average" cross section of two; one with the scattering amplitude for distinguishable particles [Lhui82a]:

$$|f(\theta)|^2, \tag{4.14}$$

and one with the scattering amplitude for identical particles:

$$\frac{1}{2}|f(\theta) - f(\pi - \theta)|^2 \tag{4.15}$$

in the case of Fermions, with weights given by the probability of the nuclear spin to

be in the same state, i.e. the polarization. Consequently, there will be a dependence on the averaged nuclear polarization of the gas.

In fact, Emerly [Emer63] pointed out that there were discrepancies between NMR measurement of diffusion coefficient and theoretical estimations. Other authors developed different aspects of this effect; the dependence on initial spin polarization and flip angle [Legg68], the necessity of a drastically modification of the theory for low temperatures and high magnetic field [Legg70], the logarithmic temperature dependence of D [Miya83], differences in the transverse and longitudinal spin diffusion collision time in polarized Fermi gases [Jeon89] [Mull83]. Jeon at al. [Jeon86] show a theoretical dependence of spin diffusion upon temperature for different polarization [2]. It is observed that the spin diffusion dependence on polarization, decreases with increasing temperature. A recommended review is the work of Lhuillier and Laloë [Lhui82a] [Lhui82b].

Even though most of these citations deal with ^{3}He at low temperatures, the work of Lhuillier and Laloë treat the effects of polarized gas in a more general way. Especially in reference [Lhui82b] is described the problem of spin diffusion in polarized gases. In order to study the evolution of an ensemble of spins in a gas, the Boltzmann transport equation is considered. It describes the distribution of particles in a fluid in non-equilibrium statistical mechanics by giving the time evolution function $f(\mathbf{r},\mathbf{p},t)$ of the distribution (properly a density) in phase space. Here $\mathbf{r}$ and $\mathbf{p}$ are position and momentum, respectively. A first approximation to the solution concludes that the spin current terms are described by

$$\mathbf{J}(M_x) = -\frac{D_0}{1+\mu^2P^2}\left[\nabla M_x - \mu P \nabla M_y\right] \tag{4.16}$$

$$\mathbf{J}(M_y) = -\frac{D_0}{1+\mu^2P^2}\left[\nabla M_y + \mu P \nabla M_x\right] \tag{4.17}$$

$$\mathbf{J}(M_z) = -D_0 \nabla M_z \tag{4.18}$$

for the case of Fermions, with P as the polarization, μ as a coefficient of the collision integrals and D_0 as the classical diffusion coefficient, both defined in [Lhui82b]. It is observed that for the case of low polarization, the spin and the particle or classical diffusion coefficient takes the same value, as follows

[2] See Fig. 3 on [Jeon86].

$$\mathbf{J}(M_x) = -D_0 \nabla M_x \tag{4.19}$$
$$\mathbf{J}(M_y) = -D_0 \nabla M_y \tag{4.20}$$
$$\mathbf{J}(M_z) = -D_0 \nabla M_z \tag{4.21}$$

In the general case, however , the authors claim that[3] "$\cdots$ *there are in fact some corrections to the value of the spin diffusion coefficient, which depend on quantum exchange effects for indistinguishable particles. Physically, if these effects can not change* $\mathbf{J}(M_i)$*, they can do it indirectly by modifying the velocity distribution of spin up or down atoms separately, so that the subsequent collisions between atoms with opposite spins can eventually be affected.*"

A second approximation of the solution of the Boltzmann equation takes the coupling with heat conduction into account, showing a dependence of the spin current on the polarization. Due to the large polarization in the present work ($M_z >> M_x, M_y$) only $\mathbf{J}(M_z)$ is considered [Lhui82b]

$$\mathbf{J}(M_z) = \frac{-D_0}{1 - \frac{C_1 + C_2 P^2}{C_3 + C_4 P^2}} \left(\nabla M_z + P(1-P^2)\alpha(P^2) \nabla \log(T) \right) \tag{4.22}$$

where C_i are linear combinations of integral collisions which depend on cross sections as well as $\alpha(P^2)$. As an homogeneous distribution of temperature through the sample is assumed, the temperature gradient term can be neglected leading to

$$\mathbf{J}(M_z) = \frac{-D_0 \nabla M_z}{1 - \frac{C_1 + C_2 P^2}{C_3 + C_4 P^2}} \, . \tag{4.23}$$

In the case of the present work, in the next chapter several measurements of diffusion coefficient at different polarization level will be presented. In order to study the influence of spin diffusion in such measurements, similar experimental conditions have to be carried out in the current chapter.

4.2 $D_{\mathbf{Xe}}$ vs. Polarization

The first experiment presented is the measured D of ^{129}Xe at different polarization levels. In order to obtain a detailed measurement of D in the region of low polarization, several measurements were done and added. Experimental parameters of the

[3] See page 228 on [Lhui82b].

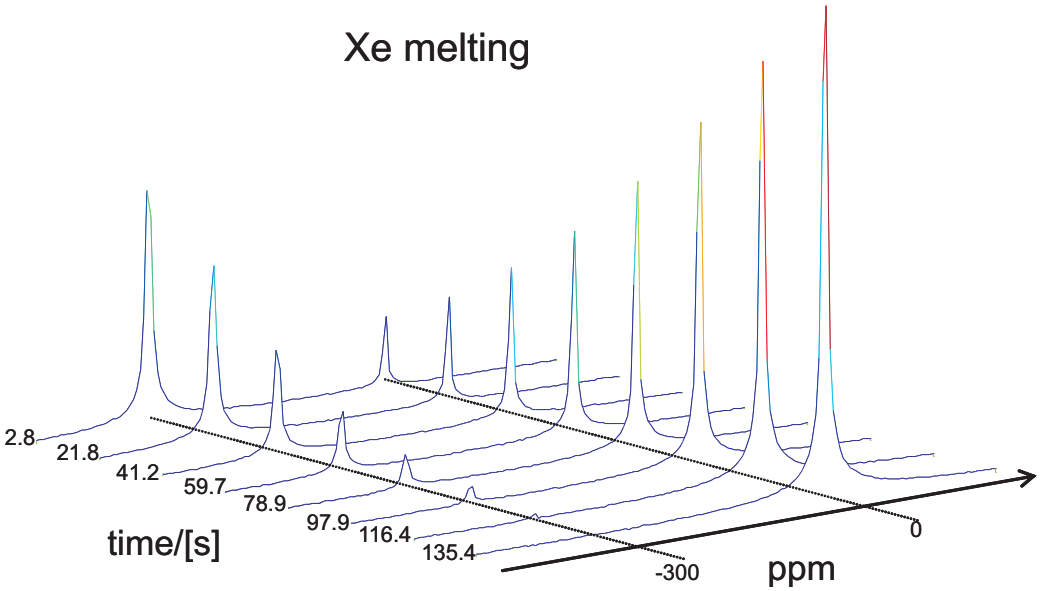

Figure 4.2: Xenon spectra during melting process. It begins in solid state with a ppm of -300 and in a little bit more than 2 minutes the Xe within the coil is converted in gas achieving 0 ppm.

polarization procedure are described in section 2.7.1 and 3.1.1. The maximal polarization achieved was around 8% .The polarized Xe was collected in a cold finger and then introduced into the magnet until it reaches room temperature.

Solid Xe produces a signal located at -300 ppm and its change of phase can be monitored as shown in Fig.4.2. In circa 2 minutes the solid Xe collected in the cold finger is melted by an external continuous air flow at room temperature. Though Xe is in gaseous state, it has not yet thermally equilibrated to room temperature. The strong dependence of D on the temperature gives the possibility of monitoring sample temperature changes and to observe when the sample has equilibrated to room temperature. As shown in Fig.4.3, the D (measured at 0 ppm) decreases while Xe melts due to the increase of Xe in gaseous state, i.e. due to the increase of pressure. After 5 minutes, although Xe has completely melted, it has not reached the room temperature and D continues increasing until the temperature in the sample reaches the ambient one. After 15 minutes the sample is thermally equilibrated to room temperature; changes of D are within the error estimation and the sample can be considered in thermal equilibrium. Finally the gas is released to 1bar in order to measure D at a reference pressure.

After room temperature has been reached, the experiment begins measuring D at different polarization levels. Change of polarization was left to spin-lattice relaxation with T_1 as characteristic time (see Fig.4.4) and ,with less importance, to the demag-

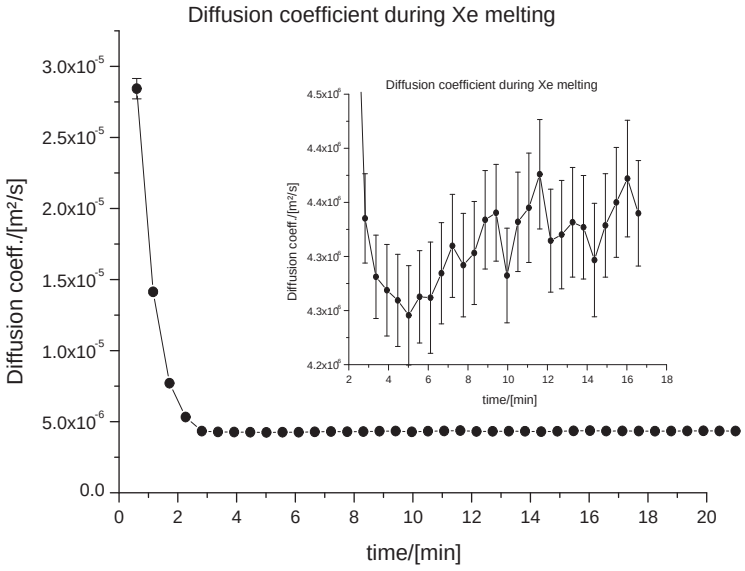

Figure 4.3: Change of the diffusion coefficient of Xe gas during melting. When Xe melts, the pressure increases inside the sample within the first 3 minutes. After that, the temperature increases, increasing slightly the diffusion coefficient. After 15 minutes, the sample has equilibrated to room temperature within the error.

netization due to the r.f. pulses of the diffusion coefficient sequence. Sample's polarization was determined comparing Boltzmann –or thermal– signal and laser polarized signal. For the determination of the sample's signal with Boltzmann spin distribution, circa 3000 FID were acquired and averaged out to obtain a thermal signal, when the laser polarized signal was completely used (after more than 10 times T_1). The thermal signal is then related to the polarization given by Eq.2.14. During the acquisition of the thermal signal, Xe was mixed with air in order to reduce T_1 and having more time to acquire and add the signal.

The diffusion coefficient was measured stepping linearly 10 times the gradient strength of the sequence of Fig.2.12 b) and fitting the signal decay to the Stejkal-Tanner equation (see Eq.2.65). A maximal b-value[4] of 6500 s/m^2 was used to dephase the spins and hence weight the signal by diffusion. The D measurement was done each 200 s; this time was chosen because it corresponds to that necessary for a Xe atom to diffuse a distance of the coil length, so the gas has time to distribute homogeneously within the coil and avoid local magnetization gradients.

[4] $b = \gamma^2 G^2 D[\delta^2(\Delta - \delta/3) + \varepsilon^3/30 - \delta\varepsilon^2/6]$ for parameters depicted in Fig.2.12

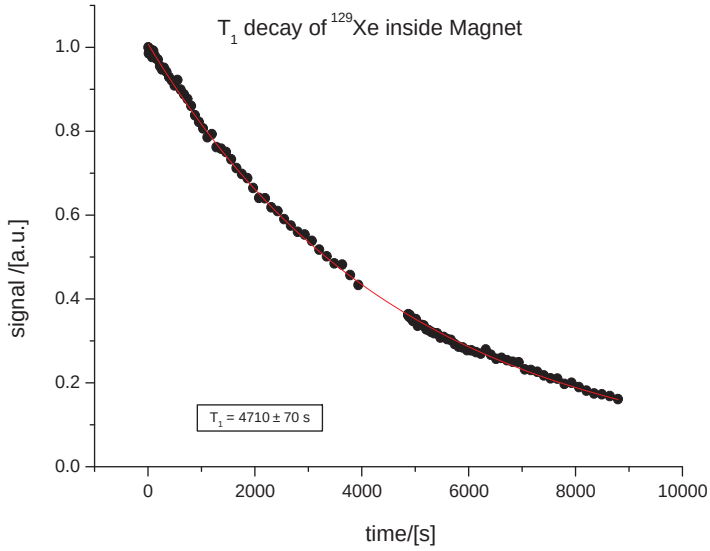

Figure 4.4: Measurement of hyperpolarized ^{129}Xe magnetization decay time T_1 inside the magnet: $T_1 = 4710 \pm 70s$.

Figure 4.5 presents the measurements of D as a function of polarization. For the present work, the values for the higher achievable polarization are most relevant, where a constant value is measured. In the low polarization regime, between 0.5% and 2%, the measured data shows a decrease up to 2.3% from the expected value. A possible explanation of this apparent decay, is the day/night laboratory temperature change what can influence the measurement. For example, a change of $2°C$ in temperature can lead for a change in the measured D of ca. 1%. Another factor that can influence also is the gradient overheating. After severals experiments, the gradient coil resistance can increase and reduce the gradient intensity, which produces a smaller spin dephase and hence leads to a smaller D. For example, a change in the gradient intensity of 1.5% produces a change in D of 3%. Even though, these points, shown for completeness, are within the error estimation and agree with the literature value [Hirs65] shown in Tab.4.1.

4.3 Measured D of ^{3}He vs. Polarization

The achievable polarization levels of ^{3}He gas are considerably larger than those of ^{129}Xe gas. Two different measurements will be presented to measure D with different depolarization methods. In the first one the depolarization is left to the spin lattice

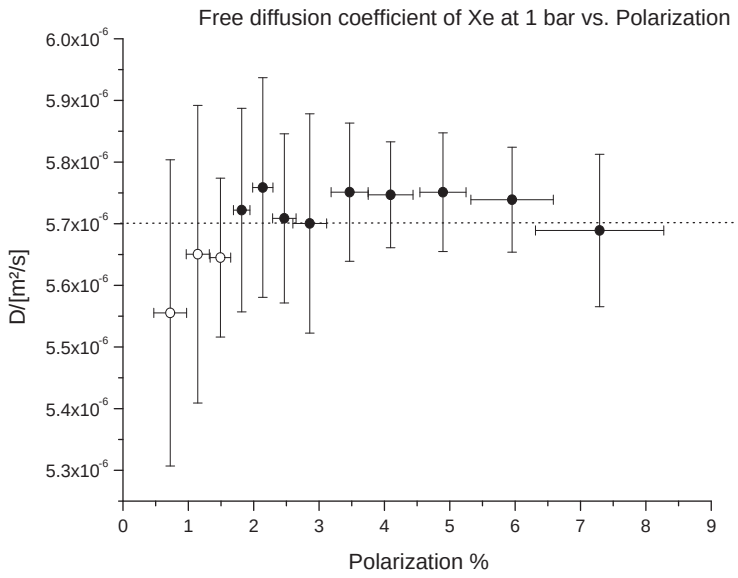

Figure 4.5: Average measurements of the diffusion coefficient, *D*, of Xe at 1 bar versus different polarization levels. The averaged *D* errors were weighted by its error at fitting with the Gaussian signal decay. The dotted line shows the experimental value from Tab. 5.2. Empty circles were measured during overnight experiments, which were prone to temperature changes and gradient overheating. Although these points are not significant because of the large experimental errors, they are shown for the sake of completeness.

decay and done at 1 bar, as in the Xe case. In the second method, *D* is measured at different collisions regimes. For that purpose measurements will be done at different pressures and then normalized to 1 bar. The measurements at different pressures require a fast depolarization method –large r.f. pulses could produce radiation damping– thus change of polarization will be achieved by admixture of laser polarized ^{3}He with thermal polarized ^{3}He.

4.3.1 $D_{\mathbf{He}}$ vs. Polarization at 1 bar

Unlike Xe, in the case of *D* of ^{3}He only 2 measurements were sufficient to obtain a reasonable good value for the low polarization zone; due to the larger γ, achievable polarization and abundance of the detected isotope. The sequence and sample were similar to those used for Xe. The ^{3}He was hyperpolarized at the institute of physics at the Mainz university [Heil96] [Schm04], by the method described in section 2.7.2

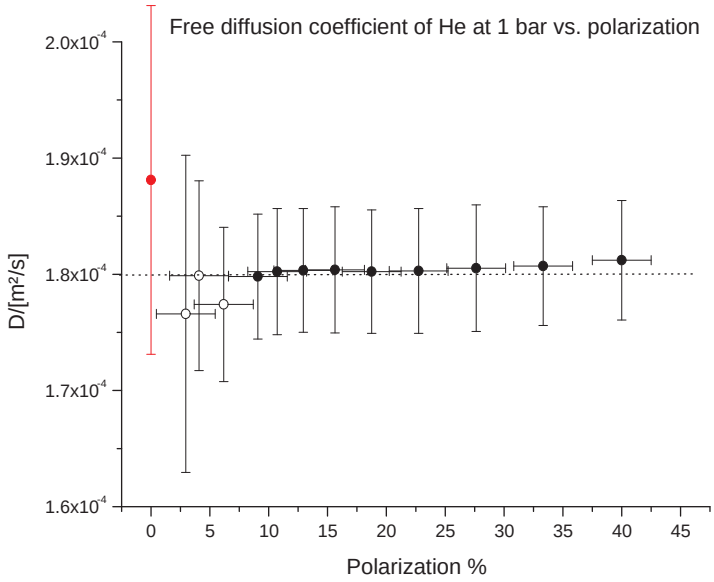

Figure 4.6: Average measurements of the diffusion coefficient, D, of He at 1 bar versus different polarization levels. The averaged D errors were weighted by its error at fitting with the Gaussian signal decay. The dotted line shows the experimental value from Tab. 5.1. Empty circles were measured during overnight experiments, which were prone to temperature changes and gradient overheating. Although these points are not significant because of the large experimental errors, they are shown for the sake of completeness. The red point is the measurement at thermal polarization as explained in section 4.3.3.

and 3.1.2.

The D was measured by stepping a bipolar gradient (see Fig.2.12 b)) with a maximal b-value of 500 s/m^2. However, in this case the polarization was measured by the institute of physics as described in [Heil97] [Schm04], and corrected by the T_1 decay influence due to the cell transport and storage (see section 3.1.2). A polarization higher than 50% was achieved in the polarizator. Polarization change during the D measurements was left to the spin-lattice relaxation and, to a small extent, to r.f. pulses of the sequence.

The D for different polarization levels for standard conditions of pressure and temperature is shown in Fig.4.6. As in the case of Xe, a strong deviation of the measured D from the literature value [Hirs65] (see Tab.4.1) was not observed. Only the points with less than 7% of polarization present a slight dispersion but well within the error estimation. This deviation could be originated due to the same factors explained

in the Xe case.

4.3.2 D_{He} vs. Polarization vs. Pressure

An important factor in the experimental determination of D is the pressure of the sample, as already explained for the behaviour of the diffusion coefficient in Fig.4.3. From Eq.4.12 the following equation can be obtained:

$$p \cdot D = \frac{1}{3}\frac{k_B T}{\sigma}\sqrt{\frac{4RT}{\pi M}}, \tag{4.24}$$

which will be used to normalize D to 1 *bar* when measurements at different pressures are carried out.

As it is known from the classical theory of gases, the pressure indicates the momentum interchange between components of a gas and the walls of its container and, as explained in Eq.4.4, the pressure is also proportional to the number of collisions made by one particle, w (see Eq.4.2). The aim of the pressure change is to create a scenario with different collision rates, and therefore different probabilities of interactions between spins. Another parameter that could be changed is the temperature, however, from the experimental point of view this is more complicated due to possible temperature gradients within the sample. This problem is avoided in the case of pressure changes.

The diffusion coefficient measurement at different pressures were conduced by means of the pressure box presented in section 3.3.2. Inside this box is an elastic bag, which is connected to the sample, so that this bag equilibrates to the pressure inside the box. The pressure of the box was varied between 0.1 *bar* to 1 *bar*, in increments of ca. 0.1 *bar*; this corresponds to a number of collisions $w(1bar) \approx 10^4$ to $w(0.1bar) \approx 10^3$ at room temperature in a typical sequence time of $1000\mu s$ (see Eq. 4.2). For a short time, ^{3}He–^{3}He molecules can be formed by dipolar couplings, which can lead to a spin state information loss and hence to a spin exchange [Wolf04]. The probability of this exchange is ca. 10^{-7} per time unit by averaging over the sum of the collisions frequencies [Torr63] [Mull90] at ambient pressure.

Only four representatives experiments, from 10, are presented for clarity in Fig.4.7. All others experiments show the same behaviour. In this figure $D \cdot p$ is plotted versus the polarization for different pressures and, for a better comparison, the diffusion coefficient is normalized to 1 *bar*. The D measurement procedure was the same as in the previous section. Nevertheless, in order to adjust the b-value to D, which changes inversely with the pressure, values from 1524 s/m^2 at 1 *bar* to 747 s/m^2 at

0.1 *bar* were taken changing the gradient intensity. A factor that increases the error is the smaller quantity of ^{3}He at decreased pressures resulting in weaker NMR signals. Again, the polarization was determined at the institute of physics at the Mainz university, as in section 4.3.1. The initial polarization was $67\% \pm 5\%$ in a cell with a T_1 of 91 hours. All measurements were done in less than 5 hours, which corresponds to a polarization difference of ca. 5% between first and last measurement, i.e. 1 *bar* and 0.1 *bar* respectively.

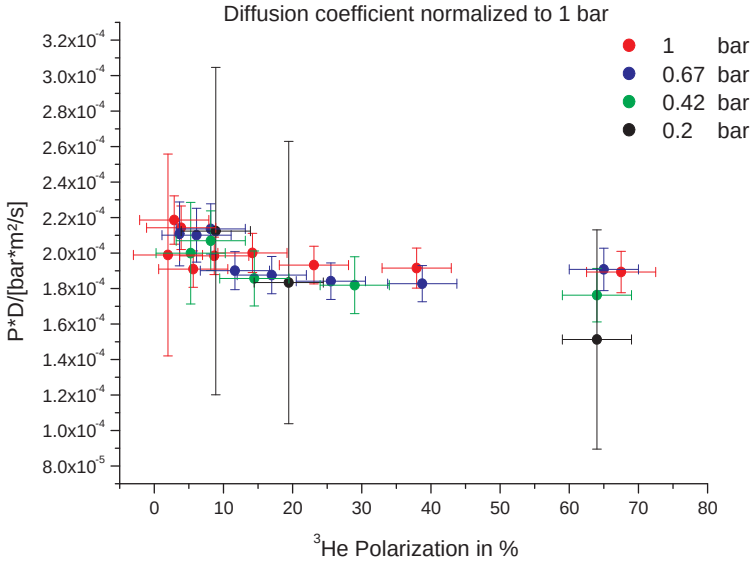

Figure 4.7: Diffusion coefficient measurements of ^{3}He at different pressures versus different polarization degrees. Measurements were normalized to 1 *bar*. Diffusion errors were weighted by its normalization factor and polarization error was 5%.

Unlike the first two measurements presented in this chapter (*D* of Xe and He at 1 *bar*), here the depolarization process of the spins is not only obtained by spin-lattice relaxation. For this experiment, the gas mixer of section 3.3 was used with thermally polarized ^{3}He at 3.1*bar* as a buffer gas. This allow faster experimental times, avoiding gradient overheating and permitting a better temperature stability, which are sources for experimental errors in longer experiments.

In Fig.4.7 it can be observed that for high polarization the corrected *D* is the same for all pressures and coincides with the values of Tab.4.1. For lower polarization levels a dispersion of the values is observed. Unlike in Fig.4.6 and Fig.4.5 there is no a clear increase or decrease of the values, which arises from the faster depolarization method.

Like in the last two cases, however, these deviations still lie inside the experimental error. Even with a difference of an order of magnitude in the number of collisions experienced by one particle, w, no deviation outside the error bars is observed.

4.3.3 D_{He} at thermal polarization at 1 bar

The last measurement presented in this chapter is the D of thermally polarized ^{3}He at $1bar$. In the case of pure ^{3}He, which magnetogyric ratio is close to that of protons, an NMR signal can be obtained even though the density of a gas is around thousand times smaller than in a liquid, but, of course, the signal to noise ratio is rather low. The thermal polarization of ^{3}He in a magnet of $4.7T$ will be of the order of water –ca. 20 per million– as described by Eq.2.15.

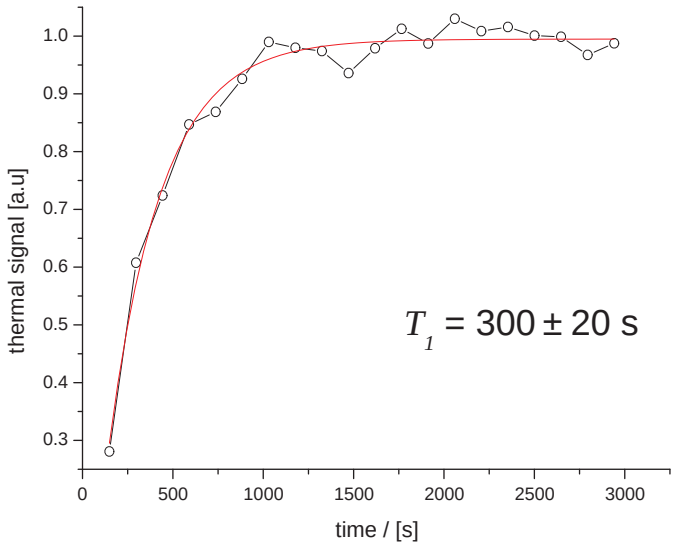

Figure 4.8: Recovery of ^{3}He normalized thermal signal versus time to measure T_1.

The sample for D measurements with hyperpolarized gas is optimized to have a long T_1 to store the large polarization of the gas[5]. This is a severe drawback in the case on thermal measurements. The poor signal to noise ratio needs several scans to add a suitable signal particularly when gradients are applied for diffusion coefficient measurements. A complete recovery, typically $5T_1$, of the magnetization after a

[5]The glass cell with the shortest T_1 was chosen to measure the D at thermal polarization, which is not the same cell used in the previous experiments.

$\pi/2$ pulse is necessary. A recovery measurement of the signal was done as shown in Fig.4.8. The sequence for signal recovery of thermally polarized ^{3}He was as follows: $\pi/2 - Acq - \tau$. The sequence was repeated with increasing τ. It was observed that after 1500s the signal was completely recovered.

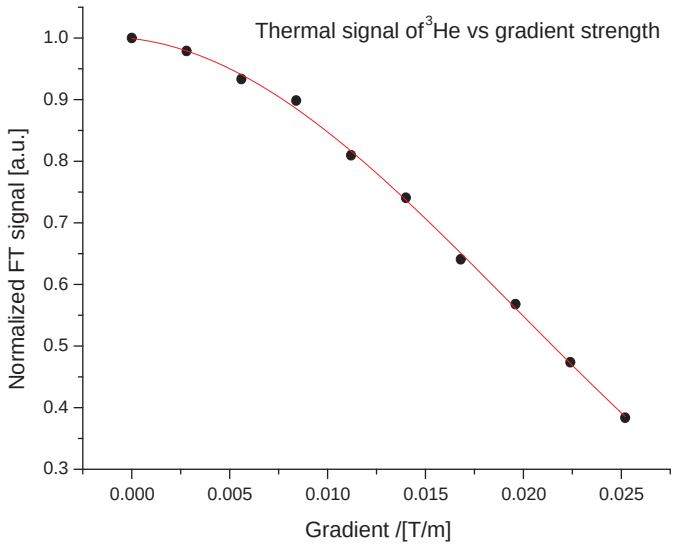

Figure 4.9: Diffusion coefficient of ^{3}He at 1 *bar* with thermal signal. Each point is an average over 31 measurements with a repeat time of 1500s. The fitted diffusion coefficient (red line) was $(1.95 \pm 0.15)10^{-4} m^2/s$ for a temperature of $(20 \pm 2)^\circ C$. The polarization was ca. $2 \cdot 10^{-6}$, given by a polarization field of $4.72T$.

With this data, the diffusion coefficient sequence was acquired 31 times. A b-value of $6095 s/m^2$ was used with the sequence described in Fig.2.12 b), a maximum gradient strength of $0.0286 T/m$ that was rased 10 times. The D was fitted at $(1.95 \pm 0.15)10^{-4} m^2/s$, value that agrees with Tab.4.1 and is shown in Fig.4.6 where is represented in red. This D could be easily plotted very close to the zero polarization without being incongruous with the other points of Fig.4.7. Because of the long time measurement, pressure and temperature oscillations and gradient overheating increased the error estimation. Even so, the measured diffusion coefficient error is less than 8%.

4.4 Conclusions

The kinetic theory of gases, based on three simple assumptions, already develops a very accurate prediction of the diffusion coefficient D. A more realistic theory has to take into account different factors involved in the collision of particles since the kinetic theory of gases only considers them as composed by rigid spheres. Adding this factors, Chapman [Cha70] and Enskog [Ens22] developed a more exact description of D in gases resulting in Eq.4.13.

Since the technique used in this work to measure D is NMR (described in section 2.6.3) magnetic properties which can influence this kind of measurement, will have to be considered. Emerly [Emer63] observed that the diffusion coefficient given by the Champman-Enskog theory was systematically smaller than experimental values given by NMR methods. After this, several discrepancies between spin diffusion and particle diffusion were investigated. In a complete review, Lhuillier and Laloë [Lhui82b] describe the importance of the polarization for spin diffusion by means of Eq.4.23, showing a dependence of the spin current on the polarization.

The large polarization achieved actually in ^{3}He and ^{129}Xe in a gaseous state at room temperature, makes a rigorous measurement of D versus polarization necessary. Moreover, since gases have a D four orders of magnitude higher than liquids, influence of spin diffusion in clinical gas MRI has special importance because the polarization changes during the MRI sequence –besides influences explained in section 2.3. *In vitro* samples, like those used in this chapter, allow for a more accurate measurement of D compared with clinical studies, which makes these measurement more sensible to polarization effects. Measurements were done at 1*bar* (or normalized to this pressure) in order to make them comparable to clinical conditions, though temperature was 15 degrees less than body temperature. Only pure gas was investigated, nevertheless, it is believed that if no effects are observed under such experimental conditions, they can hardly be expected in clinical experiments. As far as we know, no one has reported such measurements to investigate the influence of polarization on diffusion of gases in clinical conditions, neither *in vitro* nor *in vivo*.

Diffusion measurements of ^{129}Xe and ^{3}He at different polarization have been done and presented in Fig.4.5 and Fig.4.6 respectively. Polarization decay was produced by spin-lattice interaction, and with less influence to sequence r.f. pulses. In both gases, D agrees with theoretical values for high polarization values.

As pressure is proportional to the number of particle collisions, different pressures correspond to different collision rates and therefore different spin transition probabilities. The diffusion coefficient of ^{3}He was measured at different pressures and normal-

ized to 1*bar* (see Fig.4.7). For the depolarization, however, a mixture with thermal polarized ^{3}He gas was used. The result was the same as in the two previous experiments.

A difference between spin diffusion and particle diffusion was not observed under our experimental conditions. Since ^{3}He is more frequently used in MRI, this gas received more attention with a deeper research. The experiments done *in vitro*, which are more sensitive than an usual clinical MRI, do not show any divergence in *D*, so it can be conclude that spin diffusion, if it occurs under clinical conditions, has no observable effect in the particle diffusion measurements by NMR. The experiments at different pressures, after normalization, show also no deviation, what means that under more restricted movement conditions –such as capillaries, alveoli or buffer gas: as in experiments of chapter 5 and chapter 6– no spin diffusion effects can be expected.

The method used to depolarize ^{3}He by means of admixture with thermally polarized ^{3}He by means of gas admixture is reliable under different pressures and polarizations. These measurements verify the stability of the gas mixing system used in the next chapter.

Chapter 5

Gas admixture

From the very beginning of the application of laser-polarized (LP) noble gases to magnetic resonance imaging (MRI), diffusion measurements were envisioned as a tool for studying the microscopic structure of respiratory organs. Diffusion coefficients of gases at standard temperature and pressures are of the order of 10^{-4} to $10^{-5} m^2/s$, which are 4–5 orders of magnitude greater than in liquids. Although the distance diffused during a typical time interval of $1ms$ for the application of a gradient pulse is approximately $600mm$ for ^{3}He gas, the diffused distance will be reduced by the restrictions imposed by the dimension of the volume. The second condition that influences the diffusion coefficient of a LP gas is its interaction with other gases present in the imaged volume: N_2 and O_2 in biomedical applications. In this chapter the possibility of generating a highly controlled binary gas mixture at $1bar$ overall pressure is explored, which is a necessary condition for clinical imaging.

A detailed description of the theory of the precise determination of the molar fraction of ^{3}He and ^{129}Xe in admixture with different buffer gases is presented. The resulting protocol is applied for the measurement of the diffusion coefficient as a function of the molar fraction for three very different buffer gases, namely ^{4}He, N_2 and SF_6. The admixture of LP ^{3}He to these gases is very relevant; ^{4}He and SF_6 are very light and very dense gases, respectively. It has been shown that they can be used to provide opposite contrasts in MRI [Acos06b], while N_2 is present in most biological studies and, since it has a similar molecular mass as oxygen, is a good approximation to a ^{3}He mixture with air, ideal for lung research. The inverse situation of a dense LP gas such as ^{129}Xe upon a mixture with these gases was also studied.

Simulations were performed of direct atomistic molecular dynamics on the binary gas mixtures in order to obtain a realistic theoretical description of the diffusion properties of this system at the actual temperature and pressure in the corresponding

experiments. Using interaction potentials of Lennard-Jones type, the molecular dynamics simulations incorporate the mass and size of the individual particles as well as their mutual attraction and repulsion due to the interactions of the electronic clouds of the atoms.

5.1 Theory of gas admixture diffusion coefficient

The diffusion coefficient, D, seen until now is the one related to one particle diffusing without restrictions in an atmosphere of more identical particles. In this chapter, binary mixtures of gases will be used and hence another diffusion coefficient has to be considered. This corresponds to the NMR sensitive isotope; one gas mixture component and not to the gas as a whole. The more important characteristic is whether the gas component of interest is restricted via heavier buffer gases (BG) or its movement is less restricted via lighter BG.

As a start, D of the gas as a whole, the so-called binary diffusion coefficient $D_{1,2}$, will be considered. From the known Chapman-Esnkog theory of the previous chapter, Hirschfelder at al.[Hirs65] continued developing D. The authors present in this book a first approximation to the binary diffusion coefficient as follows:

$$[D_{1,2}]_1 = 2.628 \cdot 10^{-7} \frac{\sqrt{T^3 \mu}}{p \sigma_{1,2}^2 \Omega_{1,2}^{(1,1)*}(T_{1,2}^*)} \tag{5.1}$$

given in m^2/s with p in bar, T in kelvin, $\mu = \frac{m_1+m_2}{2m_1m_2}$ is the reduced mass and $\Omega_{1,2}^{(1,1)*}(T_{1,2}^*)$ is a collision integral term that depends on $T_{1,2}^*$, which is the reduced temperature equal to $k_B T/\varepsilon_{1,2}$, being $\varepsilon_{1,2} = \sqrt{\varepsilon_1 \varepsilon_2}$ a collision characteristic term, and the collision parameter as

$$\sigma_{1,2} = (\sigma_1 + \sigma_2)/2 \tag{5.2}$$

with collision diameter in angstroms (1 Å = $10^{-10}m$). Subindex 1 and 2 makes reference to spice-1 and to spice-2 respectively[1].

Following this equation, the value of $[D_{Xe,He}]_1$ for a Xenon-Helium gas mixture at $294.15K$ and $1bar$ is $6.1437 \cdot 10^{-5} m^2/s$, which is a value in between those presented in Tab. 4.1. However, different concentrations, can alter the movement of the particles and hence the diffusion, a fact that is not explicity considered in Eq.5.1.

[1] See page 539 on [Hirs65]

5.1.1 Concentration dependence of diffusion coefficient

Gas mixture concentration is taken into account in higher approximations of the Chapman-Enskog theory (approximations done by Kihara [Kiha53] lead to a similar result) applied to Eq.5.1 as follows for the k^{th}-approximation

$$[D_{1,2}]_k = [D_{1,2}]_1 f_D^{(k)}. \tag{5.3}$$

In a second approximation, the function $f_D^{(2)}$ depends on molecular weights, mole fractions, temperature and viscosities of the two components as follows:

$$f_D^{(2)} = \frac{1}{1 - W\frac{(6C_{1,2}^* - 5)^2}{60(X_\lambda + Y_\lambda)}} \tag{5.4}$$

where W, $C_{1,2}^*$, X_λ and Y_λ depend on concentration, molecular masses, integral collisions and thermal conductivity[2]. The dependence of $[D_{1,2}]_2$ on the composition of the mixture of gases is only slight since $f_D^{(2)}$ differs only slightly from the unity. For example, in a gas mixture of Xenon and Helium at $294.15K$ and $1bar$, the deviation is 4% at the most of when the concentration of one gas component varies from 1 to 0.

The presented theory determines the diffusion coefficient of a binary gas mixture as a bulk property, ignoring the fact that there are two very different gases in this mixture, which move and hence diffuse individually. However, other methods like NMR experiments or radio isotopes tracers observe only one isotope, which means that when the diffusion is measured by these methods, only the motion of this very isotope is measured. For example, in a Xe–He gas mixture, the lighter isotope (He) will move faster than the average, a fact not included in the presented theory.

A semi-empirical equation was proposed by Wilke [Wilk50], which was found to describe the observed effects very accurately. This equation describes the diffusion coefficient of one species, i, in a mixture with L others ,

$$\frac{1 - x_i}{D_i} = \sum_{j \neq i}^{L} \frac{x_j}{D_{i,j}} \tag{5.5}$$

with x_i as a concentration of the spice-i in the gas mixture and $D_{i,j}$ the binary diffusion coefficient of component i with respect to the component j in the mixture. For the case of a mixture of two species of different gases, a further development of Eq.5.5 leads to the following semi-empirical approximation of the observed diffusion coefficient $D_1(x)$ of one species of the gas mixture, as a function of its molar fraction, x ,

[2] See page 606 on [Hirs65]

[Mair02]:

$$\frac{1}{D_1(x)} = \frac{x}{D_1(1)} + \frac{1-x}{D_1(0)} \tag{5.6}$$

where the subscript 1 denotes the diffusion coefficient of the studied species, and not of the bulk gas. When the molar fraction is 1, $D_1(1)$ is the self diffusion coefficient of the detected isotope and when the molar fraction is 0, $D_1(0)$ denotes the diffusion coefficient of the detected isotope in an infinite dilution in the buffer gas.

5.2 Concentration measurement

Originally it was intended to use independent analytical techniques (e.g. mass spectroscopy, gravimetry or partial pressures) to determine the gas concentrations, but quantification even within a few percent was not possible with the available equipment. In the course of the experiments it turned out that NMR was the most precise way to determine the concentrations.

As explained in section 3.3, the mixture process begins with a sample tube filled with laser polarized (LP) gas, which is placed in the NMR coil while being connected to the gas handling system. A sequence –e.g the one depicted in Fig.2.12 b)– is run and a a reference signal is obtained for the initial concentration of the LP-gas. After mixture and release to the initial pressure another sequence is run. Taking into account possible signal losses due to T_1 effects and other experimental influences, the difference between signals of both sequences indicate the loss of LP-gas due to admixture.

5.2.1 Concentration and gas admixture

The molar fraction established by the procedure described above can be calculated as follows. The procedure starts with n moles present in the volume V of the sample tube at a pressure p and ambient temperature T. All measurements of the diffusion coefficient are done under the same conditions of pressure, temperature and volume, so that $n = pV/RT = \text{constant}$. When m_1 moles of buffer gas are pressed in the volume V, the LP-gas is diluted by a factor x_1, which is the molar fraction of the first mixture

$$x_1 = \frac{n}{n+m_1}. \tag{5.7}$$

The pressure is then released to p. However, this leaves the molar fraction unchanged, so that the remaining number of LP-gas moles in volume V follows the relation $n_1 = x_1 n$, which can be rewritten as

$$n_1 = \frac{n^2}{n+m_1}. \tag{5.8}$$

With the same reasoning the molar fraction of buffer gas does not change when the pressure is released to p, so that the number of moles, m_1', of buffer gas remaining in V are given by

$$x_{BG} = \frac{m_1'}{n} = \frac{m_1}{n+m_1} \Rightarrow m_1' = \frac{nm_1}{n+m_1}. \tag{5.9}$$

Repeating the procedure, that is, pressing m_2 moles of buffer gas in the sample, the LP-gas molar fraction will be

$$x_2 = \frac{n_1}{n_1+m_1'+m_2} = \frac{\frac{n^2}{n+m_1}}{\frac{n^2}{n+m_1}+\frac{nm_1}{n+m_1}+m_2}, \tag{5.10}$$

which can be understood as

$$x_2 = \frac{n}{n+m_1}\frac{n}{n+m_2} = x_1\frac{n}{n+m_2}. \tag{5.11}$$

For the k^{th} experiment this can be generalized as

$$x_k = \prod_{i=1}^{k}\frac{n}{n+m_i}. \tag{5.12}$$

5.2.2 Relation between signal and concentration

The determination of the molar fractions will be carried out through inspection of the signal intensity of the first signal acquired in each measurement before runnig the sequence to determined the diffusion coefficient. The initial magnetization is M_0. After the sequence run (diffusion measurement in this case) the signal will be reduced due to the application of N r.f. pulses,

$$M_1^* = \cos^{N-1}\alpha M_0 \tag{5.13}$$

where the supraindex * denotes the magnetization before mixture and α is the r.f. tip angle, which is typically small (2 to 5 degrees) when used hyperpolarized samples [Haas86]. Relaxation due to the gas collision with walls of the sample will be ignored as the total duration of the experiment is only around 1 minute, while the typical relaxation time T_1 of the used samples is measured to be around 50 times larger. After buffer gas is pressed into the sample and the exceeding pressure is released to p, the

magnetization will become

$$M_1 = M_1^* \frac{n}{n+m_1} = \cos^{N-1}\alpha M_0 x_1. \tag{5.14}$$

If this is repeated for a second time, the magnetization after releasing to P will become

$$M_2 = M_2^* \frac{n}{n+m_2} = \cos^{N-1}\alpha M_1 \frac{n}{n+m_2} = (\cos^{N-1}\alpha)^2 M_0 x_2. \tag{5.15}$$

This expression can be generalized for the k^{th} experiment as

$$M_k = (\cos^{N-1}\alpha)^k M_0 x_k. \tag{5.16}$$

The signal acquired will be $S_k \propto M_k \sin\alpha$, hence the following expression is used to obtain the LP-gas molar fractions from the measurement of the initial signal, S_0:

$$x_k = \frac{S_k}{S_0(\cos^{N-1}\alpha)^k}. \tag{5.17}$$

5.2.3 Error estimation

Another aspect of the setup that can influence the molar fraction determination is a small residual volume that lies between the volume of the sample contained inside the r.f. coil and gas mixing valves . The polarization of the gas present in this volume will not be affected by the r.f. pulses, hence leading to a systematic error in determination of the molar fraction. This volume was minimized as far as possible and determined to be 5% of the volume contained inside the r.f. coil. The pulse tip angle was determined by running the whole sequence for measuring $D(x)$ with pure LP-gas and setting the factor $\cos^{N-1}\alpha$ so that the molar fraction calculated was equal to unity. The error in the tip angle was determined to be lower than $\Delta\alpha = 5\%$. However, this error propagates during the course of the experiments (k mixtures excited by N r.f. pulses each). Error propagation of Eq.5.17 results in an error Δx_k of the determined molar fraction x_k of the LP-gas as

$$\frac{\Delta x_k}{x_k} = k(N-1)\tan\alpha\Delta\alpha\,. \tag{5.18}$$

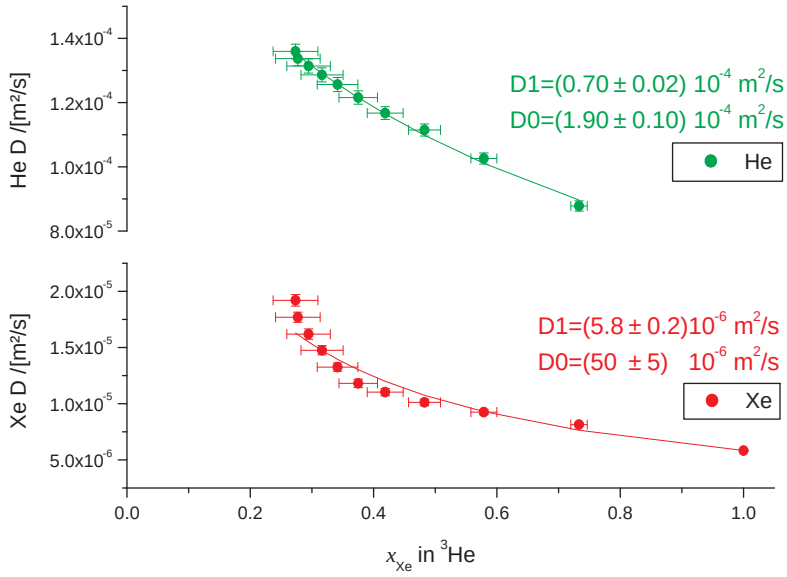

Figure 5.1: Simultaneous measurement of diffusion coefficient of ^{129}Xe and ^{3}He in a mixture versus concentration of Xe. Laser polarized ^{3}He was used as a buffer gas and mixed with LP-Xe.

5.3 Simultaneous measurement of *D* in a Xe–He gas admixture

In this section, the simultaneous measurement of D of ^{129}Xe and D of ^{3}He will be carried out in a mixture of Xe with ^{3}He as a buffer gas. After applying the same experimental procedure of section 4.2 in order to achieve a sample with LP-^{129}Xe at room temperature, the gas was transfered to a sample which fits in the coil length, and then released to $1bar$. Laser polarized ^{3}He was then introduced into the sample to dilute the Xe by means of the gas handling system described in section 3.3. The process was completely automated and synchronized with the NMR sequence to measure the diffusion coefficient with the sequence of Fig.2.12 b). In the case of Xe, the maximal gradient strength was $0.215T/m$, $\delta = 1050\mu s$ and $\varepsilon = 50\mu s$ as depicted in the Fig.2.12 b). In the case of ^{3}He, the maximal gradient strength was $0.0286T/m$, $\delta = 850\mu s$ and $\varepsilon = 50\mu s$.

After several experiences ^{3}He was chosen to be the buffer gas of the admixture and Xe the suitable gas to take as signal reference to calculate the concentration because the larger ^{3}He volume (ca. 1 L), which can be achieved with a pressure of almost 3 bar, produces a more stable admixture of this BG.

Figure 5.1 shows the simultaneous diffusion coefficient measurement of ^{129}Xe and ^{3}He. The upper points (in green) are the D_{He} and the line represents the fitting to the semiempirical function of Wilke (Eq.5.6). The lower part (in red) shows the same for D_{Xe}. The values displayed in both graphs, D_1 and D_0 represent the respective fitted values and their fitting error. Along the concentration axis, the error is given by Eq.5.18. The error in D is given by the linear fitting erros of the signal decay under different gradient strength taking into account pressure imperfections during the mixing procedure, which were determined to be less than 1%.

The higher the Xe concentration in the mixture the more the velocity of the ^{3}He atoms is slowed down due to kinetic energy absorption by Xe atoms in collisions. On the contrary, the velocity of the Xe atoms increases at higher ^{3}He concentration –or a smaller x_{Xe}.

5.4 $D_{\mathbf{He}}$ vs. $x_{\mathbf{He}}$ in ^{4}He, SF_6, N_2 and Xe: experiments and simulations

After observing the change of the ^{3}He diffusion coefficient by admixing Xe, a complete assortment of buffer gases will be applied. From lighter ones like ^{4}He to heavy ones like SF_6.

5.4.1 Determination by NMR

The experimental procedure is the same as in the previous section, but only the ^{3}He concentration is observed. In this case the maximum b-value corresponds to a diffusion gradient strength of $0.06T/m$ and the gradient timings were $\delta = 500\mu s$ and $\varepsilon = 50\mu s$ following the representation in Fig.2.12 b).

In Fig.5.2 the inverse of D_{He} under different buffer gases can be observed. The lightest one, ^{4}He, has almost no influence on the diffusion coefficient. On the other extreme, SF_6 produce a change of almost one order of magnitude in the extrapolation $x_{\mathrm{He}} \rightarrow 0$. Values for such extrapolation are presented in the Tab.5.1 following the linear regression of Eq.5.6. The standard deviation uncertainties resulting from the statistical error in the regression analysis of the measured D are less than 5% for all the measurements of the figure.

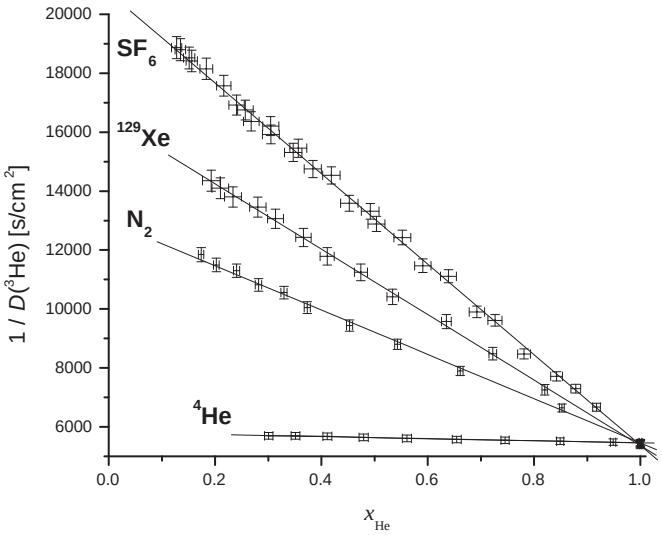

Figure 5.2: Inverse of ^{3}He diffusion coefficient obtained by NMR measurements as a function of the helium molar fraction, x_{He}, for binary mixtures corresponding to four different buffer gases (^{4}He, N_2, Xe and SF_6). The vertical error bars are the errors of the fitted diffusion coefficients, while the horizontal errors were estimated by Eq.5.18. The solid lines show the fits of Eq.5.6 to the data. The binary diffusion coefficients are found by extrapolating the fit to $x_{He} \rightarrow 0$. The obtained results are summarized in Tab.5.1.

5.4.2 Molecular dynamics simulations

Classical molecular dynamics simulations, MD, under periodic boundary conditions have been carried out using the Gromacs simulation package [Lind01] with the help of Komin *et al*. [Acos06]. It was simulated ^{3}He upon a mixture with ^{4}He, N_2 and ^{129}Xe as buffer gases at molar fractions from 0 to 1 in steps of 0.1.

Atoms were modeled using pairwise 6–12 Lennard–Jones potentials:

$$V = 4\varepsilon \left[\left(\frac{\sigma}{r} \right)^{12} - \left(\frac{\sigma}{r} \right)^{6} \right] \tag{5.19}$$

with $r = |R_1 - R_2|$. N_2 was represented as a united atom. In the case SF_6, which has a more complex internal structure, the untited atom model would represent a considerable simplification. The alternative, an all-atom calculation, would mean that all seven atoms have to be described independently. This in turn would require a significantly smaller time-step of the MD simulations due to the fast internal vibrational modes of the molecule. The Lennard–Jones parameters ε and σ were taken from reference

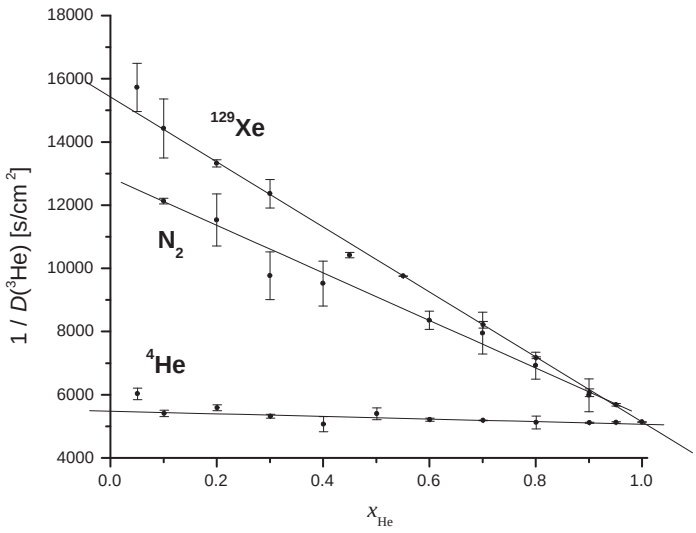

Figure 5.3: Inverse of ^{3}He diffusion coefficient obtained by simulations as a function of the helium molar fraction, x_{He}, for binary mixtures corresponding to three different buffer gases (^{4}He, N_2 and Xe). Error bars were estimated by comparing the diffusion coefficients obtained from the first and the second half of the simulation. The solid lines show the fits of Eq.5.6 to the data. The binary diffusion coefficients are found by extrapolating the fit to $x_{\mathrm{He}} \to 0$. The obtained results are summarized in Tab.5.1.

[Raid87]. Their values are ε(Xe) = 231 K, σ(Xe) = 4.047 Å, ε(He) = 10.22 K, σ(He) = 2.551 Å, ε(N_2) = 71.4 K and σ(N_2) = 3.798 Å. For interactions between particles of different species, the combination formulae

$$\varepsilon_{i,j} = \sqrt{\varepsilon_i \varepsilon_j} \quad \text{and} \quad \sigma_{i,j} = (\sigma_i + \sigma_j)/2 \tag{5.20}$$

were used.

For the thermodynamic parameters of the binary gas mixtures, the equation of state of an ideal gas was assumed. In order to match the experimental pressure and temperature, simulation boxes of $205379nm^3 = (59nm)^3$ containing 5000 particles were used for the ^{3}He–^{4}He and ^{3}He–^{129}Xe mixtures. A check on the equivalent systems with only 500 particles yielded only insignificant deviations from the corresponding 5000 particle runs. Hence, we used only 500 particles for the ^{3}He–N_2 system. For the equilibration of our systems, the particles were placed at random positions in the box and brought to the desired temperature $(T = 294K)$ by a canoni-

cal[3] (NVT) molecular dynamics run for $20ps$. Subsequently, production runs of $10ns$ length were performed in the NVE ensemble[4] , with a time step of $2fs$.

Diffusion coefficients were computed from the production runs by fitting the root mean square displacement, averaged over all atoms of a given species-i, to the elapsed time, assuming the Einstein-Smolochowski relation

$$\langle R_i(t) - R_i(0)\rangle^2 = 6D_i t \tag{5.21}$$

Error bars were estimated by comparing the diffusion coefficients obtained from the first and second half of the simulation. The simulations were performed on a parallel 16-processor Beowulf cluster with 2.6 GHz Xeon processors and required about 2000 CPU hours in total.

The simulated dependence of the binary diffusion coefficients in the ^{3}He–^{4}He, ^{3}He–N_2 and ^{3}He–^{129}Xe mixtures on x_{He} is shown in Fig.5.3. The qualitative and quantitative agreement with the values obtained from the NMR experiments shown in Fig.5.2 is within the 5% error. In all cases, the shape $D_{He}(x_{He})$ is correctly obtained in the molecular dynamics simulations, even for the subtle ^{3}He–^{4}He case. Although there is still significant noise in the computed diffusion coefficients, the substantial reduction due to the admixture of heavier and larger components is nicely reproduced, hence supporting the experimental findings presented.

Table 5.1 summarizes values for the binary diffusion coefficient from Eq.5.1 as well as the ^{3}He free diffusion coefficient and extrapolation when $x_{He} \to 0$ obtained by NMR and by molecular dynamics simulations. Diffusion coefficient absolute values agree well within the 5% error.

5.5 D_{Xe} vs. x_{Xe} in ^{3}He and N_2: experiments and simulation

Unlike the case of ^{3}He, only two buffer gases had been mixed with Xe: ^{3}He and N_2. The mixture with ^{3}He had been already presented in section 5.3. In Fig.5.4 this measurement is compared with the simulation. The fitted values agrees very well, however

[3] NVT ensemble: the number of particles (N) and the volume (V) of the system are hold constant during the simulation and a well defined temperature (T) is imposed by coupling the system to an external heat bath. The system is allowed to exchange energy with the reservoir, and the heat capacity of the reservoir is assumed to be so large as to maintain a fixed temperature for the coupled system.

[4] NVE ensemble: the number of particles (N), the volume (V) and the internal energy (E) are hold constant during a MD simulation.

$D(0)^3$He/[$\cdot 10^{-4} m^2/s$]	^{3}He	^{4}He	N_2	Xe	SF_6
$D_{1,2}$ Eq.5.1	1.84	1.72	0.77	0.615	0.418
NMR	1.8	1.7	0.77	0.7	0.48
Simulation	1.96	1.86	0.8	0.63	–

Table 5.1: ^{3}He binary mixed diffusion coefficient comparison within an infinite dilution of different buffer gases: ^{4}He, N_2, Xe and SF_6. The different $D(0)$ are from top to bottom respectively: calculation of binary diffusion coefficient $D_{1,2}$ from Eq.5.1, fitted to NMR measurements of Fig.5.2 by Eq.5.6 and fitted to simulations of Fig.5.3 by Eq.5.6. The fitted parameters error estimation is determined to be less than 5%.

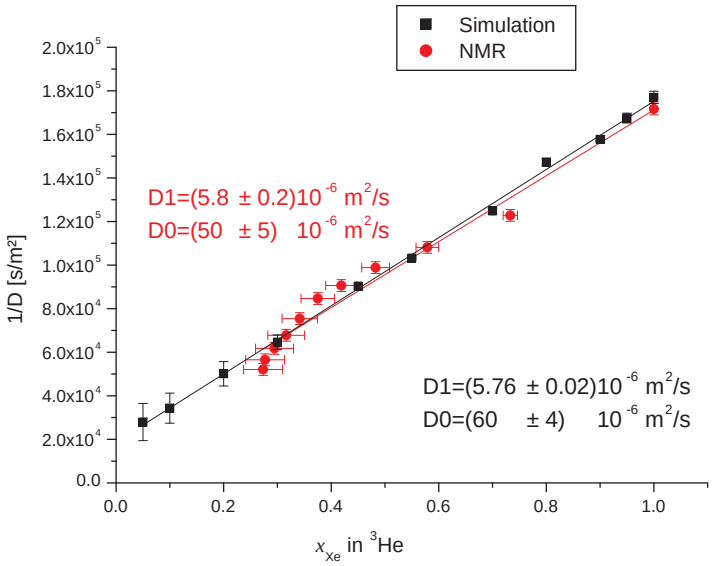

Figure 5.4: Diffusion coefficient of ^{129}Xe versus concentration of a mixture with ^{3}He. Measurement (same as Fig.5.1) and simulation are presented.

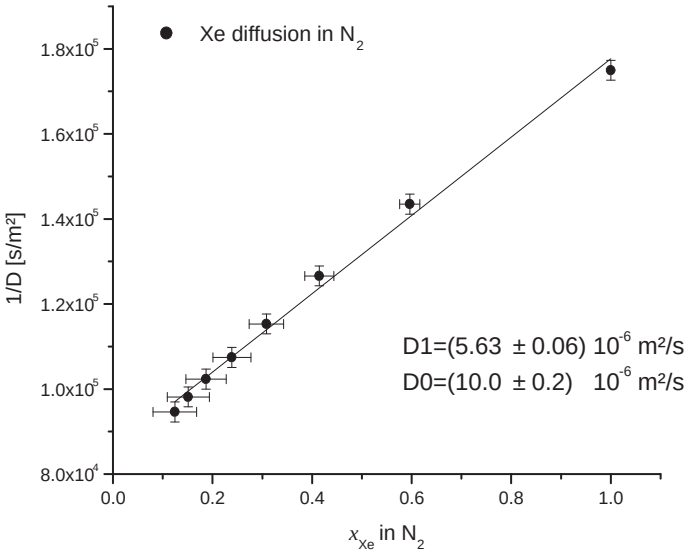

Figure 5.5: NMR experimentally determined data: diffusion coefficient of ^{129}Xe versus concentration in a mixture with N_2.

for concentrations $x_{Xe} < 0.4$ measurements tend to deviate from their espected linear behaviour, which does not happen with simulated data.

One possible origin of these deviations is inhomogeneity of the concentration within the sample volume. Local fluctuations or even gravity could cause a locally increased Xe concentration, whose Xe diffusion would be significantly reduced with respect to a perfectly homogeneous gas mixture. This effect would correspond to an effective increase in the Xe mole fraction, hence bringing the experimental D closer to the simulated value. Additionally both, experimental and simulation, have increasing errors with decreasing numbers of observed particles, which might also add to this discrepancy. A further uncertainty caused by the curvature of the inverse Xe diffusion coefficient at these lower concentrations complicates the extrapolation for $x_{Xe} \to 0$.

In the case of the mixture Xe–N_2, only experimental points are shown, see Fig.5.5. These measurements follow better a linear behaviour in comparison with the ^{3}He–Xe admixture. However, a small tendency is observed here like in the previous case, which can have the same origin. The minor molecular weight of N_2 in comparison with Xe can also be a reason for the less influence of the described error factors and hence, for a better agreement with a linear behaviour.

The obtained D values extrapolated for $x_{Xe} \to 0$ and the theoretical predicted values are listed in Tab.5.2. A good agreement is obtained for the experimental data

$D(0)^{129}$Xe/[$\cdot 10^{-6} m^2/s$]	Xe	^{3}He	N_2
$D_{1,2}$ Eq.5.1	5.52	61	8.8
NMR	5.7 ± 0.1	50 ± 5	10.0 ± 0.2
Simulation	5.76 ± 0.02	60 ± 4	–

Table 5.2: ^{129}Xe binary mixed diffusion coefficient comparison within an infinite dilution of different buffer gases: ^{3}He and N_2. The different $D(0)$ are from top to bottom respectively: calculation of binary diffusion coefficient $D_{1,2}$ from Eq. 5.1, fitted to NMR measurements by Eq.5.6 and fitted from simulations to Eq.5.6. Errors were obtained from the fitting error.

set with the theoretical prediction given by the binary diffusion coefficient, $D_{1,2}$. There are some minor discrepancies where the simulated xenon diffusion coefficient at low Xe concentrations is slightly different from the measured one.

5.6 Conclusions

In this chapter an experimental setup and protocol for achieving a controlled binary gas mixture –and hence a controlled diffusion coefficient– in which one of the gas components is a noble LP gas is presented. The experiments can be performed at pressures from $0.05 bar$ to $2 bar$ [Zaen07], however, for an approximation to clinical conditions, the measurements at ambient pressure are the best choice. The gas mixing is controlled by pneumatic valves which are driven from the spectrometer, enabling a synchronized timing with the pulse sequences and complete automation of the experiment. The molar fraction determination is performed by direct inspection of the NMR signal assuming that the only source of loss of magnetization is produced by the r.f. excitation. This strategy turned out to be more accurate than other standard techniques for quantitative analysis of mixtures of gases with very different molar masses. This setup was then used for the simultaneous measurement of the diffusion coefficient of ^{3}He and Xe as a function of the Xe molar fraction. ^{3}He in binary mixtures with other three different inert buffer gases (^{4}He, N_2 and SF_6) were presented as well as ^{129}Xe diffusion coefficient as a function of its molecular fraction upon a mixture with N_2.

The agreement between the experimentally measured diffusion coefficients with those obtained from molecular dynamics simulations and analytical expressions is very good, in particular for ^{3}He. The dependence of the ^{3}He diffusion coefficient in a BG on the molar concentration in mixtures with BG = N_2 and BG = Xe is neatly reproduced, illustrating the possibilities of fine-tuning diffusion properties of a gas by

the admixture of another one of different molecular mass. In the case of the ^{129}Xe diffusion data, the agreement between experiment and simulation is somewhat not so satisfactory. This might be due to the approximations in the Xe–Xe and Xe–He interaction potentials in the molecular dynamics simulations, but could also be explained by an imperfect experimental setup as discussed above.

In the porous media research, diffusion plays an important role for determination of pore size, distribution and shape [Mair02] [Sen04]. Since a wide range of D can be achieved with gas admixture, the mixture procedure shown represents a new technique to improve porous media research. In the case of the lung, the control of the diffusion coefficient is important (not only from the point of view of porous media) but also for the spatial resolution in MRI, since diffusion influences the NMR signal by means of the point spread function (*PSF*). Reducing the diffusion coefficient is hence important for minimizing *PSF* effects and thus the spatial resolution. In this sense, Xe could represent a good candidate for lung MRI, however, the lower NMR signal, the lipophilicity and anaesthetic effects of Xe turn it not so much profitable for this purposes. Some attempts had been made to reduce the diffusion coefficient of Xe with heavier molecules like SF_6 [Mair00], however, the authors conclude that replacing ^{129}Xe with SF_6 will both lower the NMR signal and have minimal effect on $D_{\mathrm{Xe}}(x_{\mathrm{Xe}} \rightarrow 0)$. Even in the case where a benign buffer gas is required to increase the total sample pressure, a similar reduction in diffusion can be obtained simply by adding more ^{129}Xe, with the side benefit of increased NMR signal.

These considerations, among others, fovour the use of ^{3}He as the candidate for lung MRI. Thus a deeper knowledge of the influence of helium diffusion on spatial resolution is required, task that will be carried out in the next chapter.

Chapter 6

Influence of diffusion in MRI

Usually clinical NMR images show the ^{1}H density inside the body. The diffusion coefficient, D, of these protons is on the order of $D_{water} = 2 \cdot 10^{-9} m^2/s$ at 25°C, which is five orders of magnitude smaller than that for ^{3}He. Spatial resolution of this gas will be therefore more affected by diffusion. In the previous chapter, the control of D in gases by means of addition of buffer gases (BG) was presented showing that an attenuation of the diffusion coefficient of almost an order of magnitude is possible. Diffusion coefficient control is necessary to handle the problem of the influence of D in the signal, and hence in images [Acos06b].

In this chapter the influence of $D(x)$ in ^{3}He MRI by means of the Point Spread Function (PSF) is presented. It is shown, that the signal can be optimized by varying the mixture and hence the effects of diffusion on images as "edge enhancement" and "motional narrowing". The sensitivity and spatial resolution achievable for restricted gas is analyzed. One-dimensional images of mixtures of laser polarized (LP) ^{3}He with N_2, in restricted geometries shows that the control of gas mixtures concentration can be used as a contrast agent to determine structures size in images, as well as the admixture with different weight BG, shown in the more realistic case of a lung.

6.1 Spatial resolution and point spread function

Spatial resolution is conceptually easiest explained by discussing the point-spread function, $PSF(\mathbf{r})$, which convolves the pure spatial information, $\rho(\mathbf{r})$ [Ross69]. The width of the point spread function in relation to the width of an image pixel directly gives a measure of the spatial resolution. An NMR-image, $I(\mathbf{r})$, is then described by the following convolution

$$Image \Rightarrow I(\mathbf{r}) = PSF \otimes \rho(\mathbf{r}) + noise\,. \tag{6.1}$$

The width of the point spread function can be directly obtained by switching the "spatial term" off, i.e. by measuring at gradient strength zero ($G = 0$) and then Fourier transform the result.

- Frequency encoding

The frequency encoded dimension is then simply the normal NMR-spectrum, and the maximum dispersion of chemical shifts or line width determines the total width of the *PSF*, $\Delta\omega$, hence the blurring of the image along this dimension. The minimum resolved distance, Δr , is consequently defined by the width of the *PSF* and the (spatial) frequency spread by the read gradient, γG_{read}

$$\Delta r_{Fre} = \frac{\Delta\omega}{\gamma G_{read}} \quad \text{or} \quad \Delta r_{Fre} = \frac{\pi}{\gamma G_{read}\delta} \tag{6.2}$$

where δ is the half of the acquisition time (see Fig.6.1). From this equation it is obvious, that if the line width increases, the resolution decreases accordingly, unless the gradient strength is enlarged. This explains the difficulties of NMR imaging of solids, where line widths can be 5 or more orders of magnitude broader than in liquids, because the dipole-dipole interactions are no longer averaged out as a consequence of reduced mobility.

- Phase encoding

The situation is quite different when the spatial information is obtained via phase-encoding with constant evolution time. If the gradient is switched off, nothing is varied, hence resulting in a constant which Fourier-transforms into a delta-function. That means that the *PSF* has no width, and the minimum resolvable distance Δr is no longer determined by any intrinsic NMR-parameter, but exclusively by instrumental variables, namely the maximum gradient amplitude G_{max} and the evolution time τ (see Fig.2.7) as

$$\Delta r_{Pha} = \frac{2\pi}{\gamma G_{max}\tau}\,. \tag{6.3}$$

Similar considerations hold for the influence of self-diffusion on the resolution. The random walk of the observed molecules causes a spatial offset, which can blur the image in the frequency encoded dimension. This happens according to the Einstein-Smoluchowski equation, rewriting Eq.2.61 for 1D case:

$$\Delta r = \sqrt{2D\Delta t} \tag{6.4}$$

where D is the self-diffusion coefficient and Δt a sampling interval with which the signal is recorded. Furthermore, self-diffusion also has a strong influence on the amplitude of the point-spread function, which is given by

$$PSF = \exp\left(-\gamma^2 D G^2 m \frac{\delta^3}{3}\right) \equiv \exp(-bD) \tag{6.5}$$

where $m = 2$ for the frequency encoded dimension, $m = 1$ for the phase encoded dimension and δ is the gradient length as depicted in Fig.2.7. The influence of self-diffusion is usually smaller than chemical shifts, dipolar couplings and other interactions as long as liquids are considered. For water as an example a typical experimental setup gives $\Delta r \approx 0.3\mu m$ and a $PSF \approx 0.999999$ which is negligible.

- Gases

In difference to liquids the main cause of resolution limits may be expected from rapid Brownian motion of the gas atoms, since D is 4 orders of magnitude larger than liquids. The same experimental values in the example above give for ^{3}He a $\Delta r \approx 90\mu m$ and a $PSF \approx 0.5$ for the frequency encoded dimension, which are both substantial.

However, this calculation assumes free, unrestricted diffusion. In a realistic sample, one will find walls, which restricts the diffusivity of the gas atoms close to them. Pores will cause restricted diffusion of the gas inside their entire volume. In such situations the effective diffusion coefficient can also be estimated by the Einstein-Smoluchowski equation when the pore size, r , is smaller than a critical distance, r_c

$$r_c = \sqrt{2D_0\Delta\tau} \tag{6.6}$$

where D_0 is the coefficient for free diffusion, so that the effective diffusion coefficient can be approximated as

$$D = \begin{cases} \frac{r^2}{2\tau} & \text{for } r < r_c \\ D_0 & \text{for } r > r_c\,. \end{cases} \tag{6.7}$$

The spatial restriction by pore walls therefore reduces the effective diffusion coefficient and increases the amplitude of the diffusion PSF in Eq.6.1. From these facts it is expected, that MRI of laser polarized (LP) gases in porous media lead to better resolved images. Consequently it is of interest to investigate how the “coherent” resolution, Δr, of the image in Eq.6.2 is related to the size of a pore, r, and whether there

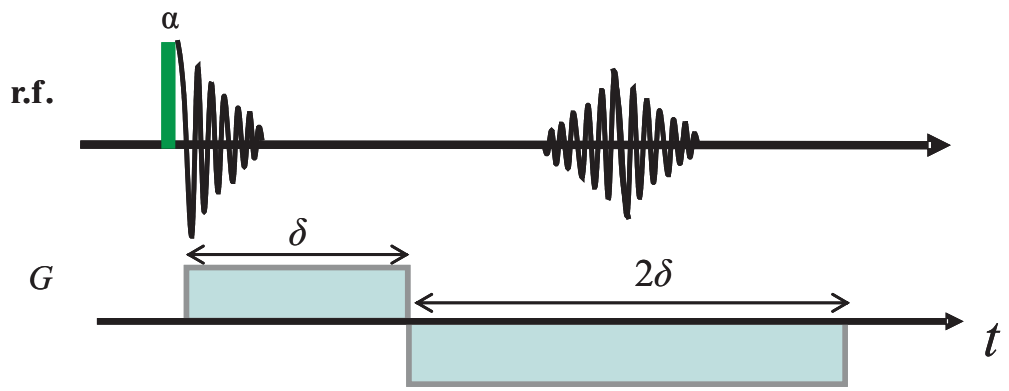

Figure 6.1: Gradient echo sequence used to measure the signal under a frequency encode gradient at different concentrations

is an optimum of resolution, respectively sensitivity. For such a relation one has to combine Eq.6.2, Eq.6.4 and Eq.6.7 giving [Acos06b]

$$PSF = \exp\left(-\frac{\pi r^2}{6\Delta r^2}\right) . \tag{6.8}$$

6.2 Optimal mixture in non restrictive geometries

Equation 6.1 shows the factors that play an important role for the image intensity. On one hand the *PSF*, which include sequence parameters –as timing and gradient strength– and *D*. On the other hand the density distribution, $\rho(\mathbf{r})$.

In order to optimize the *PSF* sequence parameters have some restrictions due to the necessary field of view, FOV, and technical means. In the case of medical MRI, the restrictions are even more important since human bodies can not suffer high gradient strength. The other parameter left to correct is the *D*. In the previous chapter it was shown how *D* can be controlled by admixture of BG; to improve the signal intensity the lowest *D* is required. Although *D* can be reduced an order of magnitude in the case of ^{3}He, the admixture has the draw back of diluting ^{3}He and hence reducing $\rho_{^3\mathrm{He}}(\mathbf{r})$.

Both factors, *D* and $\rho(\mathbf{r})$, are concentration dependent and hence the signal intensity. On one hand the more concentration , or $\rho(\mathbf{r})$, the more signal. On the other hand, the less concentration the less *D* and so the larger the signal as follows:

$$Sig(x) \propto x \cdot \exp\left[\frac{-b}{x/D_1 + (x-1)/D_0}\right] \tag{6.9}$$

where $Sig(x)$ is the signal, x the concentration, D_1 and D_0 denotes respectively the self diffusion coefficient and the diffusion coefficient in an infinite dilution of BG, and

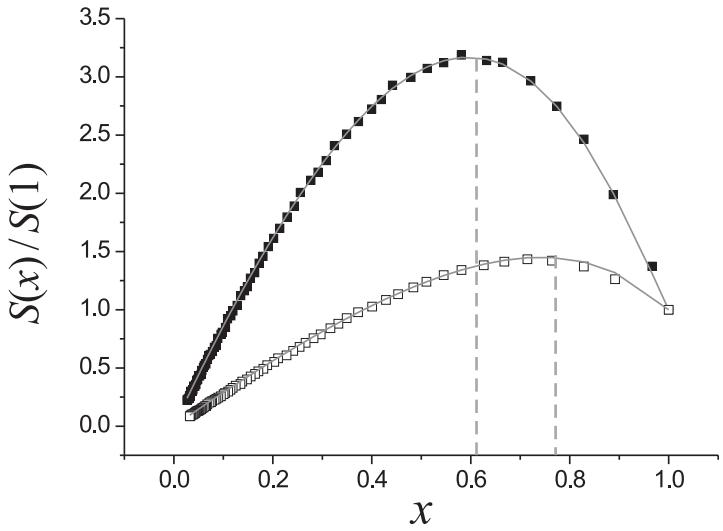

Figure 6.2: Signal dependence of freely diffusing ^{3}He as a function of its molar fraction in admixture with the buffer gas SF_6 following the sequence of Fig.6.1. For two b-values, $\square b = 6758 s/m^2$ (realized with Gread $= 86.4 mT/m$ and $\delta = 320 \mu s$) and $\blacksquare b = 13525 s/m^2$ (realized with Gread $= 43.2 mT/m$ and $\delta = 640 \mu s$). The ordinate is the NMR-signal normalized to the value at $x = 1$. The curves show Eq.6.11 using the diffusion coefficients from Tab.5.1. The dashed lines are the values of x_{opt} calculated from Eq.6.10.

$b = 2\gamma^2 G^2 \delta^3/3$, represents the sequence parameters depicted in Fig.6.1.

From Eq.6.9 an optimal concentration that compensate $\rho(\mathbf{r})$ and D will be given by

$$x_{opt} = \frac{D_1}{2(D_1 - D_0)} \left[2 + bD_0 - \sqrt{4bD_0 - (bD_0)^2} \right]. \tag{6.10}$$

Free diffusive LP-^{3}He was diluted with SF_6 following the mixture procedure of the experiments of chapter 5. Figure 6.2 shows the maximum gradient echo signal given by the sequence depicted in Fig.6.1 at different concentrations. The signal is plotted for 2 different b-values, which are typical in MRI, and normalized to $x = 1$ as well as Eq.6.9, obtaining

$$S(x) = \frac{Sig(x)}{Sig(1)} = x \exp\{-b[D(x) - D_1]\} \tag{6.11}$$

where $D(x)$ is given by

$$D(x) = \frac{1}{x/D_1 + (x-1)/D_0}\,. \tag{6.12}$$

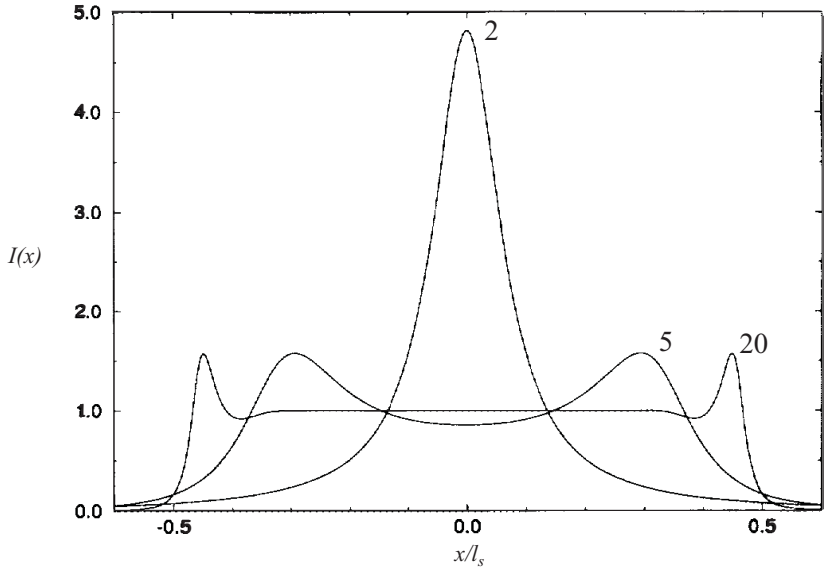

Figure 6.3: Analytical one-dimensional image in x-direction ($I(x)$) of a slab of size l_s obtained by frequency encoding with three different gradient strength $l_s/l_G = 2,5,20$. The crossover from slow ($l_s = 20l_G$) to fast ($l_s = 2l_G$) exchange regime is noticeable. Picture from [Swie95]

The optimal concentration is marked with dashed lines following the Eq.6.10. The optimal concentration, x_{opt}, depends on the b-value, as it can be observed in the figure or in Eq.6.11. The signal is enhanced up to 3 times thanks to the mixture for a $b = 13525 s/m^2$, or in other words, the diluted ^{3}He exhibits 5 times of the expected signal in x_{opt}. Hence, the somewhat counter intuitive situation arises, that less signal carrying substance results in an increased MRI-signal. In both cases, the measurements show a very good agreement with Eq.6.11.

6.3 Edge enhancement

The random movement of spins makes it practically impossible to recover completely the coherence, acquiring an echo attenuated by diffusion. In restriction cavities, however, due to collisions with the container, there is less diffusion and therefore less attenuation near a restriction. Thus, the signal in the edges won't be as attenuated as under certain circumstances.

In order to describe these circumstances, three lengths have to be defined. The first is the distance that a particle covers due to its diffusion, the so-called root mean square displacement, Δr, given by the Einstein-Smoluchowski equation, Eq.6.4. The second is the dephasing length due to the diffusion and related to the read gradient

strength as described in [Swie94], given by

$$l_G = \sqrt[3]{\frac{D}{\gamma G}} \tag{6.13}$$

where D is the diffusion coefficient, γ the magnetogyric ratio and G the read gradient strength in a frequency encoding sequence. The third length is, of course, the restriction distance of the cavity, l_s, which contains the NMR-isotope.

Taking into account these lengths, two regimes can be considered. The "fast-exchange" regime when the isotope diffuses throughout the enclosure during the life time of the experiment, i.e. $l_s << l_G, \Delta r$, and the "slow-exchange" regime when most of the spins do not contact a wall during the life time of the experiment, i.e. $l_s >> l_G, \Delta r$, and the diffusive distortion is confined to a boundary layer of spins near to the walls.

Figure 6.3 represents the calculated one-dimensional image calculated by de Swiet [Swie95]. The equation that describes this image depends on a sum of eigenfunctions. For a given l_s/l_G only a finite number of them have complex eigenvalues. In the "slow-exchange" regime, the number of complex eigenvalues tends to infinity and the eigenfunctions become increasingly localized. The eigenfunction nearest the walls decay slowest and thus have the smallest width. Consequently these are the sharpest and highest peaks in the image, obtaining a better resolution. In Fig.6.3 this effect is shown for the curve marked with "20", referenced to $l_s = 20 l_G$.

In the quantitative theory presented in the work of de Swiet [Swie95], the regime change is done by increasing the gradient strength and thus l_s/l_G. In the case of gases, another way of increase l_s/l_G can be done by decreasing D in Eq.6.13. Figure 6.4 shows a set of one-dimensional images of a $3mm$ slab at different concentrations of ^{3}He with N_2 at a total pressure of $1bar$. All images were normalized to their maximum. The ratio l_s/l_G took values of 17 for $x \to 0$ (see fig6.5), very close to the "slow-exchange" regime (see $8th$ row of Tab.6.2 for more details). Nevertheless, the increasing of the *PSF* (see Fig.6.5) reduces the loss of signal in the middle of the slab and, instead of getting a acute edge enhancement, a constant signal without diffusional effects is acquired.

6.4 Motional narrowing

A particular effect related to the high diffusivity is the "motional narrowing", which accumulates locally the signal and produces signal enhancement. Motional narrowing

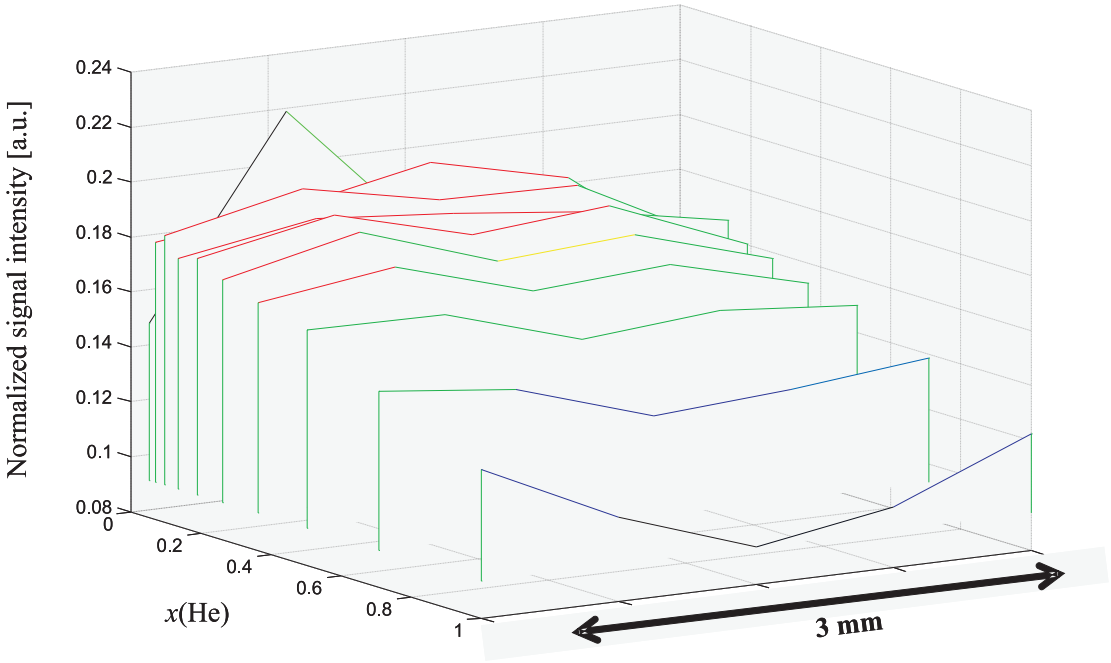

Figure 6.4: One-dimensional images of a $3mm$ restricted cavity at different concentrations of ^{3}He mixed with N_2. Images at $1bar$ were normalized to their maximum signal and taken with the following parameters: $G_{read} = 74mT/m$ and $SW = 2 \cdot 10^5 Hz$.

occurs when spins move back and forth so frequently that spins in different chemical sites have no time to accumulate a significant phase difference, thus all spins have the same average precession frequency.

The motional narrowing is rather related to the "fast-exchange" regime. In the work of de Swiet [Swie95], for values $l_s \approx 2.264 l_G$, there are no complex eigenvalues and the ratio of 2.264 can be defined as the beginning of the "fast-exchange" regime or motional narrowing regime. In Fig.6.3 the central peak, marked with a "2", what means $l_s = 2l_G$, shows an example of the described effect.

Concretely in images, when an encoding magnetic gradient is applied in bounded medium containing an NMR observable isotope and the root mean squared displacement of spins is several times the motion restrictive length, all the resonances are at the average frequency of the container and consisting the image in a single Lorentzian resonance line, as shown in [Hieb06] [Wayn66].

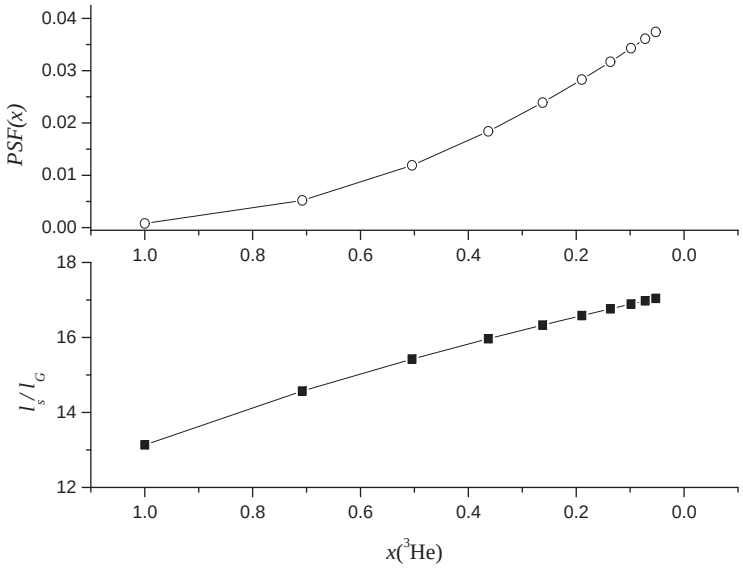

Figure 6.5: The top graph shows the *PSF* values versus concentration with parameters of Fig.6.4. In the bottom graph is represented l_s/l_G getting closer to 20; the critical ratio of slow-exchange regime. However the increase of the *PSF* under different concentrations make up for this regime change, as observed in Fig.6.4.

6.5 Influence of experimental NMR-parameters in restrictive cavities

The effects related to diffusion –edge enhancement and motional narrowing– can be partially reduced by combining a proper timing and adjusted gradient strengths. Nevertheless high diffusivity of ^{3}He makes it practically impossible to resolve a wide range of restrictive cavities sizes.

Figure 6.6 shows two sets of images of the sample of Fig.3.8, composed of collinear cylinders (stuck with epoxy), prepared to be filled with a gas (see section 3.4). All images in each set were taken with different resolution (acquired points) and acquisition time (dwell time: time in between two acquired points). The two columns on the left –from a) to d)–are filled with 100% ^{3}He at 1*bar*. The two columns on the right –from e) to h)– are filled with the same quantity of LP-^{3}He plus an additional *bar* of SF_6. The free *D* in the second case is five times smaller and hence the influence of the *PSF* will be less than the half compared with the 100% ^{3}He set of images.

The 2D images of Fig.6.6 were acquired using a gradient echo FLASH Cartesian

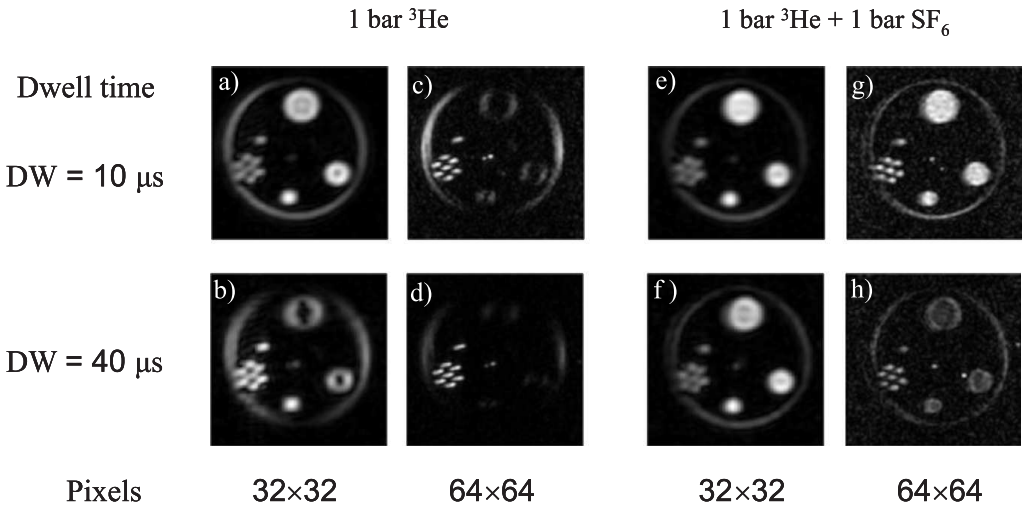

Figure 6.6: Gradient echo images of collinear cylinders at different resolution parameters; number of pixels and dwell time (time between data points). The first images block –"a" to "d")– consist on pure ^{3}He at $1bar$. The second images block –"e" to "h")– consist on $1bar$ of ^{3}He plus another of SF_6. A gradients strength of $106mT/m$ and spectral width of $100kHz$ were used in the "a)" and "e)" images, $26mT/m$ and spectral width of $25kHz$ were used in the "b)" and "f)" images, $53mT/m$ and spectral width of $100kHz$ were used in the "c)" and "g)" images and $53mT/m$ and spectral width of $25kHz$ were used in the "d)" and "h)" images.

sampling of *k*-space. Read gradient was set along the *x*-direction in all experiments while the phase gradient was set along the *y*-direction, the B_0 field was the *z*-direction. Tip angles of $\backsim 3^\circ$ were achieved by means of hard r.f. pulses of length of $5\mu s$. A gradient strength of $106mT/m$ and spectral width of $100kHz$ were used in the "a)" image. The gradient strength was changed accordingly to the acquisition time to keep the FOV constant in the other images. The images were zero filled to four times their dimension before Fourier transformation. An FID was acquired immediately before each image acquisition and the data were normalized to the corresponding FID intensity before Fourier transformation in order to avoid the influence of depolarization by r.f. excitation. Despite the capillaries an exterior ring is visible due to gas which occupies the volume between the epoxy cylinder and the glass container. The gray scale of all the images presented corresponds to its own maximum.

A comparison of the smallest capillary (exactly in the center of the phantom with a diameter of $0.5mm$) with the largest one (upper part of the phantom with a diameter of $3.2mm$) will be done, since these are the extreme cases imaged. The "a)" image has the shortest acquisition time and hence shorter root mean squared displacement,

$\Delta r \approx 0.34mm$. Only few atoms have time to collide with the capillary walls, even in the smallest capillary, where they are not enough to generate an appreciable signal. However, the largest capillary is resolved and, slightly, motional narrowing and edge enhancement effects can be observed. The in between size capillaries shows these both tendencies; edge enhancement in the capillary on the right and lack of spins in the set of capillaries on the left, only the capillary on the bottom has the precise size to be perfectly resolved.

For increased dwell times the atoms have enough time to diffuse, therefore, they collide with the capillary walls and are more restricted. In image "b)" the time is four times increased and $\Delta r \approx 0.5mm$. In this case, the spins in the smallest capillary (in the center of the phantom) are resolved because they are more restricted, but the image is strong diffusion weighted due to the large dwell time and then the large capillary (top of the phantom) is badly resolved, only edge enhancement is appreciable. Acquiring more points –c) and d) – is also no solution to improve the resolution since the acquisition time also increases – hence the image is more diffusion weighted– and only small capillaries are well resolved.

In the second set of images –from e) to h)– the mixture is presented. The smaller the diffusion coefficient the more its effects are reduced for the same configuration of timing and pixels, when both sets of images are compared. The smallest and the largest capillaries can be resolved in "e)", "f)" and "g)". In "h)" the low SNR does not permit to obtain a quality image. The image "g)", with a $\Delta r \approx 0.2mm$, presents the best image; all capillary sizes are homogeneously resolved and have the same intensity per pixel. It means that the real distribution of spins is perfectly represented by the signal intensity distribution in the image.

6.6 Cavity selection

In the previous section it has been shown that a wide range of cavity sizes can not be well resolved with a high diffusive NMR-isotope. The different restrictions, and hence the different apparent diffusion coefficient, ADC, influences the image by means of the *PSF* and produces signal enhance or decrease depending on the cavity size. In this section these effects are used to enhance or reduce the determinated cavity size, by means of diffusion coefficient control via mixture control or mixture with BG choice.

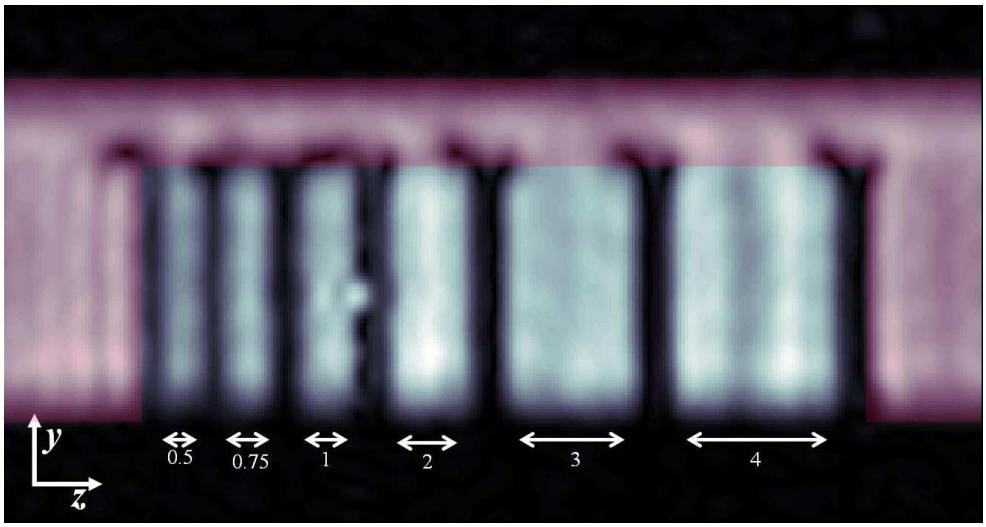

Figure 6.7: ^{3}He inside the phantom of Fig.3.9. Distances between planes are given in *mm*. The image was 8 times zero filled before Fourier transformation and corresponds to the mixture $x = 0.5$ of Tab.6.2. The reddish part was set to zero. Phase gradient was set along the *y*-direction and read gradient was set along the *z*-direction.

6.6.1 Concentration dependence

Due to the high ^{3}He concentration dependence of the D , as shown in Fig.5.2, concentration control can provide an important tool to enhance cavity size in NMR images. The synchronization of magnetic valves, which control the gas admixture, with the sequence console offers the possibility of achieving a desired concentration under certain known conditions (see section 3.3).

The phantom of fig 3.9 was designed to study a wide range of one-dimensional restrictions. It consists of a set of parallel planes separated by distances of alveoli size order to last part of bronchial tube i.e. 0.5, 0.75, 1, 2, 3, 4 *mm* (see Fig.6.7). The phantom was imaged at different concentrations of ^{3}He mixed with N_2 since it is the most close buffer gas to air, which permits a T_1 of $2880 \pm 20s$; long enough to reject lattice interaction influence in the concentration measurement during the experiment, which took ca. 120*s*. All images were acquired at 1*bar*.

Pixels outside the restriction walls were set to zero, reddish on Fig.6.7. The restriction walls were set perpendicular to the *z*-direction, which is the B_0 direction. Images were taken in the $y-z$ plane (see Fig.6.7), following a gradient echo FLASH sequence [Haas86] like the one depicted in Fig.2.7. Six points were acquired after the r.f. pulse ($\backsim 3°$) before applying the gradients to normalize each image and calculate the concentration. The signal was averaged out in the *y*-direction, i.e. the phase gra-

dient direction, in order to obtain one-dimensional images in the restricted direction. In all experiments the phase gradient was 32 times stepped with a maximum gradient intensity of $50mT/m$.

- Large acquisition time

$x(^3\text{He})$ in N_2	1	0.70	0.50	0.37	0.27	0.19
PSF	0	0	0.001	0.003	0.006	0.008
$\Delta r/[mm]$	0.68	0.58	0.53	0.51	0.49	0.48
$l_s(0.5mm)/l_G$	1.74	1.93	2.04	2.11	2.16	2.19
$l_s(0.75mm)/l_G$	2.61	2.90	3.07	3.16	3.24	3.29
$l_s(1mm)/l_G$	3.47	3.87	4.09	4.22	4.32	4.39
$l_s(2mm)/l_G$	6.95	7.74	8.18	8.44	8.63	8.78
$l_s(3mm)/l_G$	10.4	11.6	12.3	12.7	13.0	13.2
$l_s(4mm)/l_G$	14.9	15.5	16.4	16.9	17.3	17.6

Table 6.1: Parameters of a one-dimensional images of phantom of Fig.6.7 at different concentrations of ^{3}He with N_2 ($G_{read} = 37mT/m$ and $SW = 10^5Hz$). The first row are the concentrations at which the images were acquired. The second row are the PSF values which attenuate the signal by non restricted diffusion. Third row is root mean square displacement given by Eq.6.4. Rows $4th$ to $9th$ show the l_s/l_G values (which define the fast-exchange regime, $l_s/l_G \approx 2$, to slow-exchange regime, $l_s/l_G \approx 20$) at the restriction cavities.

Two sets of images are presented in this section with the same number of acquired points, 128, and two gradient strengths in read direction, G_{read}, and spectral width, SW, to keep the FOV. The first set of images was taken with a $G_{read} = 37mT/m$ and $SW = 10^5Hz$. Table 6.1 presents the different concentrations and the lengths related to the diffusion, as well as PSF. As the third row shows, the gas is only restricted in the smallest cavity ($0.5mm$) practically for all mixtures. In low ^{3}He dilutions, edge enhancement is observed in cavities from 2 to 4 mm: rows 7, 8 and 9 (see also Fig.6.10). The other cavities were covered only by 2 pixels at the most and l_s/l_G values were to small to expect slow-exchange regime. Due to the large acquisition time, PSF is not high enough to prevent edge enhancement effects and take advantage of the gas admixture in these cavities.

The importance of edge enhancement is shown in Fig.6.8. It represents the signal per pixel in each mixture, i.e. in each image. All images show a decay of signal as the cavity size increases. The first point, cavity of $0.75mm$, shows a small value due to the lack of spins and to the faster signal decay because of collisions. The larger the N_2 concentration the smaller the signal decay for the different cavity sizes.

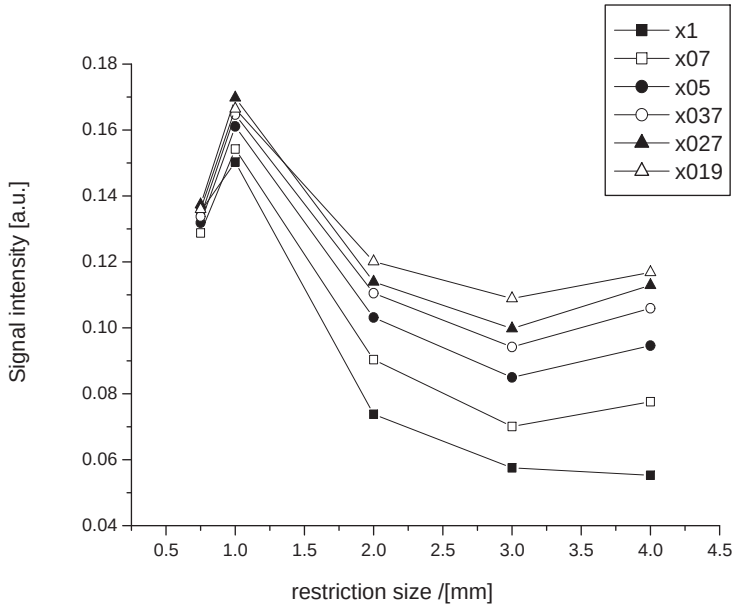

Figure 6.8: Signal per pixel of data of Tab.6.1 versus restrictive cavity sizes for different concentrations: x1, x07, x05 ... corresponds respectively to the following concentrations $x = 1$, $x = 0.7$, $x = 0.5$, ... and so on. The less ^{3}He in the mixture the higher the signal, especially in the larger cavities.

Figure 6.9 shows the normalized signal per pixel dependence with the concentration for the different cavity sizes. In the small cavities, the more N_2 in the mixture the less the signal. The gas in these cavities was in majority restricted and motional narrowing effects are expected. In fact, the presence of a BG moves away from the fast-exchange regime. In the case of big cavities, the increase of the *PSF* plays an important role since the gas is rather free. A win up to 2 times of the normalized signal can be observed. The figure also shows a gap between small cavities ($0.5,\ 0.75,\ 1\ mm$) and large cavities ($2,\ 3,\ 4\ mm$). The three big ones are exactly those where edge enhancement was observed, see Fig.6.10.

A concrete mixture, $x = 0.37$, can be studied in Fig.6.10. Two images are shown; one at $x = 1$, blue line, and the other at $x = 0.37$, red line. The black line denotes the signal win due to the admixture in the restricted walls. It can be observed that the three smallest cavities have practically no signal win, the other three cavities have a signal win but inhomogeneously, principally far away from the walls.

- Short acquisition time

The other set of images was acquired with a $G_{read} = 74 mT/m$ and $SW = 2 \cdot 10^5 Hz$,

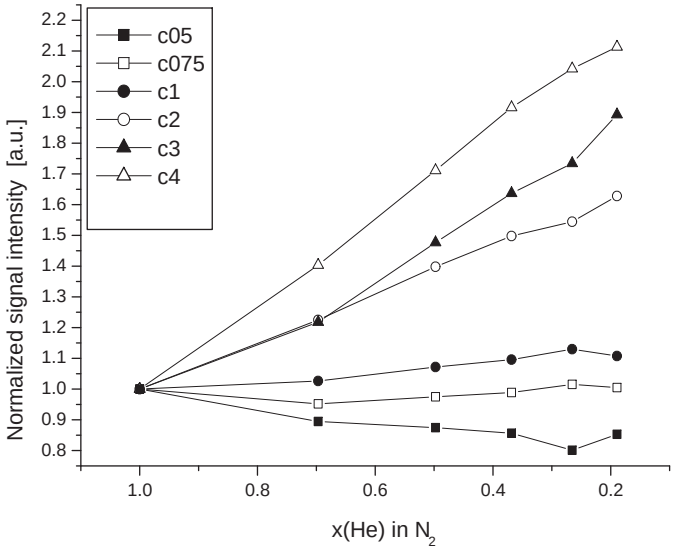

Figure 6.9: Signal per pixel of data of Tab.6.1 normalized to $x = 1$ upon concentrations for the different cavities: c05, c075, c1 ... corresponds respectively to the following cavity sizes $0.5mm$, $0.75mm$, $1mm$, ... and so on. Due to the admixture, the signal win is clearly appreciable for the three largest cavities.

what means the half of acquisition time of the previous set of images. As can be observed in the second row of Tab.6.2, due to this short time the values of the *PSF* are much higher compared with those of Tab.6.1 even though the gradient strength was doubled, since the time increases to cube and the gradient to square. In this set of images the gas was only restricted before mixing and only in the smallest cavity. Values of l_s/l_G are closer to 20 than those of Tab.6.1, nevertheless the higher values of the *PSF* minimize the edge enhancement effects, as already explained in reference to Fig.6.4, which in fact shows the $3mm$ slab images of this set.

Figure 6.11 shows the signal per pixel in the cavities at different concentrations. In this case, contrary to Fig.6.8, the signal does not decay for all mixtures when the cavity size increases. High N_2 concentrations enhance the signal by slowing down the gas diffusivity, specially in the low ^{3}He concentrations, because of the *PSF* increase, as can be observed in the second row of Tab.6.2. The signal loss is for low N_2 concentrations not as acute as in Fig.6.8.

In the case of the normalized signal of Fig.6.12, due to the high values of the *PSF*, the edge enhancement is only observed in the $4mm$ slab (see Fig.6.13) and the gap between large and small cavities is not as clear as in fig 6.9. Therefore the signal

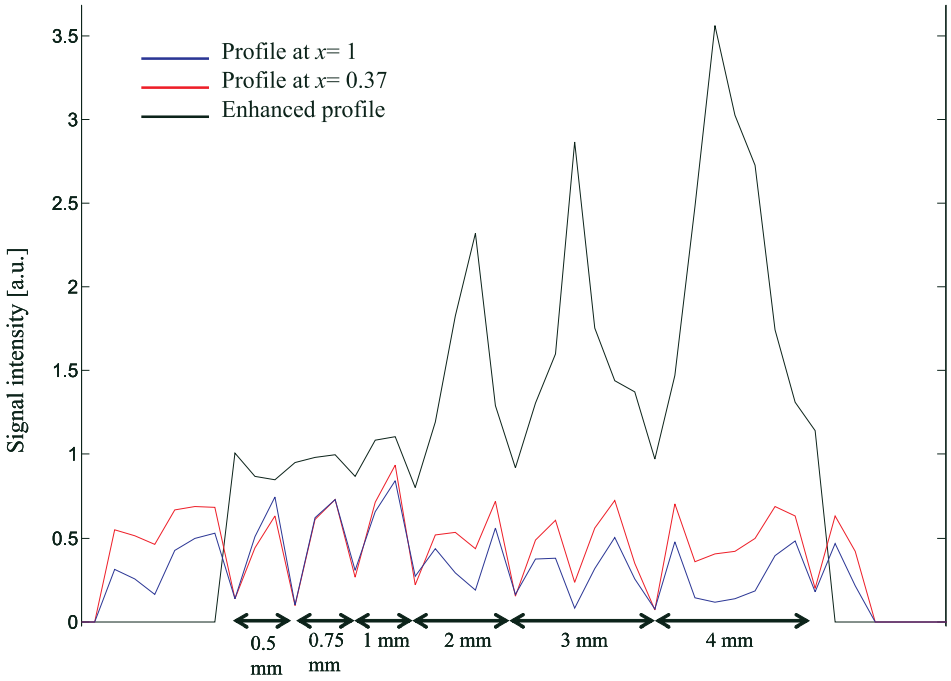

Figure 6.10: One-dimensional images of data from Tab.6.1. The blue line corresponds to the $x = 1$ image, the red line to the $x = 0.37$ and the black line is the proportion between both. The ratio was only calculated in the part between walls. An enhance of the the three largest cavities is observed, especially far away from the walls.

$x(^3\text{He})$ in N_2	1	0.71	0.50	0.36	0.26	0.19	0.14
PSF	0.001	0.005	0.012	0.018	0.024	0.028	0.032
$\Delta r/[mm]$	0.48	0.41	0.38	0.36	0.35	0.34	0.33
$l_s(0.5mm)/l_G$	2.19	2.42	2.57	2.66	2.72	2.76	2.79
$l_s(0.75mm)/l_G$	3.28	3.64	3.86	4.00	4.08	4.15	4.19
$l_s(1mm)/l_G$	4.37	4.86	5.14	5.32	5.44	5.53	5.59
$l_s(2mm)/l_G$	8.76	9.71	10.3	10.6	10.9	11.1	11.2
$l_s(3mm)/l_G$	13.1	14.6	15.4	16.0	16.3	16.6	16.8
$l_s(4mm)/l_G$	17.5	19.4	20.6	21.3	21.8	22.1	22.4

Table 6.2: Parameters of a one-dimensional images of phantom of Fig.6.7 at different concentrations of ^{3}He with N_2 ($G_{read} = 74mT/m$ and $SW = 2 \cdot 10^5 Hz$). The first row are the concentrations at which the images were acquired. The second row are the PSF values which attenuate the signal by non restricted diffusion. Third row is root mean square displacement given by Eq.6.4. Rows $4th$ to $9th$ are the l_s/l_G values (which define the fast-exchange regime, $l_s/l_G \approx 2$, to slow-exchange regime, $l_s/l_G \approx 20$) corresponding to the restrictive sizes.

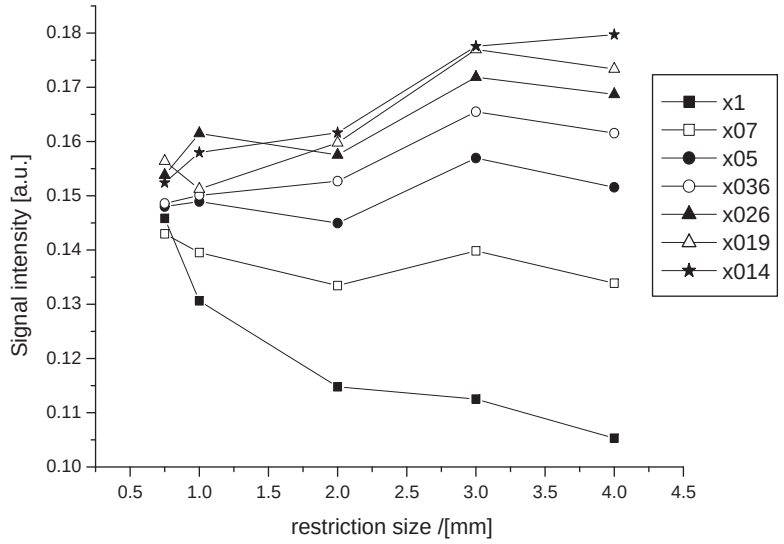

Figure 6.11: Signal per pixel of data of Tab.6.2 versus restrictive cavity sizes for different concentrations: x1, x07, x05 ... corresponds respectively to the following concentrations $x = 1$, $x = 0.7$, $x = 0.5$ ... and so on. For $x > 0.5$ the large cavities are affected by edge enhancement and signal decreases for larger sizes. For $x \leq 0.5$ wall collisions and lack of ^{3}He are more important than edge enhancement and the signal increases principally in the larger slabs.

win is not so appreciable. However, a signal rise is observed even in the $0.75mm$ cavity; in other words, more cavity sizes benefit from gas admixture for these sequence parameters.

Figure 6.13 shows the one-dimensional image of the phantom at $x = 1$, in blue, and $x = 0.36$, in red. The signal enhance is depicted in black only for the cavities. It can be observed that the $4mm$ slab is for both concentrations, red and blue lines, affected by edge enhancement. In the $3mm$ slab, this effect is suppressed by the *PSF* increase, as can be seen also in Fig.6.4. Signal enhance, black line, in the $3mm$ and $2mm$ cavities is more homogeneous if it is compared with the pixel intensity distribution of the $4mm$ one or those of Fig.6.10.

6.6.2 Buffer gas dependence

Another method to obtain the desired D, and so enhance different cavity sizes at will, is the choose of different buffer gases, BG, as can be observed in Fig.5.2. For a more

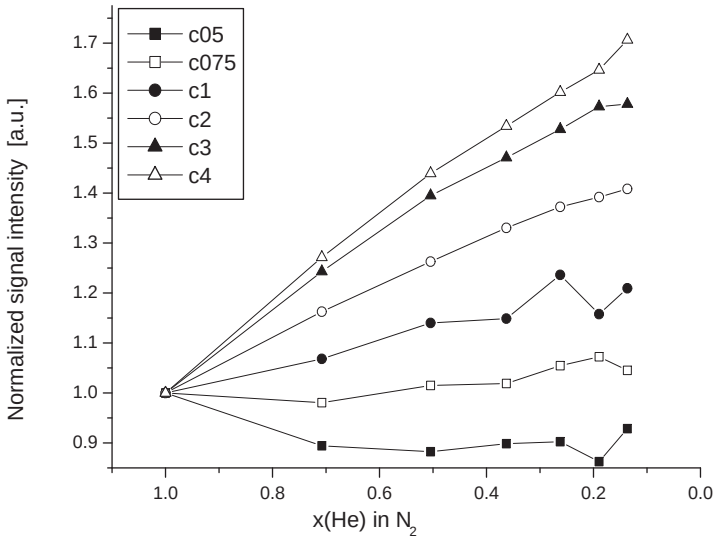

Figure 6.12: Signal per pixel of data of Tab.6.2 normalized to $x = 1$ upon concentrations for the different cavities: c05, c075, c1 ... corresponds respectively to the following cavity sizes $0.5mm$, $0.75mm$, $1mm$ ... and so on. Due to the admixture, the signal win is appreciable for almost all cavity sizes.

realistic demonstration of the applicability of such buffer gases as structural contrast agents, a ventilated lung of a dead pig was imaged using mixtures of laser polarized ^{3}He with the buffer gases ^{4}He, N_2 and SF_6 (molar fractions, $x \approx 0.08$, assuming a total lung volume of $2L$) [Acos06b]. Special care was taken to replace all residual gases from previous experiments by extensive ventilation cycles. In order to quantify to some extent the contrast due to changes in the b-value for the three buffer gases, an additional bipolar gradient in the sagittal direction (blue gradient in Fig.6.14) was added to the otherwise unchanged pulse sequence of Fig.6.14.

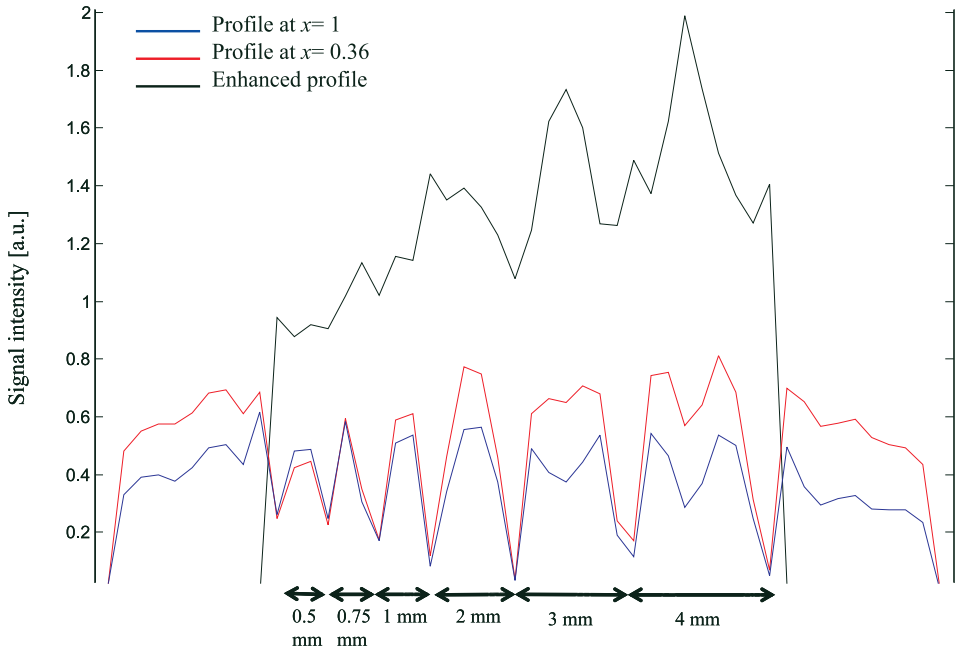

Figure 6.13: One-dimensional images of data from Tab.6.2. The blue line corresponds to the $x = 1$ image, the red line to the $x = 0.36$ and the black line is the proportion between both. The ratio was only calculated in the part between walls. An enhance of the three largest cavities is observed.

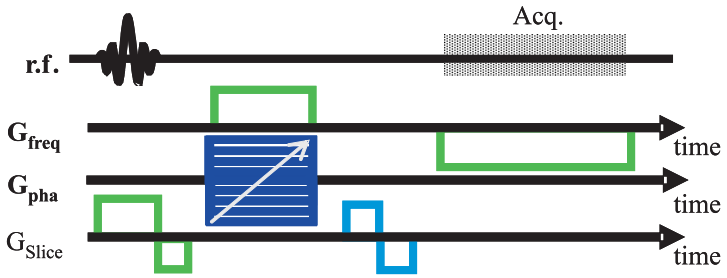

Figure 6.14: Diffusion weighted image sequence with slice selection used for the lung images of Fig.6.15. Five slices of $2cm$ thickness were acquired with the following parameters: tip angle $\backsim 6°$, echo time $= 6ms$, repeat time $= 16.1ms$, and $FOV = 32cm$; a 64×128 (phase $\times$ read) data matrix was acquired in one scan.

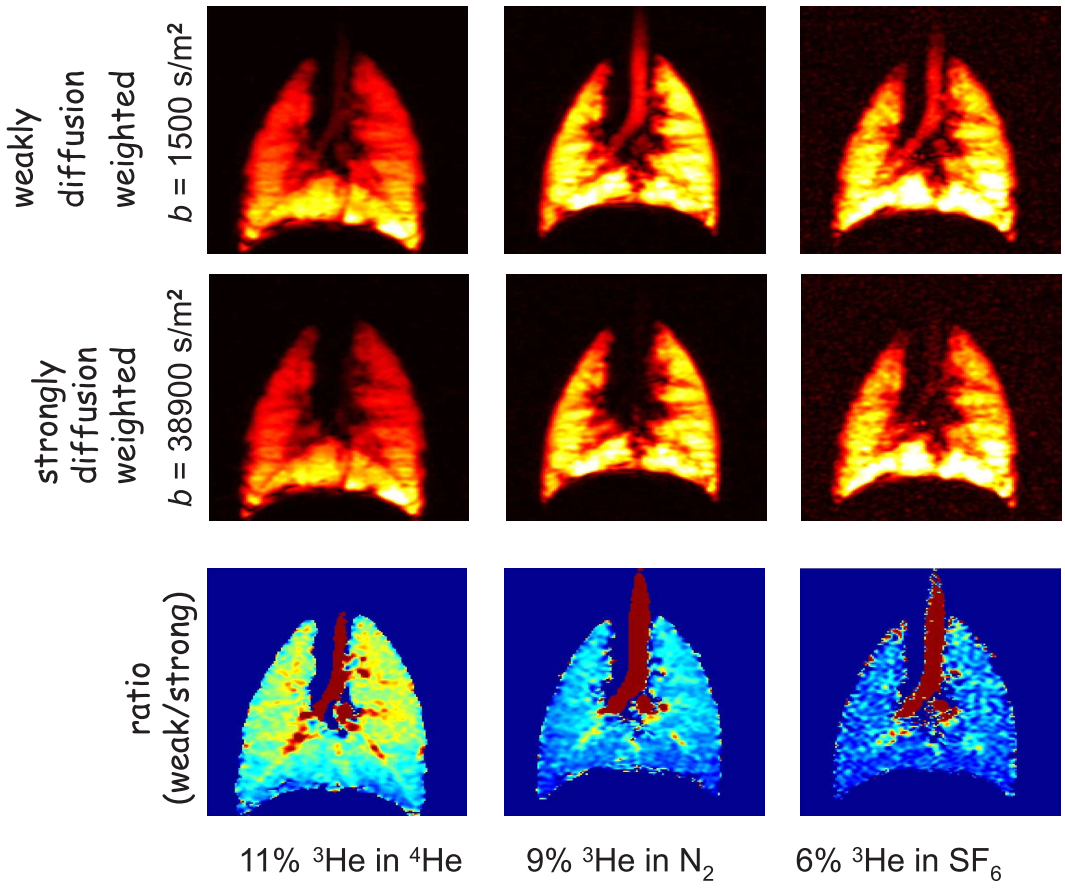

Figure 6.15: ^{3}He images of a pig lung using different buffer gases: ^{4}He (left column), N_2 (middle column), and SF_6 (right column). The top row shows the images of a reference measurement without additional diffusion gradients and $b = 1525 s/m^2$ along the vertical read direction. The color scale stretches from 0% to 90% of the maximal intensity of each image. The middle row shows the images with additional diffusion gradients and $b = 38897 s/m^2$ in the sagittal direction (normal to image plane). The bottom row shows the images of the top row divided by strongly diffusion weighted images of the middle row. Note that the colour scales for the ratio images in this row stretches from ratio 1 to 2. Noise was masked by applying a suitable threshold filter.

Lung images of the porcine lung were acquired (see Fig.6.15) using a whole body magnet with a field strength of $1.5T$ (Siemens Magnetom Vision; Siemens Medical Solutions, Erlangen, Germany). A custom-built chest coil (Fraunhofer Institute, St. Ingbert, Germany) was used for r.f. transmission and reception. The coil design comprised of a dual-ring construction with a sensitive volume of $450 \times 365 \times 340 mm^3 (L \times W \times H)$. It was manually tuned to the ^{3}He Larmor frequency at $48.4 MHz$. A slice-selective gradient echo sequence (see Fig.6.14), with additional gradient weighting,

was used with the *b*-values given in the figure caption (see Fig.6.15). Five slices of $2cm$ thickness were acquired with the following parameters: tip angle $\backsim 6^\circ$, echo time $= 6ms$, repeat time $= 16.1ms$, and $FOV = 32cm$; a 64×128 (phase $\times$ read) data matrix was acquired in one scan. This measurements were performed at the clinic's university of Mainz (work group Prf.Schreiber).

With approval of the animal care committee, a domestic pig (mass $\backsim 20kg$) was anesthetized and a tracheal tube was inserted. To avoid asphyxia during the experiment, the anesthetized animal was killed by a potassium overdose. Then the lungs were flushed with pure nitrogen for about 15 minutes using a servo ventilator 900C (Siemens-Elema) with a tidal volume of $400mL$ and a respiratory frequency of 40 cycles per minute using volume controlled ventilation. At 45 minutes after death, the first set of images (Fig.6.15 middle column) was acquired after applying a ^{3}He-bolus of $178mL$ $(x = 0.089)$. The flushing was repeated to replace N_2 with ^{4}He and imaged 2.5 hours postmortem with a ^{3}He bolus of $210mL$ $(x = 0.105)$ (Fig.6.15 left column). Finally the helium was replaced by SF_6 and the right column of Fig.6.15 was acquired with a ^{3}He bolus of only $112mL$ $(x = 0.056)$ five hours after death.

The results of this procedure can be seen in Fig.6.15. The experiments on the top row were acquired without an additional diffusion gradient (blue gradient off in Fig.6.14). On the middle row, the diffusion gradient was turned on decreasing the signal in the larger air spaces. The bottom row of Fig.6.15 shows a ratio image of weakly divided by the strongly diffusion-weighted experiments. Of course the signal ratio is highest for the large airspaces (such as the trachea). However, this ratio decreases with going from ^{4}He (bottom left) to SF_6 (bottom right), because the diffusion is slowed more effectively by the heavier buffer gas. These ratio images also clearly reveal that similar processes can be observed in the somewhat smaller airspaces up to segmental bronchi, which becomes clearly visible in the bottom left image, obtaining the highest contrast in the ratio images. On the other extreme the bottom right image reaches noise level.

6.7 Conclusions

The possibility to enhance the MRI-signal significantly by diluting the detected gas by inert buffer gases of high molecular weight is clearly demonstrated. Of course, higher signals are observed for lower *b*-values. However, considerations of the nature and concentration of the gas mixture are of importance when either *b* or *x* is predefined by the application. The somewhat "paradoxical" case, that less signal-carrier can result in higher signal intensity, is illustrated in Fig.6.2. Nonetheless, one should note, that

this description and observation is essentially valid for unrestricted diffusion, which might be interesting for imaging larger cavities in the body (i.e., trachea, bronchi, and sinus). Another possible area of practical implementation includes strongly diffusion weighted sequences or "microscopic" MRI. However, the smaller structures of the respiratory system are usually first affected by pulmonary diseases. Hence, restricted diffusion appears to be more relevant for most clinical applications.

In order to investigate the restricted geometries, two phantoms with different cavities sizes have been used to study the influence of sequence parameters and control of D. One, consisting on collinear cylinders of different radii, shows that diffusion effects, as motional narrowing and edge enhancement, cause image distortions for the high diffusive ^{3}He. Gas admixture and pressure increase, reduces these effects otherwise practically impossible to cut out in all cavity sizes just by sequence parameter corrections. The BG admixture provides a reduction of the D homogeneously inside the sample. The D effects on images do not depend any more on the restriction cavity but on the admixture: concentration and BG. The best example is the "g)" image of Fig.6.6. With a $\Delta r \approx 0.2mm$ in the whole image, the set of cylinders on the left of the image can be distinguished with a constant intensity, which is very close to the largest cylinder on the top of the image. Even though in this image a wide spectra of values of l_s/l_G –form 3.34 for the $0.5mm$ of diameter capillary to 21 for the $3.2mm$ capillary– the attenuation of diffusion coefficient reduce the observed effects of slow and fast exchange regimes.

Another phantom was constructed to study one-dimensional images in read gradient direction. It consists of parallel planes placed at different distances, see Fig.6.7. Two sets of images at different concentrations were done, differentiated by the read gradient intensity and spectral width, SW. The shortest SW implies more acquisition time, and hence diffusion effects play an important role in the acquired image, as in the previous phantom. However, if two images with different admixture are compared, the diffusion coefficient change, due to the admixture, emphasize the signal in the larger slabs (see Fig.6.10). Nevertheless the enhancement is achieved specially in the middle of the larger cavities, since the borders were already restricted. This difference is less appreciable in the set of images taken with the larger SW (see Fig.6.13). In this case, the drawback is that the signal enhance in the large slabs is not so substantial.

These two phantoms offer an approximation of a realistic application in lung medicine due to the wide distribution of cavity sizes. However, some idealizations have been done: the most important gas, Oxygen, was not used due to the depolarizing effects (see section 2.3.1), and in the case of the admixture of the collinear cylinders, the gas admixture was pressed at $2bar$. An approach to a more realistic experiment

with the lung of a dead pig shows other methods to control the D and highlight cavity sizes by means of diffusion weighted images. The combination of light and heavy BG permits also to obtain a desired D. Buffer gases with low molecular mass (such as ^{4}He) can be used to keep the diffusion coefficient high in a gas mixture, or in the case of hyperpolarized ^{129}Xe even increase it. On the other hand, gases with high molecular mass (such as SF_6) can be used in the opposite fashion.

Differences in the inhaled gas mixture can cause significant changes of the image contrast for suitably chosen b-values. While mixtures with high diffusion coefficients can be used to suppress the larger airways, a less diffusion weighted image can be obtained for the mixtures with low diffusion. While an individually optimized mixture of the breathing gas might be impractical for clinical MRI, these two described scenarios might have an assistive influence on the choice of roughly adjusted gas mixtures, depending on the type of experiment to follow. For instance, experiments which locally determine the ADC [Schr99] or the partial oxygen pressure [Lehm04] of very light gases or high ^{3}He concentration can profit from a lower D, because it could make the experiment more reliable and faster due to improved SNR. Furthermore, this approach could assist or replace acquisition schemes that minimize the influence of diffusion on the NMR signal. However, the opposite approach seems to have more importance, as an increase of the diffusion coefficient will allow the tailoring of the image contrast to originate mainly from structures below an adjustable size. If this size threshold is known, the pixel size can be increased, because a visual selection of regions of interest excluding larger bronchi is no longer necessary. At this reduced resolution, however, the signal will increase, which can then be used to reduce the measurement time.

Chapter 7

Conclusions

The high diffusivity of gases strongly influences the NMR signal intensity, hence the resolution and appearance of the images. Furthermore, due to the large polarization achieved, 64% for ^{129}Xe [Ruse06] and 91% for ^{3}He [Wolf04], the hydrodynamic equations of a diluted spin polarized gas predicts unusual effects. These predictions and the influence and control of gas diffusion have been investigated in this work aiming to MRI applicability.

In a comprehensive review, Lhuillier and Laloë [Lhui82b] approximate a solution of the Boltzmann transport equation and conclude that there is a dependence of the spin current on the magnetization, which can affect translational motion like diffusion. Since it could in principle alter the D measurements and MRI signal, a rigorous study of the D upon polarization was carried out. The D_{Xe} and D_{He} at different polarizations and 1*bar* at room temperature was measured *in vitro*. No dependence of D on the polarization was found, however, only a small decay of the measured values is observed in the low polarization regime, which is well explicated due to temperature changes and gradient overheating.

Another method is presented to depolarize the gas by means of admixture of laser polarized ^{3}He with thermal polarized ^{3}He. The diffusion coefficient of ^{3}He was measured at different pressures in order to achieve different collision rates and therefore different spin transition probabilities. After normalization of D, no deviation in the measured values has been observed, meaning that under more restricted movement conditions –such as capillaries, alveoli or buffer gas– no spin diffusion effects can be expected.

Since the experiments done *in vitro*, which are more sensitive than an usual clinical MRI, do not show any divergence in D, it can be conclude that spin diffusion, if it occurs under clinical conditions, has no observable effect in the particle diffusion

measurements by NMR.

The novel experimental setup and protocol to depolarize by admixture, can also be used to achieve a controlled binary gas mixture at pressures from $0.1bar$ to $2bar$. The gas mixing setup enables a synchronized timing with the pulse sequences and complete automation of the experiment. The molar fraction determination is performed by the NMR signal intensity. This strategy turned out to be more accurate than other standard techniques for quantitative analysis of mixtures of gases with very different molar masses. This setup was then used for the measurement of the diffusion coefficient of ^{3}He in binary mixtures with other three different inert buffer gases (^{4}He, N_2 and SF_6) as well as ^{129}Xe diffusion coefficient as a function of its molecular fraction upon a mixture with N_2. The simultaneous measurement of the diffusion coefficient of ^{3}He and ^{129}Xe as a function of the Xe molar fraction has been also presented.

The agreement between the experimentally measured diffusion coefficients with those obtained from molecular dynamics simulations and analytical expressions is very good, in particular for ^{3}He. The reproducibility is demonstrated, that permits to achieve fine-tuning diffusion properties of a gas by the admixture of another one of different molecular mass.

Diffusion is one of the most important parameters in porous media research, which can be improved with this new technique. In case of MRI, the control of the diffusion coefficient is important for spatial resolution of the signal, since diffusion influences the NMR signal by means of the point spread function (*PSF*). Reducing the diffusion coefficient is hence important for minimizing *PSF* effects and thus the spatial resolution.

The improvment of MRI signal by diluting the detected gas by inert buffer gases of high molecular weight is clearly demonstrated. Considerations of the nature and concentration of the gas mixture are of importance when the sequence parameters, summarized in b[1], are predefined by the application. The somewhat "paradoxical" case, that less signal-carrier can result in higher signal intensity is demonstrated, showing that the signal of diluted ^{3}He with SF_6 exhibits 5 times of the expected signal in the optimal concentration, x_{opt}. Larger signal enhancement has been observed for other b-values.

As conceptually discussed, the influence of diffusive processes during the image acquisition can be understood by a *PSF*, whose amplitude is determined by the competition of a coherent and incoherent term. The coherent term arises from the spatial displacement of the signal by the application of gradients, which determines the image resolution, while the incoherent diffusive spread of particles destroys the underlying

[1] $b = \gamma^2 G^2 D[\delta^2(\Delta - \delta/3) + \varepsilon^3/30 - \delta\varepsilon^2/6]$ for parameters depicted in Fig.2.12

phase coherence resulting in a signal loss. However, this is only valid as long as free and unrestricted diffusion is considered. In real samples (e.g. lungs) the free path a particle moves can also be determined by the size of its container, when it is observed long enough. This latter case of restricted diffusion will therefore cause smaller "apparent" diffusion coefficients (ADC) for small voids. MRI of restricted geometries presents effects related to two characteristic lengths: the cavity size l_s and a dephasing length $l_G = \sqrt[3]{\frac{D}{\gamma G}}$. The ratio l_s/l_G defines the regimes in which "edge enhancement" or "motional narrowing" affects the images.

The influence of the diffusion in images of restricted geometries is clearly attenuated by gas admixture. In a sample consisting on parallel collinear cylinders of different diameter, the "edge enhancement" and "motional narrowing" effects can be avoided under different experimental settings (acquisition points and sequence timing), achieving an homogeneous signal intensity distribution for all cavities independently of their size, i.e. l_s.

The diffusion effects can also be manipulated to enhance cavity sizes by two methods based on D control; by means of concentration control of the gas admixture or choice of buffer gas (BG). To investigate the first method, two sets of images at different concentrations have been presented, differentiated by the read gradient intensity and spectral width, SW, but with the same field of view. If two images with different concentrations are compared, the diffusion coefficient changes, due to the admixture, emphasizing the signal in the larger slabs. Nevertheless, enhancement is achieved especially in the middle of the larger cavities, since the borders were already restricted before admixture. This difference is less appreciable in the set of images taken with the larger SW. In this case, the drawback is that the signal win is not so substantial.

The second method, diffusion control by means of BG choice, has been presented in diffusion weighted images (DWI) of a pig lung. Buffer gases with low molecular mass (such as ^{4}He) can be used to keep the diffusion coefficient high in a gas mixture, or in the case of hyperpolarized ^{129}Xe even increase it. On the other hand, gases with high molecular mass (such as SF_6) can be used in the opposite fashion. While mixtures with high diffusion coefficients can be used to suppress the larger airways, a less diffusion-weighted image can be obtained for the mixtures with low diffusion. Of course, the binary mixtures used in this study have to become ternary for in vivo investigations, including sufficient oxygen.

It is easy to foresee that these results can have a considerable impact on clinical lung studies. Obviously, the combination of these two methods –concentration and buffer gas choice– is not excluded. It is possible to create such gas mixtures that only the alveoli become visible or the entire air spaces. Furthermore, diffusion measure-

ments of gases in lungs with the aim to study the underlying microstructure will also profit from these results.

The experiments of this work had been mainly directed to applicability in clinical MRI, nevertheless the results can be used generally in porous media research. Exploiting the control of the diffusion coefficient by this novel method opens new possibilities in the field of NMR of gases, not only for laser polarized, but also for thermal polarized systems.

Bibliography

[Acos06] R.H.Acosta, P.Blümler, L.Agulles-Pedrós, S.Komin, D.Sebastiani, H.W.Spiess “Diffusion in binary gas mixtures studied by NMR of hyperpolarized gases and molecular dynamics simulations” Physical Chemistry Chemical Physics 8 4182-4188 (2006)

[Acos06b] R.H.Acosta, P.Blümler, L.Agulles-Pedrós, A.E.Morbach, J.Schmiedeskamp, A.Herweling, U.Wolf, A.Scholz, W.G. Schreiber, W.Heil, M.Thelen, H.W.Spiess “Controlling Diffusion of ^{3}He by Buffer Gases: A Structural Contrast Agent in Lung MRI” Journal of Magnetic Resonance Imaging 24 1291-1297 (2006)

[Albe94] M.S.Albert, G. D.Cates, B.Driehuys, W.Happer, B.Saam, C.S.Springer, A.Wishnia “Biological magnetic resonance imaging using laser-polarized ^{129}Xe” Nature 370 199-201 (1994)

[Appe98] S.Appelt, A.B.Baranga, C.J.Erickson, M.V.Romalis, A.R.Young, W.Happer “Theory of spin-exchange optical pumping of ^{3}He and ^{129}Xe” Physical Review A 58(2) 1412 (1998)

[Appe00] N.J.Shah, T.Ünlü, H.P.Wegner, H.Halling, K.Zilles, S.Appelt “Measurement of rubidium and xenon absolute polarization at high temperatures as a means of improved production of hyperpolarized 129Xe” NMR Biomedicine 13 214-219 (2000)

[Appe04] S.Appelt “From Photon Spin to Magnetic Resonance Imaging” Habilitation RWTH Aachen 2004

[Atk84] P.W.Atkins, Physical Chemistry, Oxford University Press, 1984

[Beck98] J.Becker, J.Bermuth, M.Ebert, T.Grossmann, W.Heil, D.Hoffmann, H.Humblot,M.Leduc, E.W.Otten, D.Rohe, R.Surkau “Interdisciplinary experi-

ments with polarized ^{3}He"Nuclear Instruments and Methods in Physics Research A 402 327-336 (1998)

[Blüm94] P.Blümler, B.Blümich "NMR Imaging of Solids" NMR-Basic Principles and Progress Vol. 30 209 (1994)

[Blüm04] P. Blümler, H. Raich "Design and Construction of a Dipolar Halbach Array with an Homogeneous Field from $N \times 8$ Identical Bar-Magnets–NMR-Mandhalas" Concepts on Magnetic Resonance B : Magn. Reson. Eng. 23B(1) 16-25 (2004)

[Bouc60] M.A.Bouchiat, T.R.Carver, C.M.Varnum "Nuclear polarization of ^{3}He gas induced by optical pumping and dipolar exchange" Physical Review Letters 5 373-375 (1960)

[Brow79] K.R.Brownstein, C.E.Tarr "Importance of classical diffusion in NMR studies of water in biological cells" Physical Review A 19 2446-2453 (1979)

[Call91] P.T. Callaghan "Principles of Nuclear Magnetic Resonance Microscopy" Oxford Science Publication, 1991

[Cate88] C.D.Cates, D.J.White, Tind-Ray Chien, S.R.Schaefer, W.Happer "Spin relaxation in gases due to inhomogeneous static and oscillating magnetic fields" Physical Review 38 5092-5106 (1988)

[Cha70] S.Chapman, T.G.Cowling "The mathematical theory of non-uniform gases" 3rd Ed. Cambridge university press, 1970

[Chan02] B.Chann, I.A.Nelson, L.W.Aanderson, B.Driehuys, T.G.Walker "^{129}Xe–Xe molecular spin relaxation" Physical Review Letters 88 113201 (2002)

[Char92] C.Chardairerivere, J.C.Roussel "Principles and Potential of NMR Applied to the Study of Fluids in Porous Media" Revue de L'Insitut Francais du Petrol 47 4 503 (1992)

[Chen99] X.J.Chen, H.E.Möller, M.S.Chawla, G.P.Cofer, B.Driehuys, L.W.Hedlund, G.A.Johnson "Spatially Resolved Measurements of Hyperpolarized Gas Properties in the Lung In Vivo. Part I: Diffusion Coefficient" Magnetic Resonance Medicine 42 721-728 (1999)

[Cole63] F.D.Colegrove, L.D.Schearer, G.K.Walters "Polarization of ^{3}He gas by optical pumping" Physics Review A 132 2561-2572 (1963)

[Conr06] M.C.Conradi, B.TSaam, D.A.Yoblonskiy, J.C.Woods “Hyperpolarized ^{3}He and perfluorcarbon gas diffusion MRI of lungs” Progress in Nuclear Magnetic Resonance Spectroscopy 48 63-83 (2006)

[Cus03] E.L.Cussler “Diffusion mass transfer in fluid systems” 2nd Ed. Cambridge University press, 2003.

[Drie95] B.Driehuys, G.D.Cates, W.Happer “Surface relaxation mechanisms of laser-polarized ^{129}Xe Physical Review Letters 74 4943-4946 (1995)

[Eber96] M.Ebert, et alter “Nuclear Magnetic Resonance with hyperpolarised Helium-3” The Lancet 347 1297-1299 (1996)

[Eins05] A.Einstein. “Über die von der molekularkinetischen Theorie der Wärme geforderten Bewegung von in ruhenden Flüssigkeiten suspendierten Teilchen” Annalen der Physik 17 549-560 (1905)

[Emer63] V.J.Emery “Spin Diffusion in Gases at Low Temperatures” Physical Review 133:3A A661-A664 (1963)

[Ens22] D. Enskog, Archiv. för Mathematik, Astronomi och Fysik, 1922

[Erns87] R.R.Ernst, G.Bodenhausen, A.Wokaun “Principles of Nuclear Magnetic Resonance in One and Two Dimensions” Clarendon Press, Oxford 1987

[Fitz69] W.A.Fitzssimmons, L.L.Tankersley, G.K.Walters “Nature of surfaceinduced nuclear-spin relaxation of gaseous He3” Physical Review 179 156-165 (1969)

[Gamb65] R.L.Gamblin, T.R.Carver “Polarization and relaxation processes in ^{3}He gas” Physics Review 138 A 946-960 (1965)

[Glad94] L.F.Gladden “Nuclear Magnetic Resonance in Chemical Engineering - Principles and Applications” Chemical Engineering Sciencie 49 3339 (1994)

[Good02] B.M.Goodson “ Nuclear Magnetic Resonance of Laser-Polarized Noble Gases in Molecules, Materials, and Organisms” Journal of Magnetic Resonance 155 157-216 (2002)

[Gros00] T.Großmann “Realisierung des ^{3}He Kreislaufs zur ^{3}He Magnet Resonanz-Tomographie” Ph.D Thesis in the the Johannes Gutenberg-Universität Mainz, Germany 2000

[Haac99] E.M.Haacke, R.W.Brown, M.R.Thompson, R.Venkatesan “Magnetic Resonance Imaging, physical principles and sequence design” Wiley-liss 1999

[Haas86] A.Haase, J.Frahm, D.Matthaei, W.Hanicke, K.D.Merboldt “FLASH imaging: Rapid NMR imaging using low flip-angle pulses” Journal of Magnetic Resonance 67 258-266 (1986)

[Hahn50] L.E.Hahn “Spin Echoes” Physical Review 80 580-594 (1950)

[Heil96] M-Ebert, T.Großmann, W.Heil, E.W.Otten, R.Surkau,M.Leduc,P.Bachert, M.V.Knopp, L.R.Schad, M.Thelen “Nuclear Magnetic Resonance with hyperpolarised Helium-3” The Lancet,347 1297-1299 (1996)

[Heil97] E.Wilms, M.Ebert, W.Heil, R.Surkau “Polarimetry on dense samples of spin-polarized 3He by magnetostatic detection” Nuc.Instr.Meth in Physics Research A 401 491-498 (1997)

[Heil99] R.Surkau, A.Deninger, J.Bermuth, M.Ebert,T.Großmann,W.Heil,L.Lauer, E.Otten, J.Schmiedeskamp “ Highly polarized 3-He for lung imaging” Eur.Radiol.9:B15 (1999)

[Heil06] A.Deninger, W.Heil, E.W.Otten, M.Wolf, R.K.Kremer, A.Simon “Paramagnetic relaxation of spin polarized 3He at coated glass walls Part II ” The European Physical Journal D 38:3 439-443 (2006)

[Hieb06] S.Hiebel “ Methodische und technische Weiterentwicklung der ^{3}He-MRT im Hinblick auf erweiterte lungendiagnostische Anwendungsmöglichkeiten” Ph.D. Thesis in the department of physics at the Johannes Gutenberg-Universität Mainz, Germany 2006.

[Hirs65] J.O.Hirschfelder, C.F.Curtis, R.B.Bird “ Molecular theory of gases and liquids ” John Wiley and sons, inc. 1965

[Hunt63] E.R.Hunt, H.Y.Carr “Nuclear magnetic resonance of ^{129}Xe in natural xenon” Physical Review 130 2302-2305 (1963)

[Jame88] C.J.Jameson, A.K.Jameson, J.K.Hwang “Nuclear spin relaxation by intermolecular magnetic dipole coupling in the gas phase ^{129}Xe in oxygen” Journal of Chemichal Physics 89 4074-4081 (1988)

[Jeon89] J.W.Jeon, W.J.Mullin “Transverse Spin Diffusion in Polarized Fermi Gases” Physical Review Letters,62:23 2691-2694 (1989)

[Jeon86] J.W.Jeon, W.J.Mullin “Theory of spin diffusion of Dilute, Polarized Fermions for all Temperatures” Journal of Low Temperature Physic 67:5/6 421-440 (1987)

[Kiha53] T.Kihara, “Imperfect gases” (Asakura bookstore, Tokyo, 1949) Mod. Rev. Physics 25 831 (1953)

[Laut73] P.C.Lauterbur “Image formation by induced local interactions: examples employing nuclear magnetic resonance” Nature 242:190 (1973)

[Laew01] J.C.Leawoods, D.A.Yablonskiy, B.Saam, D.S.Gierada, M.S.Conradi “Hyperpolarized ^{3}He Gas Production and MR Imaging of the Lung" Concepts Magnetic Resonance 13 277-293 (2001)

[Legg68] A.J.Legget, M.J.Rice “Spins Echoes in Liquid ^{3}He and Mixtures: a predicted new effect” 20:12 586-589 (1968)

[Legg70] A.J.Legget “Spin diffusion and spin echoes in liquid ^{3}He at low temperature” Journal of Physics C: Solid State Physics 3:2 448-459 (1970)

[Lehm04] F.Lehmann, B.Eberle, K.Markstaller et al. “Ein Auswerteprogramm zur quantitativen Analyse von Messungen des alveolaeren Sauerstoffpartialdrucks (pAO2) mit der sauerstoffsensitiven 3He-MRTomographie” Rofo 176 1399-1408 (2004)

[Levi01] M.H. Levitt “Spin Dynamics: basics of nuclear magnetic resonance” John Wiley & Sons, Ltd. 2001

[Lhui82a] C.Lhuillier, F.Laloë “ Transport properties in a spin polarized gas,I” Journal de Physique 43 197-224 (1982)

[Lhui82b] C.Lhuillier, F.Laloë “ Transport properties in a spin polarized gas,II” Journal de Physique 43 224-241 (1982)

[Lind01] E.Lindahl, B.Hess, D. v. d.Spoel “GROMACS 3.0: A package for molecular simulation and trajectory analysis” Journal Molecular Modeling 7 306-317 (2001)

[Mans73] P.Mansfield, P.K.Grannell “NMR ’diffraction’ in solids?” Journal of Physics C: Solid State Phys 6 L422-L426 (1973)

[Mair00] R.W.Mair,D.Hoffmann, S.A.Sheth, G.P.Wong, J.P.Butler, S.Patz, G.P.Topulos, R.L.Walsworth “Reduced xenon diffusion for quantitative lung study – the role of SF_6” NMR in Biomedicine 13 229-233 (2000)

[Mair02] R.W.Mair, P.N.Sen, M.D.Hürlimann, S.Patz, D.G.Cory, R.L.Walsworth “The Narrow Pulse Approximation and Long Length Scale Determination in Xenon Gas Diffusion NMR Studies of Model Porous Media” Journal of Magnetic Resonance 156 202-212 (2002)

[Miya83] K.Miyake, W.J.Mullin “Spin Diffusion in a Two-Dimensional Degenerate Fermi Liquid” Physical Review Letters, 50:3 197-200 (1983)

[Mühl07] Frank Mühlbauer “ Polarimetrie an hyperpolarisiertem 129-Xenon ” Diploma Thesis in the department of physics at the Johannes Gutenberg-Universität Mainz, february 2007.

[Mull83] K.Miyake, W.J.Mullin “Exact Transport Properties of Degenerate , Weakly Interacting and Spin-Polarized Fermions” Journal of Low Temperature Physic 53:3/4 313-338 (1983)

[Mull90] W.J.Mullin, F.Laloë, M.G.Richards “Longitudinal relaxation time for dilute quantum gases” Journal of Low Temperatures Physics 80 1-13 (1990)

[Newb93] N.R.Newsbury, A.S.Barton, G.D.Cates, W.Happer, H.Middleton “Gaseous ^{3}He–^{3}He magnetic dipolar spin relaxation” Physical Review A 48:6 4411-4420 (1993)

[Pric97] W.S.Price “Pulsed-Field Gradient Nuclear Magnetic Resonance as a Tool for Studying Translational Diffusion: Part 1. Basic Theory” Concepts Magnetic Resonanace 9 299-336 (1997)

[Raid87] R.C.Reid, J.M.Prausnitz, B.E.Poling “The Properties of Gases and Liquids” McGraw-Hill Book Company, New York, 4th edn, (1987)

[Rizi05] R.R.Rizi et alter “Imaging physiological parameters with hyperpolarized gas MRI” Progress in Nuclear Magnetic Resonance Spectroscopy 47 187-212 (2005)

[Ross69] K. Rossmann “ Point spread-function, line spread-function, and modulation transfer function: tools for the study of imaging systems” Radiology 93 257-272 (1969)

[Ruse06] I.C.Ruset, S.Ketel, F.W.Hersman “Optical Pumping System Design for Large Production of Hyperpolarized ^{129}Xe” Physical Review Letters96, 053002(1-4) (2006)

[Ruth99] U.Ruth, T.Hof, J.Schmidt, D.Fick, H.J.Jänsch “Production of nitrogen-free, hyperpolarized 129Xe gas” Applied Physics B 68 93-97 (1999)

[Saam95] B.Saam, W.Happer, H.Middleton “Nuclear relaxation of ^{3}He in the presence of O_2” Physical Review A 52 862-865 (1995)

[Saam96] B.Saam, N.Drukker, W.Happer “Edge enhancement observed with hyperpolarized ^{3}He” Chemical Physics Letters 263 481-487 (1996)

[Sche65] L.D.Schearer, G.K.Walters “Nuclear spin-lattice relaxation in the presence of magnetic field gradients” Physical Review 139 A 1398-1402 (1965)

[Schm04] J.Schmiedeskamp “Weiterentwicklung einer Produktionsanlage und der Speicherungs- bzw. Transportkonzepte für hochpolarisiertes ^{3}He - Anwendungen in Kernspintomographie und physikalischer Grundlagenforschung ” Ph.D. Thesis in the department of physics at the Johannes Gutenberg-Universität Mainz, Germany 2004

[Schm06] J. Schmiedeskamp et al. “Paramagnetic Relaxation of Spin Polarized 3He at Bare Glass Surfaces Part I ” The European Physical Journal D 38:3 427-438 (2006)

[Schm06b] J.Schmiedeskamp, H.J.Elmers, W.Heil, E.W.Otten, Yu.Sobolev, W.Kilian, H.Rinneberg, T.Sander-Thömmes, F.Seifert,J.Zimmer “Relaxation of spin polarized 3He by ferromagnetic particles part III” European Physical Journal D 38:3 445-454 (2006)

[Schr99] W.G.Schreiber, K.Markstaller, B.Eberle, et al. “Ultrafast MR-imaging of 3-dimensional distribution of hyperpolarized helium-3 diffusion coefficients in the lung” Eur Radiol 9 542 (1999)

[Sen04] P.N.Sen “Time-Dependent Diffusion Coefficient as a Probe of the Geometry” Concepts in Magnetic Resonance Part A, 23A(1) 1-21 (2004)

[Smol06] M. von Smoluchowski “Zur kinetischen Therie der Brownschen Molekularbewegung und der Suspension” Annalen der Physik 326(14) 756-780 (1906)

[Stej65] E.O.Stejskal, J.E.Tanner “Spin Diffusion Measurements: Spin Echoes in the Presence of a Time-dependent Field Gradient” Journal of Chemical Physics 42(1) 288-292 (1965)

[Swie94] T.M. de Swiet, P.N.Sen “Decay of nuclear magnetization by bounded diffusion in a constant field gradient” Journal of Chemical Physics 100 5597-5604 (1994)

[Swie95] T.M. de Swiet “Diffusive edge enhancement in imaging” Journal of Magnetic Resonance series B 109 12-18 (1995)

[Tab91] D.Tabor “Gases, liquids and solids and other states of matter” 3rd Ed. Cambridge university press, 1991.

[Tala91] S.L.Talagala, I.J.Lowe “Introduction to magnetic resonance imaging” Concepts in Magnetic Resonance 3 145-159 (1991)

[Tast05] G.Tastain, PJ.Nacher “NMR measurements of hyperporalized ^{3}He gas diffusion in high porosity silica gels” The Journal of Chemical Physics 123 064506 (2005)

[Tayl00] N.Taylor “LASER: The inventor, the Nobel laureate, and the thirty-year patent war” New York: Simon & Schuster, 2000

[Torr63] H.C.Torrey “Chemical shift and relaxation of ^{129}Xe in Xenon gas” Physical review 130 6 2306-2312 (1963)

[Wayn66] R.C. Wayne, R.M.Cotts “Nuclear-Magnetic-Resonance Study of Self-Diffusion in a Bounded Medium” Physical Review 151 264-272 (1966)

[Wilk50] C.R.Wilke, “Diffusional Properties of Multicomponent Gases” Chemical Engineering Progress 46 2 95-104 (1950)

[Wolf04] M. Wolf. “Erzeugung höchster ^{3}He Kernspinpolarisation durch metastabiles optisches Pumpen” Ph.D. Thesis in the department of physics at the Johannes Gutenberg-Universität Mainz, Germany 2004

[Zaen07] P.P.Zaenker “NMR Spectroscopy and Imaging of Hyperpolarized Gases: Fundamental Aspects and Applications” Ph.D. Thesis in the department of physics at the Johannes Gutenberg-Universität Mainz, 2007.

Aknowledgements

JERRY: *But you don't understand! I'm a MAN!*
OSGOOD: *Well - nobody's perfect*.
Some Like It Hot (Billy Wilder)

An dieser Stelle möchte ich mich bei all den Personen bedanken, die zum Gelingen dieser Arbeit beigetragen haben: Besonders bedanken möchte ich mich bei ...

Herrn Prof. Dr. W.Heil und Herrn Prof. Dr. H.W.Spiess für die Möglichkeit, diese Arbeit unter hervorragenden Bedingungen in ihren Arbeitsgruppen anfertigen zu dürfen und für die wertvollen Anregungen.

Herrn Dr. Peter Blümler (alias Don Pedro) für seine Einführung in die NMR Hölle, endlose Geduld und seine Hilfe mit meinem Englisch, senkiu.

Herrn Dr. Jörg Schmiedeskamp (alias Jorgito) für die letzten Korrekturen, Vorschläge und Unterstützung. Du hast es geschafft, das Labor hat mich überlebt.

Herrn Prof. Dr. Rodolfo Héctor Acosta por los primeros latigazos para hacerme entender la RMN y por estar ahí para cualquier duda. Ya tomo mate solo.

Herrn Dr. Paul Zänker (alias Pablito) für die tagtäglichen Details und das Lächeln sogar in den schlimmsten Momenten

Herrn Dr. Jochen Schmidt für seine Freundschaft, Tipps in allen Lebenssituationen und die Musik im Hintergrund.

Frau Nadia Amor für ihre Gespräche, vor allem, als sie mit sich selbst gesprochen hat und für ihr lärmendes Lachen. Was bedeutet Stille?

es Dellers ihrm Christoph fürs beibringe wie mer rischtisch hessisch babbelt unn wie mer im flur schee die kegel wegwemmst (zusamme mit em Schmidte Jochen).

Chool Soon Moon and Young Yoo for the conversations about live and future.

Daniel, Sitipong, ... for remembering me that life is more than MPI.

Besonders den Technikern: Frank, Hanspeter und Manfred. Was werde ich ohne euch machen?

Den alten Spiessern : Han-Bong, Sylvia, Anke, Yao, Mao ...und den noch gebliebenen Mitarbeitern des AK Spiess für die freundliche Arbeitsatmosphäre und

ihre stetige Hilfsbereitschaft.

Gas deliverers: Jörg in seiner Jugend, Manuela, Zahir Salhi and Marion Batz for your disposition.

A la xent de Valencia per ser tan boniques i estar ahí els primers dies, gracietes bibiananurivictorstefan.

Dem Schwein (r.i.p.) von figure 6.15. Es war mir eine Ehre.

Las brujas por los akelarres, el guaro, los mojitos y putiar de la vida.

Mi princesita por la paciencia y escuchar sin entender.

It is strictly prohibited to use, to investigate or to develop, in a direct or indirect way, any of the scientific contributions of the author contained in this work by any army or armed group in the world, for military purposes and for any other use which is against human rights or the environment, unless a written consent of all the persons in the world is obtained.

Queda absolutament prohibida la utilització, recerca i desenvolupament, de manera directa o indirecta, de qualsevol de les aportacions científiques pròpies de l'autor que es presenten en aquesta memòria, per part de qualsevol exèrcit del món o per part de qualsevol grup armat, per a qualsevol ús militar i per a qualsevol altre ús que atempti contra els drets humans o contra el medi ambient, si no és amb el permís escrit de totes les persones del món.

Lebenslauf

Name:	Luis Agulles Pedrós
Geburtsdatum:	13. Oktober 1976
Geburtsort:	Dénia/Spanien

Schulbildung

1982–1990	Grundschule
1990–1995	Historiador Chabás Gymnasium, Dénia/Spanien
27.09.1995	Abitur

Studium

10/1996–06/2002	Physikstudium an der Universitat de Valéncia, Valéncia/Spanien
10/1999–10/2001	Austauschstudent an der Johannes Gutenberg Universität, Mainz
01/2001–08/2001	Wissenschaftlicher Mitarbeiter am A4-Forschungsgruppe im Kernphysikinstitut, Mainz
31.06.2002	Diplom in Physik
11/2002–04/2003	Wissenschaftlicher Mitarbeiter im Max-Planck-Institut für Polymerforschung in Mainz (MPIP)
04/2003–04/2004	Diplomarbeit zum Thema “Influence of diffusion on contrast and sensitivity in MRI of gases” beim Prof. Dr. W.Heil vom Institut für Physik im Zusammenarbeit mit dem Gruppe von Prof. Dr. H. W. Spiess am MPIP
04/2004–10/2007	Promotion zum Thema “Diffusion of laser polarized gases in MRI” unter der Betreuung von Prof. Dr. W.Heil und Prof. W. Spiess.